PHOTOSTIMULABLE NEAR-INFRARED PERSISTENT LUMINESCENT NANOPROBES FOR ULTRASENSITIVE AND LONGITUDINAL DEEP-TISSUE BIOIMAGING

by

YEN-JUN CHUANG

(Under the Direction of Zhengwei Pan)

ABSTRACT

Cancer imaging is very important in cancer diagnosis, prognosis, and therapy effectiveness monitoring. Among all the imaging techniques, fluorescence imaging is becoming an important set of tools in biomarker-guided diagnosis, staging, typing, and prognosis of cancer. However, *in vivo* fluorescence imaging suffers from suboptimal signal-to-noise ratio and shallow detection depth, caused by the strong tissue autofluorescence under external excitation and by the scattering and absorption of short-wavelength light in tissues. In this dissertation, we tackle these limitations by using a new, novel type of optical nanoprobes, $LiGa_5O_8:Cr^{3+}$ (LGO:Cr) nanoparticles with very-long-lasting near-infrared (NIR) persistent luminescence and unique NIR photostimulated persistent luminescence (PSPL) capability. This allows optical imaging to be performed in an excitation-free and hence autofluorescence-free manner. The LGO:Cr nanoparticles were fabricated by a sol-gel method, followed by calcination at high temperature. LGO:Cr nanoparticles pre-charged by ultraviolet light can be repeatedly (>20 times) stimulated *in vivo*, even from deep tissues, by short-exposure (~15 seconds) to a white light-emitting-diode flashlight, giving rise to multiple NIR PSPL that expands the tracking window from hours to 10 days. Our studies reveal promising potential of these nanoprobes in cell tracking and tumor

targeting, exhibiting exceptional sensitivity (~5 cells) and penetration (see through a mouse body) that far exceed those afforded by conventional fluorescence imaging.

INDEX WORDS: Near infrared, Persistent luminescence, Afterglow, Photostimulated persistent luminescence, Cr^{3+}-doped lithium gallium oxide, $LiGa_5O_8:Cr^{3+}$, Cytotoxicity, *In vitro* cellular studies, *In vivo* cell tracking, *In vivo* tumor targeting, Deep-tissue bioimaging, Biodistrubution, Optical imaging, Fluorescence imaging.

PHOTOSTIMULABLE NEAR-INFRARED PERSISTENT LUMINESCENT NANOPROBES FOR ULTRASENSITIVE AND LONGITUDINAL DEEP-TISSUE BIOIMAGING

by

YEN-JUN CHUANG

B.S., National Cheng Kung University, Taiwan, 2002

M.S., National Cheng Kung University, Taiwan, 2005

A Dissertation Submitted to the Graduate Faculty of the University of Georgia in Partial Fulfillment of the Requirements for the Degree

DOCTOR OF PHILOSOPHY

ATHENS, GEORGIA

2014

PHOTOSTIMULABLE NEAR-INFRARED PERSISTENT LUMINESCENT NANOPROBES FOR ULTRASENSITIVE AND LONGITUDINAL DEEP-TISSUE BIOIMAGING

by

YEN-JUN CHUANG

Major Professor:	Zhengwei Pan
Committee:	Lianchun Wang William Kisaalita Bingqian Xu

Electronic Version Approved:

Julie Coffield
Interim Dean of the Graduate School
The University of Georgia
August 2014

ACKNOWLEDGEMENTS

It goes without saying that this dissertation cannot be produced by one person, while this research involved multi-disciplinary. There are a number of persons who deserve special acknowledgement for their roles in making this work possible. I would like to thank my advisor, Dr. Zhengwei Pan for his guidance and support. He taught me how to do research – we must strive for rigor as much as we can, although it is impossible to cover every aspect. I would like to thank Dr. William Kisaalita, Dr. Lianchun Wang and Dr. Bingquan Xu for serving on my PhD supervisory committee. Thanks Dr. Lianchun Wang and Dr. Hong Zhuang (USDA-ARS, Athens, Georgia) for initial support and collaboration on nanoparticles surface modification and bio-imaging experiments. And also thanks to Dr. Jyoti P. Mishra at Dr. Lianchun Wang's group for helping me do cell cytotoxicity study of nanoparticles.

I would like to thank Dr. Jin Xie at the Department of Chemistry. Dr. Xie taught me how to design surface modification of nanoparticles, how to perform *in vitro* cell experiments and how to do small animal *in vivo* imaging. He also took responsibility for finding bioimaging systems and arranging his group members, including Dr. Zipeng Zhen, Ms. Wei Tang and Dr. Hongmin Chen for assistance. Special appreciation goes to Dr. Zipeng Zhen for assistance in cell and animal relative studies no matter how busy he was. Thank Ms. Wei Tang for producing cells with reliable performance. Thank Dr. Hongmin Chen for his valuable advice in the conjugation of nanoparticles.

I would like to thank my current and previous group members, Dr. Feng Liu, Dr. Yiying Lu, Dr. Wuzhao Yan, Dr. Xufan Li, Mr. Kaiyuan Li, Mr. Yanjie Liang, and Dr. Zhanjun Gu. It is

great to work with them. My sincere thanks go to Dr. Feng Liu. Dr. Liu taught me optical characterization of luminescent materials. Dr. Liu also read and revised this dissertation.

I would like to thank Dr. Xiaoyuan Chen at the National Institutes of Health (NIH) and his group member, Dr. Fan Zhang and Dr. Xinglu Huang, for conducting mouse brain imaging.

I would like to thank Dr. Yuping He for assisting me to operate XRD equipment at Dr. Yiping Zhao's lab. Special appreciation also goes to Mary Ard at the UGA College of Veterinary Medicine and Dr. Jane Howe at the Oak Ridge National Laboratory for helping on TEM characterization.

Finally, I would like to thank my parents and sister for their unconditional support and encouragement.

TABLE OF CONTENTS

Page

LIST OF TABLES

Page

LIST OF FIGURES

Page

LIST OF ABBREVIATIONS

BIDIPY	boron-dipyrromethene
BphPs	bacterial phytochrome photoreceptors
BRET	bioluminescence resonance energy transfer
BS^3	bis(sulfosuccinimidyl) suberate
CT	computed tomography
c(RGDyK)	cyclic Arg-Gly-Asp-D-Tyr-Lys
c(RGDyK)-LGO:Cr	c(RGDyK)-conjugated $LiGa_5O_8:Cr^{3+}$
EPR	enhanced permeability and retention
ESC	embryonic stem cell
FDA	Food and Drug Administration
f-luc	firefly luciferase
f-luc-4T1	firefly luciferase-expressing 4T1
FITC	fluorescein isothiocyanate
GFP	green fluorescent proteins
HSA	human serum albumin
ICP-MS	inductively coupled plasma mass spectrometer
IFP	infrared fluorescent proteins
LED	light emitting diode
LGO:Cr	$LiGa_5O_8:Cr^{3+}$
MRI	magnetic resonance imaging
NIR	near-infrared
PBS	phosphate buffered saline

PCA	principal component analysis
PEI	polyethylenimine
PEI-LGO:Cr	PEI-coated LGO:Cr
PET	positron emission tomography
PLL	poly-L-lysine
PSL	photostimulated luminescence
PSMA	prostate-specific membrane antigen
PSPL	photostimulated persistent luminescence
PVP	polyvinylpyrollidone
PVP-LGO:Cr	PVP-coated LGO:Cr
QD	quantum dot
RES	reticulo-endothelial system
ROX	carboxy-X-rhodamine
SEM	scanning electron microscopy
SPECT	single-photon emission computed tomography
SWCNT	single-walled carbon nanotube
TAMRA	carboxytetramethylrhodamine
TEM	transmission electron microscopy
TEOS	tetraethyl orthosilicate
TMA	tetramethylrhodamine
UV	ultraviolet
SD	standard deviation
S/N	signal-to-noise

CHAPTER 1

INTRODUCTION

1.1 Luminescence basics

Luminescence is the emission of light by a substance through a process not caused by heat.[1,2] It is thus a form of cold body radiation. The excitation of luminescence is usually achieved with external irradiation, chemical reactions, electrical energy, subatomic motions, or crystallographic changes.[3] A luminescent material, also called a phosphor, is a solid which converts certain types of energy into electromagnetic radiation over and above thermal radiation.[4] In this section, the different types of luminescence are introduced and discussed.

1.1.1 Photoluminescence

Photoluminescence is a process in which materials absorb external photons, resulting in an excitation to a higher energy state, and then releasing that energy in the form of light.[5-7] In inorganic phosphors, photoluminescence is generally grouped into two basic types: intrinsic luminescence and extrinsic luminescence.[8] The intrinsic luminescence center is native to host materials and involves band-to-band recombination of electron-hole pairs. Intrinsic luminescence may also be associated with lattice defects within the materials. Extrinsic luminescence is the most common form of luminescence and is attributed to the presence of trace impurities. This type of origin is referred to as "impurity centers" (also called activators or emitting centers). When foreign atoms, or impurities, are introduced into a host, the optical properties of the material will be conferred. This is because impurities will create localized energy levels in the

forbidden band of the host, which allow them to give rise to the appearance of optical transitions whose energy is lower than the band gap of the host. Due to these energy levels that are not present in the host, various emission wavelengths corresponding to the transitions from various levels will occur. Therefore, doping is the strategy to engineer the optical properties of semiconductors or insulators. Transition metal ions and rare earth ions are the two types of commonly used dopants.

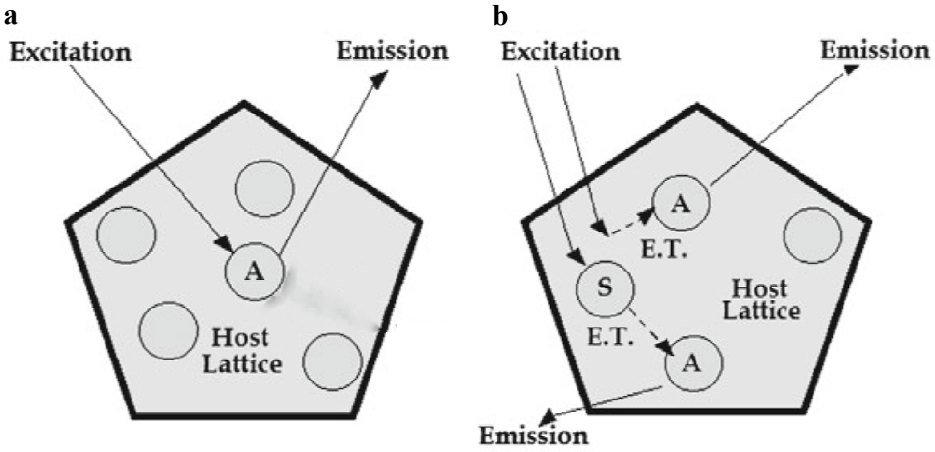

Figure 1.1 Photoluminescent materials containing activator ions (A) and sensitizing ions (S). **a**, Direct excitation of the activator. **b**, Indirect excitation followed by energy transfer from the sensitizer or host to the activator. (This figure is reproduced from reference 5 with the permission of Springer.)

The absorption of light energy, which is used to excite the luminescence, takes place by either the host lattice or by intentionally doped impurities. In most cases, the emission takes place on the activator ions. When the activator ions show too weak absorptions, a second kind of impurities can be added as sensitizers, which absorb the energy and subsequently transfer the energy to the activators.[5,9] This process involves the transport of energy through the luminescent materials, as shown in Figure 1.1.

Figure 1.2 shows typical excitation and emission spectra of photoluminescent materials.[5] The absorption and emission probability for photons depends on the atomic energy levels of

activators. The locations of the energy levels of activator ions are affected by the crystal field of host materials. In addition, the relative strength of different absorption and emission lines are generally defined by local symmetry of the host lattice.

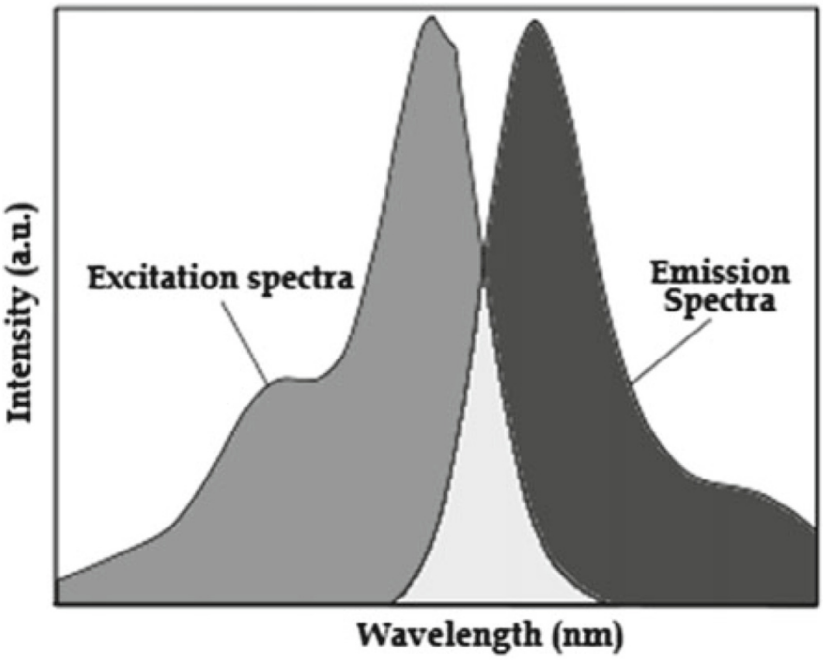

Figure 1.2 General excitation and emission spectra for photoluminescent materials. (This figure is reproduced from reference 5 with the permission of Springer.)

In contrast to inorganic phosphors where luminescence is affected by their lattice structures, organic phosphors (*e.g.*, organic dyes) are usually aromatic compounds where the luminescence is based on localized π-electron systems.[10] Photoluminescence from organic compounds can be classified into two categories: luminescence from electronically excited singlet (S_1) or triplet (T_1) states. Emission from singlet excited states, called "fluorescence," is commonly observed in conventional organic compounds. Emission from triplet excited states, called "phosphorescence," is rarely observed in conventional organic compounds at ambient temperatures due to the small radiative decay rate of phosphorescence. The process of fluorescence and phosphorescence can be explained by the simple Jablonski diagram (also called diagram of electronic transitions), as

shown in Figure 1.3.[7,11] The lifetime of fluorescence is very short (<10 ns) and the lifetime of phosphorescence is usually longer than 10 ns.

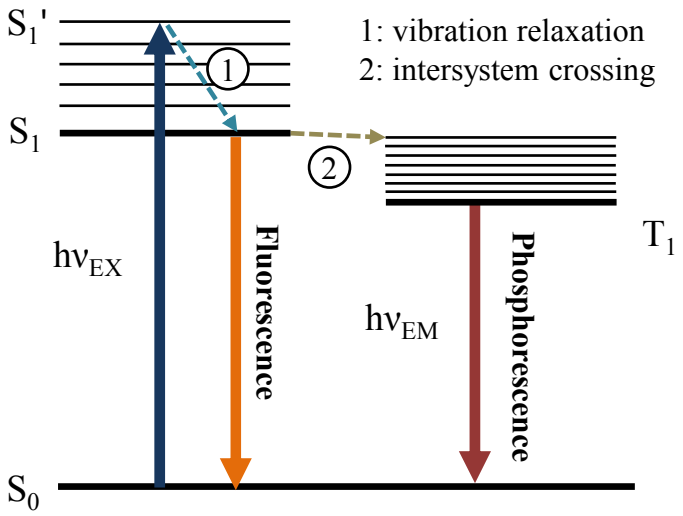

Figure 1.3 Jablonski diagram illustrating the processes of fluorescence and phosphorescence. The straight-line arrows and dashed-line arrows represent optical transition and electron transfer processes, respectively. (S_0: ground states; S_1: first singlet excited states; S_1': first singlet excited states at higher vibrational sublevels; T_1: first triplet states; $h\nu_{EX}$: excitation light; $h\nu_{EM}$: emission light.)

Photostimulated luminescence (PSL, also called as optically stimulated luminescence) is also an example of photoluminescence. When a storage phosphor is exposed to high-energy radiation, such as x-ray or ultraviolet (UV) light, part of the excitation energy is stored in the phosphor by capturing charge carriers (electrons or holes) in traps, which are generally lattice defects or impurities.[12-14] The stored energy in photostimulable storage phosphors is released as PSL by low-energy light (photon) illumination.[12,14-17] They have been used in a plethora of important applications in the fields of dosimetry and x-ray imaging.[16,18]

1.1.2 Persistent luminescence

Persistent luminescence, also called afterglow, is an optical phenomenon where a material is emitting, for an appropriate time, from minutes to many hours, after the irradiation (excitation) source has been switched off at room temperature.[6,19] Persistent luminescence is nominally an isothermal case of thermoluminescence.[20] Thermoluminescence is emitted by thermal stimulations after storage phosphors expose to irradiation.[3] In persistent luminescent materials, two kinds of active centers are generally involved: emitting centers and traps.[6] Emitting centers are capable of emitting radiation after being excited. Traps usually do not emit radiation, but store excitation energy by trapping charges and release them gradually to the emitting centers due to thermal or other physical stimulations. Figure 1.4 shows a simplified schematic model of

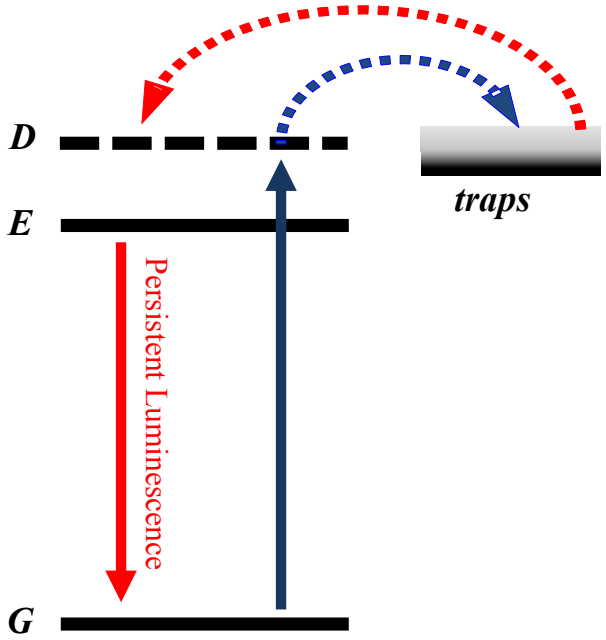

Figure 1.4 Schematic diagram of typical persistent luminescence mechanism. *G*, *E*, and *D* represent the ground state, emission state, and delocalized state, respectively.

the commonly accepted Eu^{2+} persistent luminescence process based on an electron transfer assumption.[21] Under the excitation, electron from the ground-state (*G*) of the emitting centers is

pumped to the delocalized state (*D*) lying in the conduction band of the host. The delocalized electron is captured by and stored in electron traps, which are generally lattice defects or impurities and locate close to the bottom of the conduction band. After ceasing the excitation, the captured electron escapes back to the *D* state owing to thermal or other physical stimulations, followed by nonradiative relaxation to the *E* state and then radiative return to the *G* state, accompanying with persistent luminescence emission.

1.1.3 Other examples of luminescence

In addition to excitation by radiation, luminescence can also be generated by chemical reactions (chemiluminescence), mechanical energy (triboluminescence), electrical energy (electroluminescence), sound waves (sonoluminescence), *etc*.[3,8] For example, chemiluminescence occurs when the vibronically excited product of an exoergic reaction relaxes to its ground state with light emission. It can be simply defined as chemical reactions that emit light.[22] Bioluminescence is light produced, within a living organism, by a chemical reaction that requires an enzyme known as luciferase, a substrate (luciferin) and oxygen for the chemical reaction. Some luciferases require other cofactors such as ATP and Mg^{2+} for full activity.[23] In other words, Bioluminescence is a chemiluminescence that takes place inside a living organism.

1.2 Optical Bioimaging

Bioimaging techniques can be grouped by the energy used to derive visual information (X-rays, positrons, photons or sound waves), and the spatial resolution that is attained (macroscopic, mesoscopic or microscopic).[24] Macroscopic imaging techniques that provide anatomical and physiological information are now in widespread clinical and preclinical uses. These techniques

include magnetic resonance imaging (MRI), positron emission tomography (PET), computed tomography (CT), ultrasound imaging and single-photon emission computed tomography (SPECT).[25,26] They are often used to survey whole body for disease and to do cross-sectional imaging, particularly for research on deep-seated organs. However, the high cost of these techniques and a number of technological barriers impair their widespread use.[27]

Macroscopic optical imaging techniques are used to probe more local processes and can readily make use of multiple labels, or signal-emitting tags that are attached to a molecule of interest. It is becoming an essential tool in biomedical research and drug development, owing to its advantages of high-throughput, non-invasive, non-radioactive, easy-to-operate, and cost-effective.[28-31]

Most optical imaging techniques work by tracing fluorescence signals from optical probes. Despite its dominance in analyzing cells and tissues *in vitro*, however, fluorescence imaging technique is minimally used for *in vivo* clinical applications because of its poor signal-to-noise (S/N) ratio and general shallow detection depth (< 1 cm).[29] These drawbacks are mainly associated with tissue autofluorescence and optical scattering. Autofluroescence is caused by the fluorescence from tissue due to the constant external irradiation. The autofluorescence mainly depends on tissue absorption. When light travels out of tissues, the light is attenuated by tissues, especially for visible light.[27,30,32] In addition, optical scattering occurs due to mismatches in refractive index of the different tissue components, ranging from cell membranes to whole cells.[33,34] In cellular level, sizes of subcellular organelles range from less than 100 nm to 6 μm. Most of organelles interact with light whose wavelength is similar to the size of organelle, leading to Mie scattering.[35]

To reduce autofluorescence, tremendous efforts have been spent on finding near-infrared (NIR) optical probes, because windows of the first and second NIR region (NIR I, 650–950 nm, and NIR II, 1000–1350 nm) has a relatively low level of tissue absorption, as shown in Figure 1.5.[36] To minimize scattering interference, numerous mathematical models and techniques were established and have been used in optical imaging.[37,38] However, optical imaging is still developing, especially for *in vivo* deep-tissue bioimaging, because it is still hard to achieve most clinical applications.

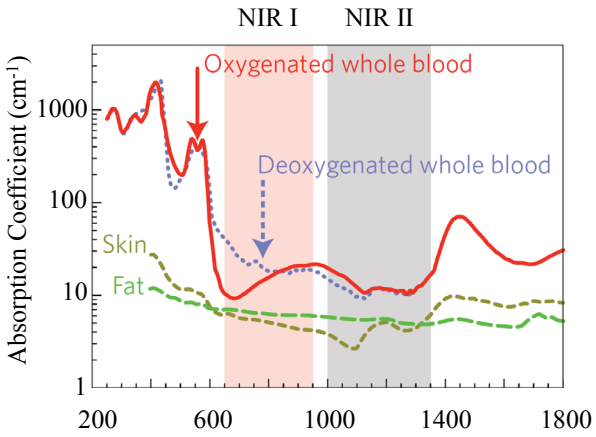

Figure 1.5 Absorption coefficients (on a log scale) of oxygenated whole blood, deoxygenated whole blood, skin, and fatty tissue (Fat) as a function of wavelengths. (This figure is reproduced from reference 36 with the permission of Multidisciplinary Digital Publishing Institute.)

1.3 Probes for optical bioimaging

The commonly used optical probes can be classified into two groups: fluorescent probes and self-luminescent probes. The fluorescent probes include organic dyes,[39,40] fluorescent proteins,[41-43] quantum dots,[44-47] single-walled carbon nanotubes,[37,48] and upconverting nanoparticles.[49] The self-luminescent NIR probes include hybrid nanoparticle[50] and persistent luminescent nanoparticles.[27]

1.3.1 Fluorescent probes

1.3.1.1 Organic dyes and fluorescent proteins

Organic dyes. Fluorescent organic dyes include various derivatives of coumarin, pyrene, naphthalene, fluorescenin, rhodamine, boron-dipyrromethene (BIDIPY) and cyanine.[51] The

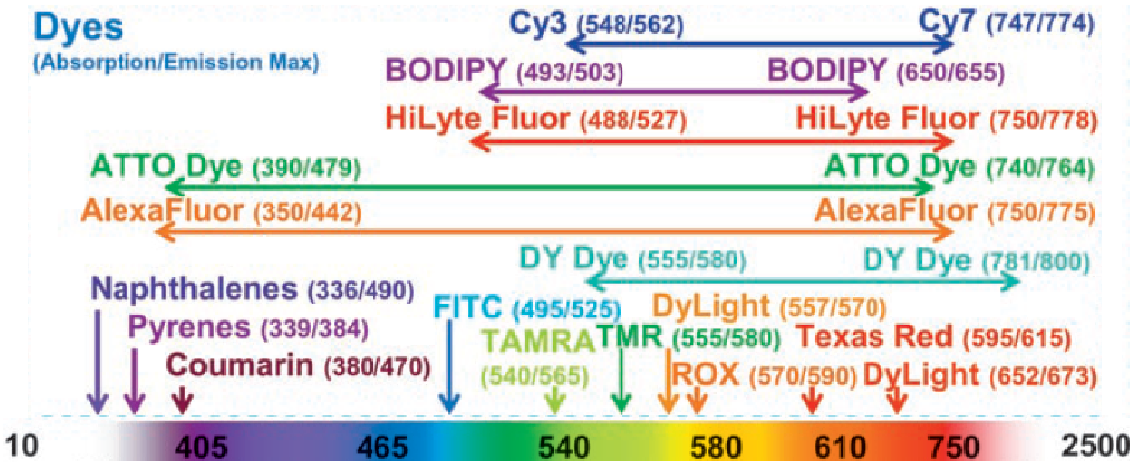

Figure 1.6 Examples of commercially available fluorescent dye families. Absorbance and emission maxima along with spectral regions covered by a particular dye family are labeled as (absorbance (nm)/emission (nm)). Tetramethylrhodamine (TMR), carboxytetramethylrhodamine (TAMRA), and carboxy-X-rhodamine (ROX) are all rhodamine-based dyes. FITC: fluorescein isothiocyanate. (This figure is reproduced from reference 52 with the permission of John Wiley and Sons.)

fluorescence emissions from these derivatives cover ultraviolet, visible, and NIR region from 384 nm to 800 nm (Figure 1.6).[52] However, only few organic dyes have been used in practical medical diagnosis. For example, indocyanine green (emission peaking at 800 nm) is a Food and Drug Administration (FDA)-approved NIR probe for fluorescence retinal (ophthalmologic) angiography.[53]

Fluorescent proteins. Green fluorescent proteins (GFP) were found in the jellyfish *Aequorea victoria*. Martin *et al.* first reported a complementary DNA for the *Aequorea victoria* GFP producing a fluorescent product when expressed in prokaryotic (*Escherichia coli*) or eukaryotic (*Caenorhabditis elegans*) cells.[42] Now according to their colors and chromophore

structures, over 150 distinct GFP-like proteins have been reported, which are classified into seven groups,[54-57] including Cyan or Green, Yellow (Zoanthus), Red (DsRed-type), Red (Kaede-type), Red (KFP-type), mOrange (*in vitro* evolution), and non-fluorescent.

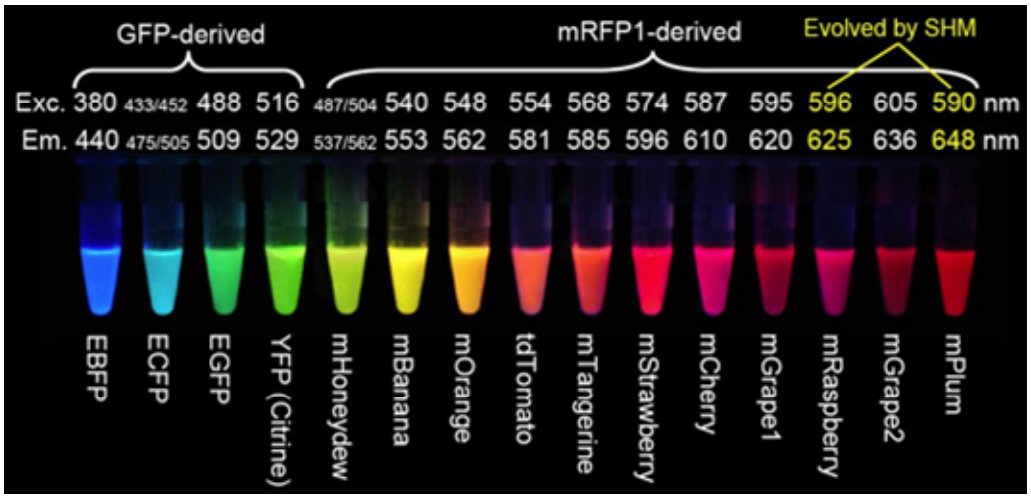

Figure 1.7 Monomeric or tandem dimeric fluorescent proteins. The photo of fluorescent proteins was taken under different excitation wavelengths and cutoff filters. (Image from Roger Y. Tsien's Nobel Lecture on 8 December 2008)

Before 2009, the emissions of these fluorescent proteins used in mammals cover from blue light to red light in visible spectral region, as shown in Figure 1.7.[57] However, deep optical imaging in mammalian tissues and whole mammals requires NIR fluorescent proteins.[43] Shu *et al.* used bacterial phytochrome photoreceptors (BphPs) as a template to obtain infrared fluorescent proteins, IFP1.4, in mammalian cells in 2009.[41] Later, mutations of BphPs resulted in the generation of infrared fluorescent proteins: Wi-Phy (emission peaking at 719 nm) and iRFP (emission peaking at 670–720 nm).[58] IFP1.4 and iRFP were previously used for whole-body imaging.[43] IFP1.4 required injection of biliverdin to become fluorescent, but iRFP efficiently incorporated endogenous biliverdin, making iRFP as easy to use as conventional GFP-like FPs. iRFP was applied for live imaging of livers and tumors in mice.

Inherent drawbacks for organic fluorophores (organic dyes and fluorescent proteins) include a short Stokes shift, poor photochemical stability, susceptibility to photobleaching and decomposition under repeated excitation, which limit their applications.[45,59] However, organic dyes are still popular due to their low cost, wide availability, and ease of use. Fluorescent proteins are still the most popular tool to trace and visualize *in vivo* molecular activities in cells.[28]

1.3.1.2 Quantum dots

Quantum dots (QDs) are zero dimensional nanocrystals made of semiconductor materials. Compared with fluorescent dyes, QDs show size-dependent emission, which enables ease of tuning emission by simply controlling their size.[60] Figure 1.8 shows the emission wavelengths of

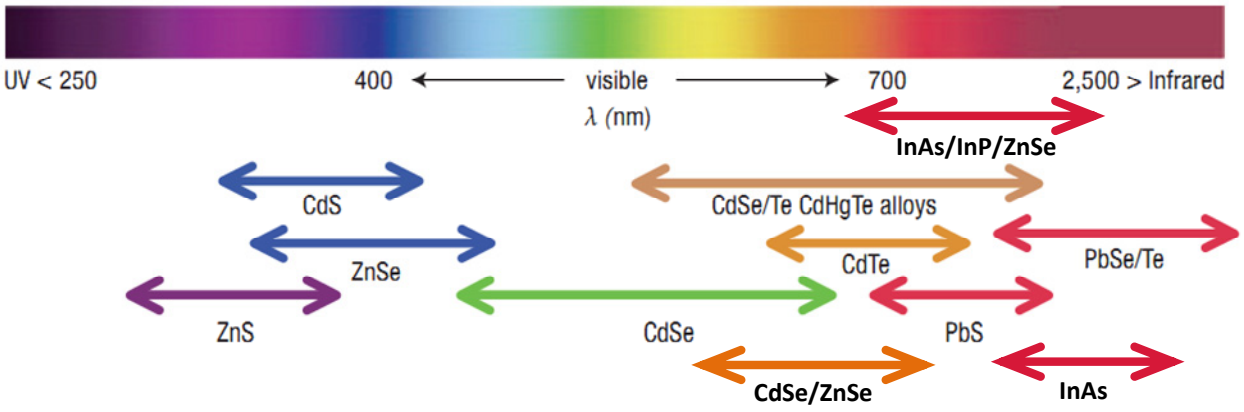

Figure 1.8 Representative QD core materials scaled as a function of their emission wavelengths superimposed over the spectrum. (This figure is modified from reference 61 and 62.)

colloidal QDs made of ZnS, CdSe, CdTe, PbS, PbSe and InAs, covering a wide spectral range from UV to NIR.[61,62] For biological applications, the best QDs are core-shell nanocrystals. For example, the CdSe core of CdSe/ZnSe QDs are caped with a layer of ZnSe, which passivates the core surface, protects the core from photooxidation, and improves the fluorescence quantum

yield of the QDs. Due to their wide absorption spectra, QDs with different emission wavelengths excited by a single light source can emit various color fluorescence; therefore, QDs have a great potential for multicolor molecular imaging.[61,62] Although the unique properties of QDs attribute to high photostability and size-tunable light emission, QDs containing Class A elements (Cd and Hg) and Class B elements (As and Se) are toxic and can cause organ damage.[45]

1.3.1.3 Single-walled carbon nanotubes

Single-walled carbon nanotubes (SWCNTs) were found to have NIR light emission between 930nm and 1550 nm (Figure 1.9).[63] This makes them the ideal second NIR (1000–1350 nm) probes especially suitable for deep-tissue *in vivo* imaging. However, the biggest obstacle in realizing the potential of SWCNTs as NIR probes is producing SWCNTs with high quantum efficiency and good biocompatibility.[48] To overcome this issue, Welsher *et al.* came up with a strategy of first debundling and solubilizing the hydrophobic, pristine SWCNTs in sodium cholate by sonification, followed by surfactant exchange to displace the sodium cholate with pegylated phospholipid.[64] The resulting water-soluble SWCNTs exhibit several emission peaks across from 900 to 1500 nm when excited at 808 nm.[37] *In vivo* circulation and biodistribution of the SWCNTs can be monitored for about two minutes after tail-vein injection SWCNTs in athymic nude mice. High-resolution optical imaging of mice organs was obtained by dynamic contrast-enhanced imaging with principal component analysis (PCA), as shown in Figure 1.10.[37] Later, both high spatial (~30 μm) and temporal (<200 ms per frame) resolution for *in vivo* small-vessel imaging were achieved at 1–3 mm deep in a mouse model of the hind limb.[65]

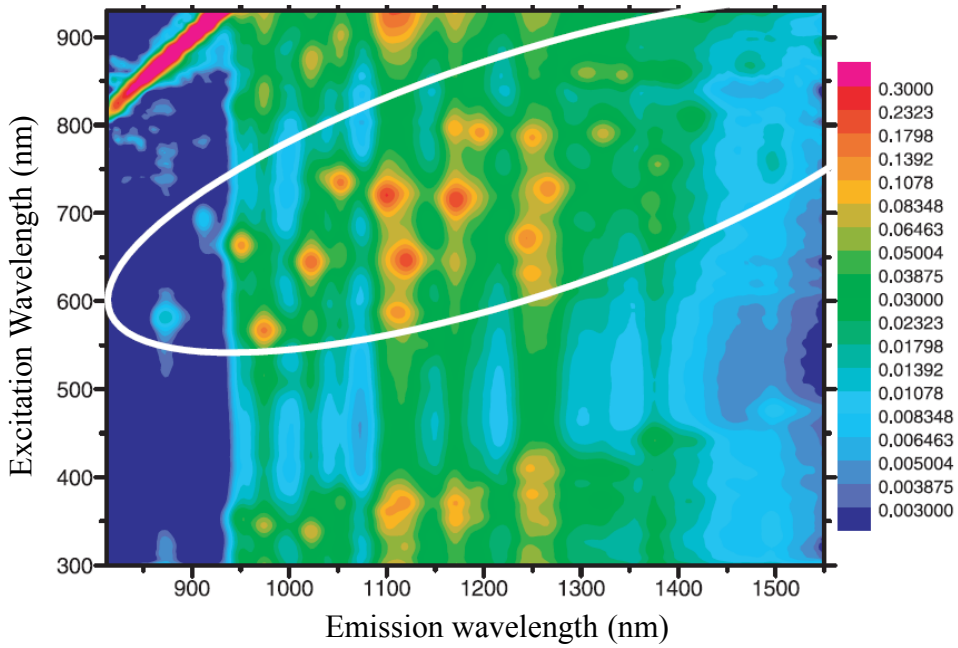

Figure 1.9 Contour plot of fluorescence intensity versus excitation and emission wavelength for a sample of SWCNTs suspended in an aqueous solution. The white oval drawn marks a region that contains discrete peaks, arising from the E_{11} transitions ($c_1 \rightarrow v_1$ emission, NIR fluorescence), excited by E_{22} absorption ($v_2 \rightarrow c_2$ excitation). (This figure is reproduced from reference 63 with the permission of American Association for the Advancement of Science.)

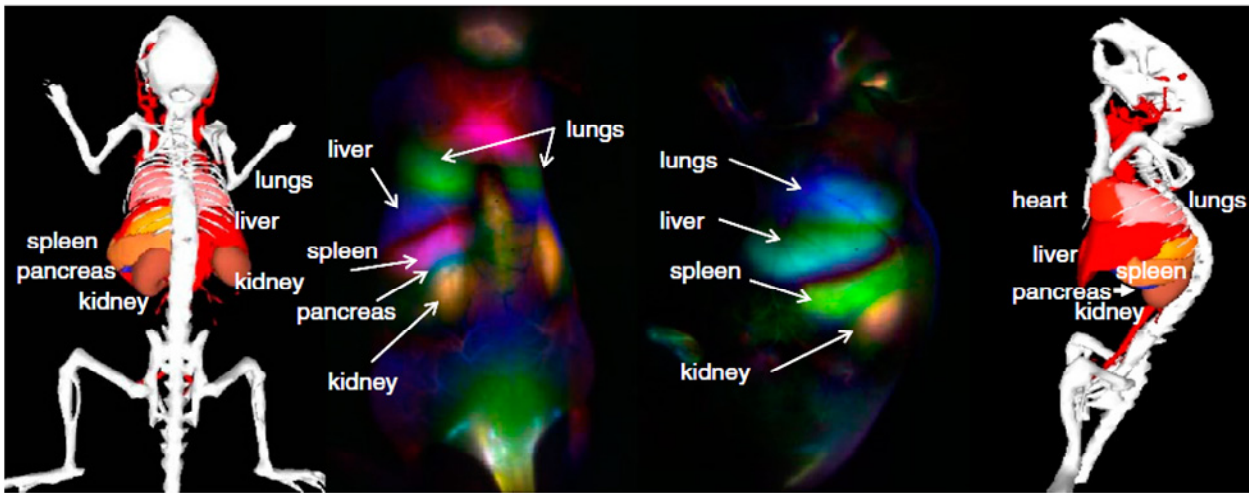

Figure 1.10 Dynamic contrast-enhanced imaging with SWCNTs through PCA. (This figure is reproduced from reference 37 with the permission of National Academy of Sciences.)

1.3.1.4 Upconverting nanoparticles

Upconverting nanoparticles are usually fluoride (*e.g.*, $NaYF_4$, $KMnF_3$, and CaF_2) nanoparticles doped with lanthanide ions.[49,66] The typical lanthanide dopants are the following ion pairs (sensitizer/activator): Yb^{3+}/Er^{3+}, Yb^{3+}/Tm^{3+} and Yb^{3+}/Ho^{3+}. Through the combination of host materials and lanthanide dopants, upconverting nanoparticles can exhibit wavelength selective emissions, which can be UV,[67] visible (blue, green, red),[68-70] or NIR emission,[69-73] under longer NIR (~980 nm) excitation.

For example, Liu *et al.* doped Gd^{3+} ions into $NaLuF_4$ host materials to get pure hexagonal-phase NaLuF4.[74] The resulting $NaLuF_4$:Gd^{3+},Yb^{3+},Tm^{3+} nanoparticles with sub-10 nm sizes can emit at 800 nm under 980 nm excitation. Both the excitation and emission are located in the NIR spectral range, enabling great tissue penetration depth of up to ~2 cm and low autofluorescence.[74,75] However, the quantum efficiency of lanthanide-based upconverting nanoparticles in water is relatively low. For example, the quantum efficiency of sub-10 nm $NaLuF_4$:Gd^{3+},Yb^{3+},Tm^{3+} nanoparticles is only ~0.47%.[74] It requires high power continuous-wave laser (100 $mWcm^{-2}$ power density) as an excitation source to induce the upconversion. Moreover, water, the most significant component in animal and human body, strongly absorbs 980 nm light. Increasing the laser power and irradiation time can cause remarkable overheating effects.[76]

1.3.2 Self-luminescent probes

To minimize or ideally completely remove the tissue autofluorescence, an ideal imaging probe is the one that can self-luminesce NIR light without the need of external light excitation. Such probes can yield a higher signal to noise ratio and a deeper penetration depth for animal

imaging than the fluorophore-based optical probes. Two types of self-luminescing NIR probes were recently developed: hybrid nanoparticles and persistent luminescent nanoparticles.

1.3.2.1 Hybrid nanoparticles

Bioluminescent proteins, such as *R. reniformis* luciferase, usually emit visible bioluminescence in the presence of oxygen and substrate (luciferin) without photo-irradiation. With the need of NIR light-emitting probes for *in vivo* deep-tissue bioimaging, Xiong *et al*. reported hybrid nanoparticles as self-luminescing NIR probes based on bioluminescence resonance energy transfer (BRET).[50] BRET is the energy transfer from a bioluminescent protein to a receptor, such as QDs[30,77] or semiconductor polymer nanoparticles.[50] Though conceptually interesting, the applications of these BRET-based technologies in translational research is limited because of the concerns regarding the probe's *in vivo* stability, the inherent toxicity of heavy metals of the QDs, the dependence of imaging duration on the half-lives of the proteins, and/or the high sensitivity of the probes to environmental changes.[78]

1.3.2.2 Persistent luminescent nanoprobes

In 1996, Matsuzawa *et al*. reported the first generation of modern persistent luminescent material, the Eu^{2+} and Dy^{3+} co-doped $SrAl_2O_4$.[79] Up to now, there are persistent materials for each of the main visible colors with the representative ones including $Sr_2MgSi_2O_7:Eu^{2+},Dy^{3+}$ (blue, ~25 h afterglow), $SrAl_2O_4:Eu^{2+},Dy^{3+}$ (green, ~30 h afterglow), and $Y_2O_2S:Eu^{3+},Mg^{2+},Ti^{4+}$ (red, ~5 h afterglow), as shown in Figure 1.11.[19,21,80] Although about 300 visible persistent materials have been developed, the research and development of persistent materials in the NIR

region (~700–2500 nm) are lacking, even though there are growing demands for applications as optical probes for *in vivo* deep-tissue bioimaging.[47]

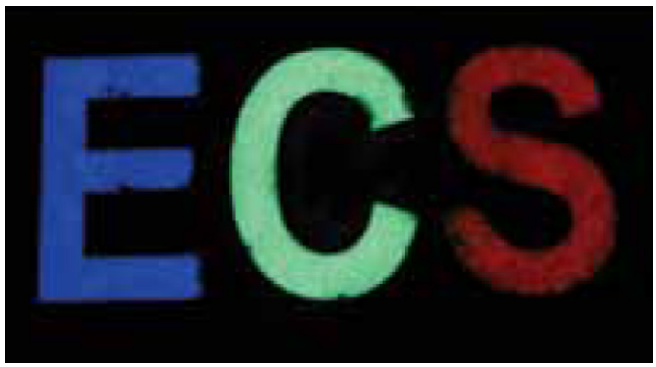

Figure 1.11 Image of persistent luminescence of visible emitting phosphors. Blue emitting $Sr_2MgSi_2O_7:Eu^{2+},Dy^{3+}$ (E), green emitting $SrAl_2O_4:Eu^{2+},Dy^{3+}$ (C), and red emitting $Y_2O_2S:Eu^{3+},Mg^{2+},Ti^{4+}$ (S) phosphors in dark. (This figure is reproduced from reference 19 with the permission of the Electrochemical Society.)

The first persistent luminescent $Ca_{0.2}Zn_{0.9}Mg_{0.9}Si_2O_6:Eu^{2+},Dy^{3+},Mn^{2+}$ nanoparticles as self-luminescing probes for *in vivo* bioimaging were introduced by de Chermont *et al*. in 2007.[27] The nanoparticles, emitting persistent 690 nm light after UV irradiation, open a new avenue for biomedical imaging, enabling imaging technique to be performed with a high signal-to-noise (S/N) ratio and a deep detection depth, and thus providing promising prospect for the wide deployment of biomedical imaging technique for clinical applications. However, the further development of the nanoparticles for bioimaging was restricted by the short persistence time (<1 h).[27,81] Therefore, there is an urgent need for functional NIR-emitting persistent luminescent nanoparticles with long persistent luminescence for long-term targeted tumor imaging *in vivo*.[81]

Recently, Cr^{3+}-doped gallate-based NIR persistent phosphors received considerable attention due to their novel optical properties.[18,81-94] Since 2010, our group reported several representative series of Cr^{3+}-doped gallate systems, which can emit very-long (up to several hundreds of hours) NIR persistent luminescence, including $La_3Ga_5GeO_{14}:Cr^{3+}$,[85] Cr^{3+}-doped zinc gallogermanates

(Zn-Ga-Ge-O:Cr^{3+})[86,87] and Cr^{3+}-doped lithium gallates (Li-Ga-O:Cr^{3+})[18,88] in the forms of bulk materials. Later, several similar material systems (such as $ZnGa_2O_4$:Cr^{3+} and $MgGa_2O_4$:Cr^{3+}) but with shorter persistence time were also reported.[81,89-94] Despite the significant progress of bulk long persistent phosphors, the persistence time of their corresponding nanomaterials is too short, which limits the application of persistent luminescent nanoparticles in *in vivo* bioimaging. The longest observation time for subcutaneously injected persistent luminescent nanoparticles was 15 h,[81] while the *in vivo* distribution of intravenously injected nanoparticles was followed in real-time for only 0.5 to 7.5 h.[27,81] Such a short time span is barely sufficient for tracking molecules, not to mention cell tracking, where a tracking window of days or even weeks is expected.[95]

1.4 Preparation of oxide phosphors

The traditional technique used to produce persistent oxide phosphors in the forms of solid ceramics or micro-scale powders is a high-temperature solid-state reaction method. In the solid-state reaction, metal oxide powders as precursors directly react to form the final products at high temperature.[18,87,96] For example, NIR persistent $Zn_3Ga_2Ge_2O_{10}$:Cr^{3+} phosphor was synthesized by mixing stoichiometric amounts of ZnO, Ga_2O_3, GeO_2 and Cr_2O_3 powders and then sintering at 1350 ˚C to form a solid ceramic.[87] In the synthesis of oxide persistent luminescent nanoparticles, four methods were usually used, including co-precipitation,[97] sol-gel method,[18,27,98] hydrothermal synthesis,[91,99] and combustion methods.[100]

The co-precipitation method produces the nanoparticles through insoluble species formed under high supersaturation conditions. A large number of small particles are formed during nucleation and then grow by Ostwald ripening and aggregation until reaching supersaturation conditions to induce precipitation.[101,102] To synthesize $SrAl_2O_4$:Eu^{2+},Dy^{3+} persistent

nanoparticles, co-precipitation occurs when metal nitrate salts ($Sr(NO_3)_2$, $Al(NO_3)_3$, $Eu(NO_3)_3$, $Dy(NO_3)_3$) mix with oxalic acid in base aqueous solution (pH = ~10).[97] The dry precipitates were then calcinated at 1000 ˚C in air, following heat treatment in a reducing atmosphere of 5% H_2/N_2.[103] Co-precipitation reactions are usually performed at low reaction temperatures (<100 ˚C), and the induced precipitation is usually the result of a chemical reaction. As such, any reaction conditions influencing the mixing process, such as rate of reactant addition and stirring rate, must be considered.[102] The complicated process results in a lower homogeneity of the precipitated nanoparticles, compared with the sol-gel methods discussed below.

The sol-gel method is a wet-chemical technique that uses a chemical solution as a precursor to produce an integrated network (gel) of discrete particles or polymers. The precursors are prepared by desirable compounds with specific stoichiometric ratios.[102,104-107] The liquid phase is removed from the gel to convert polymer network containing metal compounds into an oxide network *via* drying process. The dry gel is calcinated in order to get crystalline phases and to improve the optical properties. To prepare $SrAl_2O_4:Eu^{2+},Dy^{3+}$ persistent nanoparticles, aluminum complexes were first prepared by refluxing aluminum isopropoxide in 2-methoxyethanol and then mixed with metal nitrates **(**$Sr(NO_3)_2$, $Eu(NO_3)_3$, $Dy(NO_3)_3$**)** in a aqueous solution containing ethylacetoacetate, which acted as chelating agent to form stable metal complexes.[98] The sol was stirred and kept in an ice bath to activate the gel formation. The gel was dried at 120 ˚C and then calcinated at 1200 ˚C to form powder. Finally, $SrAl_2O_4:Eu^{2+},Dy^{3+}$ phosphor with persistent luminescence was obtained after reducing the calcinated powder in an atmosphere of H_2/N_2 at 1300 °C.

Hydrothermal synthesis is a versatile low temperature route for synthesizing metal oxide nanoparticles. In hydrothermal synthesis, the reaction is performed under high vapor pressure

(generally in the range from 0.3 to 4 MPa) and at temperatures above the boiling point of water (generally in the range from 130 to 250 ˚C).[102,108,109] Under these hydrothermal conditions, the solubility of precursors in water increases significantly, enabling reactions to take place at low temperature. This technique allows obtaining good crystalline nanoparticles. To obtain $Gd_2O_2S:Eu^{3+},Ti^{4+},Mg^{2+}$ persistent nanophosphors, metal nitrates ($Gd(NO_3)_3$, $Eu(NO_3)_3$) as precursors in a base aqueous solution were sealed in a Teflon container.[101] The Teflon contanier was then kept in a sealed, stainless steel capsule at 200 ˚C to produce white precipitants. The dry precipitants reacted with sulfur powder, $MgCO_3$ and TiO_2 at 800 ˚C in a reducing enviroment to obtain $Gd_2O_2S:Eu^{3+},Ti^{4+},Mg^{2+}$ powder.

Combustion synthesis method was accidentally discovered in 1988 in Prof. Patil's lab in India.[110] In combustion synthesis, fuel and oxidizer are required. For the combustion synthesis of oxide nanoparticles, metal nitrates (such as zinc nitrate for ZnO) are used as oxidizer, and hydrazine based compound or glycine are commonly used as the fuels. Stoichiometric compositions of metal nitrates and fuels are calculated based upon propellant chemistry.[111] In a typical combustion process, the fuel and oxidizer are dissolved in a minimum amount of water in a Pyrex dish which is then introduced into a muffle furnace or on a top of a heat plate maintained at 400–500 ˚C. The solution boils, foams and ignites to burn with flame (at about 1400 ± 100 ˚C) to yield voluminous, foamy oxide. The entire combustion process lasts for less than 5 minutes (the burn with flame just lasts tens of seconds). The combustion process is self-propagating, *i.e.*, once ignited it goes to completion without supply of additional heat. The major advantages of the combustion method are improvement in processing time, energy saving, the ability in atomic level doping of impurity ions in the host lattices, and the fine particle nature of the products. This

technique has been use to synthesize Eu^{2+}, Dy^{3+} and Er^{3+} co-doped $SrAl_2O_4$ NIR persistent nanoparticles.[100]

In the fabrication of oxide persistent luminescent nanophosphors, calcination at high temperature is needed to improve the luminescence properties and crystallinity of the materials. While the calcination improves the persistent luminescence properties, it also leads the aggregation of nanoparticles. To obtain small size nanoparticles, wet grinding, a simple physical way to break down the aggregates, is frequently used. In the process of wet grinding, the aggregated powder is suspended in a liquid media, and then mechanical forces (from a grinding mill or mortar/pestle) are applied to tear apart the aggregates suspended in the liquid. Due to the dispersing effect of the liquid media, it avoids the particle re-aggregation and obtain fine-size nanoparticles.[112,113] Now, wet grinding is becoming a popular method to increase the yield rate of persistent luminescent nanoparticles after synthesis.[18,27,81,89,92]

1.5 Surface modification of metal oxide nanoparticles

Nanoparticles are becoming the indispensable tools for medicine, biology and pharmaceutical industries, because of their unique size dependent properties such as electrical, magnetic, mechanical, optical and chemical properties, which largely differ from those of their bulk counterparts.[114,115] Since nanoparticles have much higher surface energy than the sub-micron sized particles, nanoparticles have an extremely high tendency of adhesion and aggregation. To improve the dispersion and biocompatibility of nanoparticle, surface modification or encapsulation is generally used to alter the physical, chemical and mechanical properties as well as surface structures of nanoparticles.

This section intends to give an overview of the major functional groups that tend to react with metal oxide surfaces and some of protocols reported in the literature for the coating or encapsulating of metal oxide nanoparticles. Metal oxide nanoparticles were mainly modified or encapsulated by organic ligands,[116] polymers,[117-119] and liposomes.[120,121]

1.5.1 Organic ligands

The most suitable compounds for modifying metal oxide nanoparticles include silanes, phosphonoates and carboxylates. Silanes, such as alkoxysilane, hydrogenosilane, and chlorosilane, are organofunctional alkoxysilane molecules. Since abundant hydroxyl groups exist on the surfaces of metal oxides, the alkoxy groups of silanes can be attached and displaced by hydroxyl groups to form a covalent -Si-O-Si bond. For example, silanization of metal oxide nanoparticle surfaces with tetraethyl orthosilicate (TEOS) led to silica coated nanoparticles. It is easy to introduce amino functional groups to metal oxide surfaces by replacing the TEOS with 3-aminopropyl triethoxysilane.[122] Phosphonates binding to surfaces of metal oxides forms phosphorus-oxygen-metal (P-O-M) linkages.[123,124] Phosphonic acids and phosphoric acids can easily functionalize surfaces of metal oxides, such as TiO_2,[125-127] Al_2O_3,[128,129] SnO_2,[130,131] ZnO[132] and Fe_2O_3,[133] through P-O-M bonds. Carboxylates are also often used to modify metal oxide nanoparticles.[134] Xie *et al.* reported a very simple method to turn hydrophobic magnetic nanoparticles into hydrophilic ones by ligand exchanges with dimercaptosuccinic acid, which provides the particles with additional functionality.[135] The dimercaptosuccinic acid first forms a stable coating through its carboxylic chelate bonding and further stabilization of the ligand shells is attained through intermolecular disulfide cross-linkages between ligands under ambient

conditions. The remaining free thiol groups of DMSA ligand are used for the attachment of target specific antibodies.

1.5.2 Polymers

The adsorption of polymeric dispersant is one of the simplest surface modification techniques to improve the dispersion stability of nanoparticles in liquid media. The polymeric dispersants are divided into two groups: natural polysaccharides and synthetic polymers.

The most common nature polysaccharides used in surface modification is dextran.[117,118] Dextran easily meets the strict criteria of nontoxicity, nonimmunogenic, nonantigenic and biodegradability in the requirements of biomedical applications.[117] In addition, total bonding energy of hydrogen-bonds over the length of dextran can be very high because of the large number of hydroxy groups per molecule, although single hydrogen bond are relatively weak.[136] This helps to chelate and then stabilize metal oxide nanoparticles. Dextran-stabilized magnetic nanoparticles are obtained by coprecipitation from aqueous solutions containing iron oxide precursors and dextran.[119,136]

To disperse nanoparticles into aqueous media with synthetic polymers, three kinds of polymeric dispersants, including anionic, cationic and nonionic polymers, are widely used to generate steric repulsive force from the polymer chains and to increase the surface charge.[137] For anionic polymers, various derivatives of polycarboxylic acids, polyacrylic acid,[138-144] and polyvinyl alcohol[145] are used to disperse many kinds of oxide nanoparticles such as $BaTiO_3$,[138] TiO_2,[142] Al_2O_3,[139,144] and Fe_2O_3.[143] In cationic polymers, polyethylenimine (PEI) is a popular dispersant for stabilizing of Al_2O_3[146] and TiO_2[147] nanoparticles. Pluronics are a family of poly(ethylene oxide)-b-poly(propylene oxide)-b-poly(ethylene oxide) tri-block copolymers used

as nonionic polymers in biotechnological and pharmaceutical industries for their unique abilities (*i.e.*, low toxicity and minimal immune response).[148] Polyvinylpyrollidone (PVP) is also a nonionic polymer which has been used in various medical applications, due to its high water-solubility and non-toxicity.[149] These two nonionic polymers have been used for thermal synthesis of iron based magnetic nanoparticles.[150]

1.5.3 Liposomes

Encapsulation of magnetic nanoparticles in stealth liposomes seems to be a promising approach to improve the applicability of magnetic nanoparticles in biomedical applications. Liposomes can be considered as a special class of vesicles, in which the building blocks units are lipids. Martina *et al.* developed magnetic fluid-loaded liposomes by encapsulating maghemite nanocrystals within unilamellar vesicles of egg lipids (phosphatidylcholines) and polyethylene glycol (PEG).[120,121] Magnetic fluid-loaded liposomes with hydrodynamic size of ~195 nm were capable of encapsulating up to 1.67 mol of iron per mol of lipid. *In vivo* evaluation in mice using magnetic resonance angiography demonstrated that these magnetic fluid-loaded liposomes were still present in blood 24 h after the intravenous injection, confirming their long circulating behavior.

1.6 Motivations

To overcome the limitations encountered in optical imaging and yield a robust modality for fluorescent probes *in vivo*, ideal probes should possess the following characteristics. (1) It is self-luminescent and long-lasting; that is, the luminescence signal from the probe can be detected *in vivo* for a considerable long time (>1 week) without continuous external excitation.[18,50] This can permit the complete removal of the autofluorescence and hence the background noise originating from *in situ* excitation. (2) The emission is in the tissue optical window (*i.e.*, 650–900 nm or 1000–1350 nm), in which light attenuation is largely due to scattering rather than absorption.[36] (3) It has high chemical stability and photostability in aqueous environment.[45,151] (4) It is biocompatible in physiological condition.[151] (5) It has functional groups for site-specific cell labeling in an easy and transfection-free manner.[152] (6) Its size can be tuned and controlled.[151] (7) It is available in a reproducible quality and can be produced in large volume.[151] It is anticipated that fluorescent probes with these characteristics can enable imaging to be conducted on a conventional imaging system in a bioluminescence mode with minimized background, excellent S/N ratio, great penetration depth, high spatial resolution, long-term tracking (or long circulating half-life), and cell- or tumor-specific targeting. However, no currently available probes meet all these characteristics.

The work presented in this dissertation aims to synthesize novel photostimulable NIR persistent luminescent nanoparticles, $LiGa_5O_8:Cr^{3+}$ (LGO:Cr), which satisfy almost all the requirements for an ideal optical probe listed above. The LGO:Cr nanoparticles emit intense, long-lasting NIR persistent light after the removal of the excitation. This allows the nanoparticles to be tracked *in vivo* without external excitation, permitting the complete removal of the autofluorescence. The resulting imaging is bestowed with a significantly improved S/N ratio,

allowing for detection in rather deep-tissues with high sensitivity. The emission (peaking at 716 nm) is in the tissue transparency window. This can further increase the detection depth. Remarkably, the UV-pre-irradiated LGO:Cr nanoparticles can be repeatedly stimulated by long-wavelength light, *e.g.*, white light emitting diode (LED) flashlight), which allows for longitudinal (days or even weeks) monitoring/tracking of the LGO:Cr labeled cells *in vivo*. These novel photostimulable NIR persistent luminescent nanoprobes provide promising potentials for cancer diagnosis and cell therapy research.

CHAPTER 2

PRELIMINARY UNDERSTANDING OF PHOTOSTIMULATED NIR PERSISTENT LUMINESCENCE OF CHROMIUM-DOPED LITHIUM GALLIUM OXIDE

2.1 Introduction

Photostimulated luminescence, PSL, is introduced in Section 1.1.1. Briefly, the optical information written by X-ray or UV irradiation on an imaging plate is read out as a visible PSL signal under the stimulation of a low-energy light (such as a red laser) with appropriate wavelengths in conventional photostimulable storage phosphors.

Photostimulable storage phosphors such as BaFBr:Eu^{2+}, have been widely used as imaging plates for optical information write-in and read-out in dosimetry and X-ray imaging. The optical information write-in and read-out processes require optically illuminating the phosphor plate twice.[15,16] The first exposure by an x-ray beam or a UV light "writes" a latent image in the form of trapped electrons on the phosphor plate. The number of trapped electrons is proportional to the amount of radiation absorbed locally and the latent image is optically readable within a certain time frame (usually within 8 h for practical use) after the exposure. The second illumination with a light of appropriate wavelength, typically an intense light with low energy (*e.g.*, red He-Ne lasers), "reads" the image in the form of higher energy visible PSL signal (*e.g.*, violet-blue emission for BaFBr:Eu^{2+} phosphor).[11,12] Most of the trapped electrons are extracted during the read-out process, and the residual electrons remaining on the phosphor plate can be erased through illumination with bright fluorescent light so that the plate can be used again. Therefore, the photostimulable storage phosphors which exhibit the PSL phenomenon can be used as

erasable and rewritable optical memory media for many advanced optical storage applications. For example, the best-known and the most commercially successful photostimulable storage phosphor so far is BaFBr:Eu^{2+}, which is being widely used as the imaging plates in computed radiography.[11,12]

Unlike the transient PSL, here we introduce a new optical read-out form, photostimulated persistent luminescence (PSPL) in the NIR, from a $LiGa_5O_8:Cr^{3+}$ (LGO:Cr) phosphor. An intense PSPL signal with an emission peaking at 716 nm can be repeatedly obtained in a period of more than 2000 h when a UV light (250–360 nm) pre-irradiated LGO:Cr phosphor is repeatedly stimulated by a light between 380–1000 nm.

2.2 Energy level structure of Cr^{3+} ions in phosphors

Cr^{3+} was recently adopted as an emitting center in NIR persistent phosphors. The Cr^{3+} ion (with electronic configuration of [Ar]$3d^3$) has three electrons occupying the outermost 3*d* electron orbits of the ions. When Cr^{3+} ions are doped into solids, spectroscopic properties are considerably changed. These changes are explained in terms of crystal field theory, which assumes anions (ligands) surrounding the metal ion as point electric charges.[10]

For free ions, the energies of the five 3*d* orbitals are identical. However, when the ions are doped into crystals, crystal field theory shows that the splitting of 3*d* energy level depends strongly on the symmetry of the crystallographic site. For example, when the Cr^{3+} ions are in the sites with octahedral symmetry, the energy level is split into two groups: *E* and T_2, as shown in Figure 2.1.

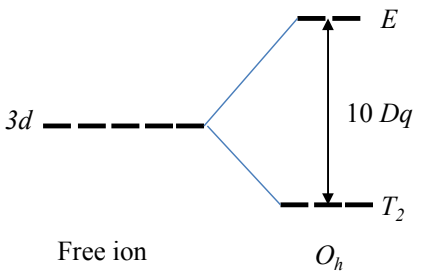

Figure 2.1 Energy level splitting of *d*-orbitals in octahedral (O_h) symmetry. *Dq* represents the interaction of the *d* electrons with the electrostatic fields of the ligands.

Figure 2.2 shows the Tanabe–Sugano diagrams for $3d^3$ configurations. The level energies *(E)* from the ground level are plotted against the crystal field energy (*Dq*). Both *E* and *Dq* are in units of B (Racah parameter). The left-hand side of the diagram corresponds to the free ion case (Dq = 0), and the split components resulting from the crystal-field are shown on the right side.

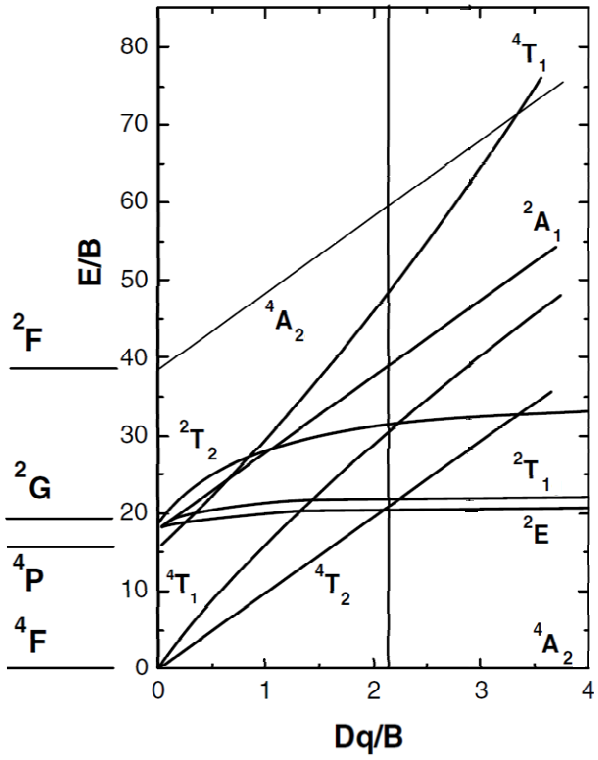

Figure 2.2 Tanabe-Sugano diagram of $3d^3$ ion in octahedral field. (This figure is reproduced from reference 153 with the permission of Wiley.)

The term symbols for free-ion states of transition metal ion are labeled as $^{2S+1}$L states, where *S* is the total spin quantum number and L is the total orbital angular momentum. These term symbols are called Racah parameters, such as ^{4}F, ^{4}P, ^{2}G, ^{2}F, as shown in Figure 2.2.[153] Crystal field energy levels are labeled as $^{2S+1}$X, where X can be A for orbital singlet, E for a doublet and T for a triplet. For instance, the ground state of a free ion of d^3 configuration is ^{4}F, and the ^{4}F state is further split into a $^4A_2$ ground state and two excited states ($^4T_2$ and $^4T_1$) in an octahedral crystal field. The other excited states of the free ion also split into different A, T and E levels.

Emission from Cr^{3+} ion can change from a sharp line to a broad band, depending on the crystal field strength around it in the host lattice. When the Cr^{3+} ion locates in a strong octahedral crystal field (Dq/B >2.3), the first excited level will be the ^{2}E term, which give a narrow sharp luminescence line. In a weak octahedral crystal field (Dq/B <2.3), the $^4T_2$ term will become the lowest excited level which gives a broadband emission ranging from 650 nm to 1200 nm.

2.3 Synthesis and characterizations of $LiGa_5O_8:Cr^{3+}$ bulk materials

Synthesis of LGO:Cr bulk materials. LGO:Cr phosphors in the forms of solid ceramic discs were synthesized by a solid-state reaction method.[18] Stoichiometric amounts of Li_2CO_3, Ga_2O_3 and Cr_2O_3 powders were ground to form a homogeneous fine powder (the Cr content in the LGO:Cr phosphor demonstrated here is 1 atom%). The mixed powder was then prefired at 800 °C in air for 2 h. The prefired material was again ground to fine powder suitable for sintering. The prefired powder was pressed into discs with diameters of 15 mm and 40 mm using a 16-ton hydraulic press. The discs were then sintered at 1300 °C in air for 2 h to form a solid ceramic. The 15-mm-diameter discs were used as-is. Some 40-mm-diameter discs were cut into 15 × 15 mm^2 plates for deliberate imaging experiments.

Characterization of LGO:Cr bulk materials. The spectral properties (excitation and emission spectra, decay curves, persistent luminescence emission and excitation spectra, thermoluminescence curves and PSPL write-in and read-out spectra) of the LGO:Cr discs were measured using a Horiba FluoroLog-3 spectrofluorometer equipped with a 450 W xenon arc lamp and a R928P photomultiplier tube (250–850 nm). All spectra were corrected for the optical system responses. Appropriate optical filters were used to avoid stray light in all spectral measurements.

Thermoluminescence curves were recorded using a homemade measurement setup (temperature range, −196–280 °C; heating rate, 4 °C/s). The typical measurement system consists of a programmable temperature controller, a heater, a photomultiplier tube, and a computer. Constant heating rate is accurately maintained by the programmable temperature controller and is recorded as x-axis. The luminescence from the sample is detected by the photomultiplier tube and recorded as y axis.

NIR persistent luminescence and PSPL photos of the samples were taken in a dark room using a Pentax digital SLR camera which was connected to an ATN PVS-14 Generation III night vision monocular. The monitoring and imaging experiments were conducted in a dark room. Before all the spectral measurements and imaging, the samples were heat-treated in a muffle oven at 400 °C for 20 min to completely empty the electron traps.

Four light sources were used to activate the LGO:Cr discs for spectral measurements and imaging: a 450 W xenon arc lamp (in a FluoroLog-3 spectrofluorometer), a 4 W 254 nm UV lamp, and a YAG:Ce-based white LED flashlight (85 lumens).

2.4 Luminescence properties of $LiGa_5O_8:Cr^{3+}$ ceramics

2.4.1 Photoluminescence and super-long persistent luminescence in the NIR

Cr^{3+}-doped $LiGa_5O_8$ (LGO:Cr) was studied in the 1970s but neither NIR persistent luminescence nor NIR PSPL was reported.[154] Figure 2.3 shows the normalized photoluminescence emission and excitation spectra of a LGO:Cr phosphor disc at room temperature. Under excitation at 400 nm, the material exhibits a narrow-band emission (red curve in Figure 2.3) peaking at 716 nm. This NIR emission is characteristic of Cr^{3+} ions and can be attributed to the spin-forbidden $^2E \rightarrow {}^4A_2$ transition. The associated broad background

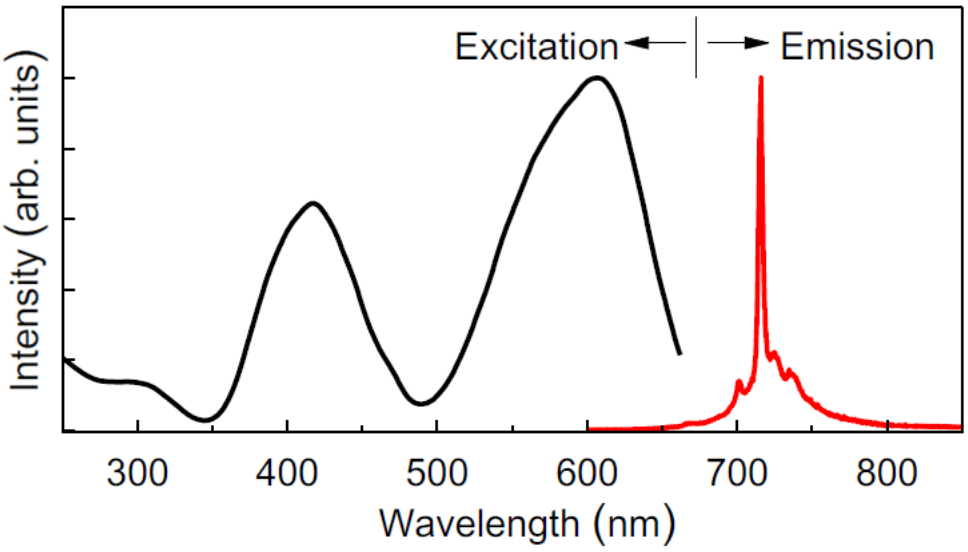

Figure 2.3 Photoluminescence of LGO:Cr phosphor discs at room temperature. Normalized excitation and emission spectra for photoluminescence. The emission spectrum is acquired under 400 nm light excitation and the excitation spectrum is obtained by monitoring 716 nm emission.

emission ranging from ~650 nm to ~850 nm originates mostly from the phonon sidebands of the $^2E \rightarrow {}^4A_2$ transition.[154] The photoluminescence excitation spectrum monitored at 716 nm emission covers a very broad spectral region (from ~250 to ~660 nm, black curve in Figure 2.3 and consists of three main excitation bands originating from the inner transitions of Cr^{3+}, including the 300 nm band originating from the $^4A_2 \rightarrow {}^4T_1(^4P)$ transition, the 415 nm band

originating from the $^4A_2 \rightarrow {}^4T_1(^4F)$ transition, and the 605 nm band originating from the $^4A_2 \rightarrow {}^4T_2(^4F)$ transition.

Besides the intense NIR photoluminescence, the excitation of UV light can also induce very-long-lasting NIR persistent luminescence in LGO:Cr phosphor with a persistence time >1000 h. Figure 2.4 shows the persistent luminescence decay curve of a LGO:Cr phosphor disc monitored at 716 nm after irradiation by 300 nm UV light for 20 min. The recording lasted for 120 h. As can be seen, the persistent luminescence intensity drops quickly in the first several hours and then decays slowly. After 120 h of persistent emission, the persistent luminescence intensity is still significantly high, indicating that the NIR persistent luminescence should last much longer than 120 h. The upper inset of Figure 2.4 shows a persistent luminescence emission spectrum recorded at 1 h after the stoppage of the 300 nm UV light irradiation. The profile of the persistent luminescence emission spectrum is almost identical to that of the photoluminescence emission spectrum (Figure 2.3), indicating that the NIR persistent luminescence originates from the Cr^{3+}emitting centers.

However, unlike the NIR photoluminescence which can be effectively excited by a wide range of wavelengths (~250–660 nm) (Figure 2.3), the NIR persistent luminescence in LGO:Cr cannot be induced by low-energy visible light irradiation. To evaluate the effectiveness of different excitation wavelengths (energies) for persistent luminescence, we measured the persistent luminescence decay curves monitored at 716 nm after the excitation of monochromatic light with different wavelengths between 250–600 nm in 10 nm steps, recorded the persistent luminescence intensity at 10 s after the stoppage of each excitation (I_{10s}), and plotted the intensity I_{10s} as a function of the excitation wavelengths, as the ball curve shown in the bottom inset of Figure 2.4. It is clear that the NIR persistent luminescence can be effectively achieved by

UV irradiation between 250–360 nm (250 nm is the low limit of the xenon emission in the FluoroLog-3 spectrofluorometer), and the effectiveness increases as the excitation moves to shorter wavelengths.

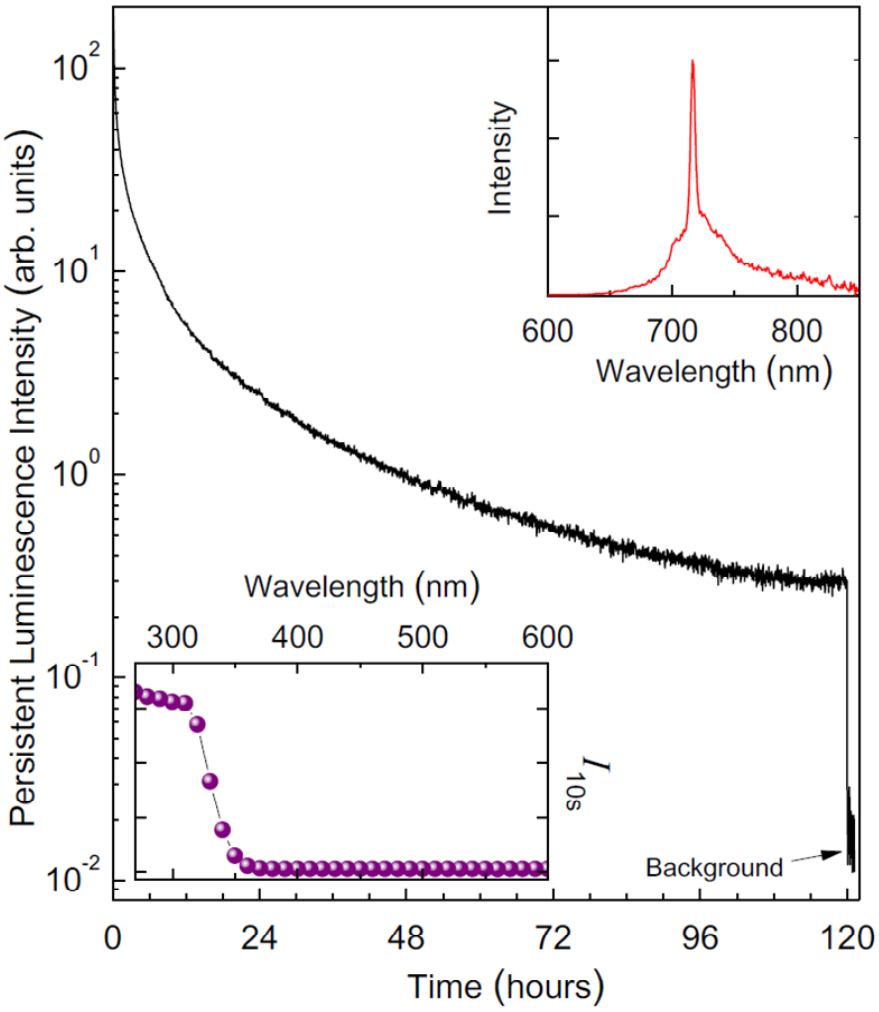

Figure 2.4 Persistent luminescence of a LGO:Cr phosphor disc at room temperature. NIR persistent luminescence decay curve monitored at 716 nm after irradiation by 300 nm light for 20 min. The upper inset shows the persistent luminescence emission spectrum recorded at 1 h after the stoppage of the irradiation. The bottom inset is the persistent luminescence excitation spectrum obtained by plotting the persistent luminescence intensity (I_{10s}) monitored at 716 nm as a function of the excitation wavelengths over the 250–600 nm spectral range. The persistent luminescence intensity at time of 10 s after the stoppage of the irradiation is noted as I_{10s}. Each data point was I_{10s} obtained from each room temperature persistent luminescence decay curve of the LGO:Cr phosphor disc irradiated by monochromatic light at the selected excitation wavelength. The disc was irradiated for 5 min at each measured wavelength using a xenon arc lamp.

The very-long-lasting NIR persistent luminescence of the LGO:Cr phosphor disc was also visually evaluated using a night-vision monocular in a dark room. Figure 2.5a–f shows the

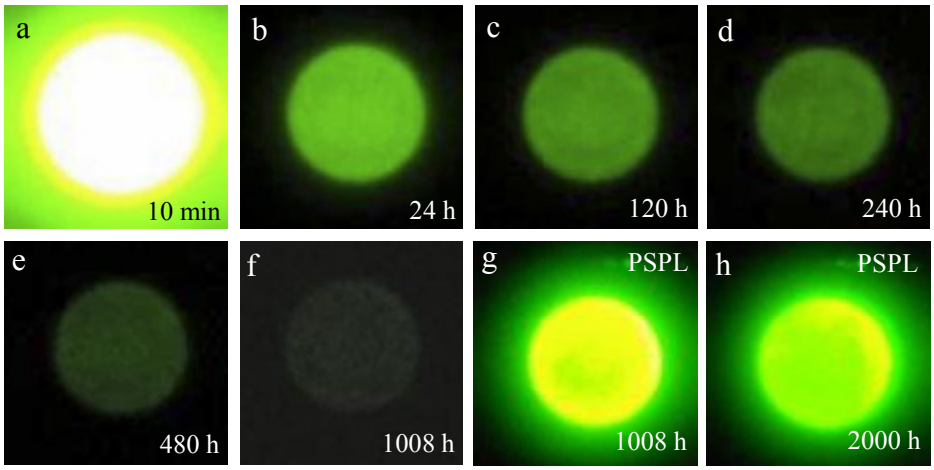

Figure 2.5 Persistent luminescence and PSPL images of a LGO:Cr phosphor disc at room temperature. **a**–**f**, NIR persistent luminescence images of phosphor discs. Images were taken at different persistent luminescence times (10 min to 1080 h) after irradiated by a 254 nm lamp for 1 min. **g**–**h**, NIR PSPL images of phosphor discs. Starting from the 1008 h time point, the phosphor disc was stimulated by a white LED flashlight. The PSPL images were taken at 10 s after ceasing the white LED stimulation. The imaging parameters are: **a**, **b**, **g** and **h**, manual/ISO 400/10 s, **c**–**e**, manual/ISO 800/30 s, and **f**, manual/ISO 1600/30 s.

changes of NIR emission "brightness" with a natural decay time up to 1008 h for the LGO:Cr disc after exposure to a 4 W 254 nm UV lamp for 1 min. Figure 2.5a–f clearly shows that the LGO:Cr phosphor discs can be effectively activated by the 254 nm UV lamp and 1 minute of UV irradiation can result in 1008 h of persistent NIR emission. Remarkably, after 1008 h of natural decay, short (~20s) white LED stimulation can recover, the luminescence signal from the decayed LGO:Cr disc, as the images shown in Figure 2.5g–h. It should be noted that, as the PSPL phenomenon that will be discussed below, the energy stored in the LGO:Cr phosphor disc during excitation is not completely released even after 1008 h room-temperature decay. Thus, the actual persistent luminescence decay time of the LGO:Cr phosphor at room temperature should be longer than 1008 h.

2.4.2 Photochromism

In irradiating the LGO:Cr phosphor discs using a 254 nm UV lamp in room light environment, we observed that the body color of the LGO:Cr sample changed from greenish to reddish, as the digital pictures shown in Figure 2.6a,b. This UV irradiation induced coloration phenomenon is long lived at room temperature, lasting for more than one month (the samples need to be stored in the dark); however, it can be quickly bleached by external stimulations, such as through illumination with bright fluorescent light or through heating at around 400 °C. This coloration/bleaching process can be repeatedly carried out without leaving any permanent changes to the optical performance of the LGO:Cr samples. The change of body color due to UV irradiation is qualitatively reflected by measuring the diffuse reflectance absorption on the samples with and without UV irradiation, as the spectra shown in Figure 2.6c. Compared with the non-irradiated sample (curve 3), the spectra of the UV-irradiated sample (curves 1 and 2) contain an additional green absorption band peaking at ~500 nm, as the dash-line curve and dot-dashline curve shown in Figure 2.6c. The presence of the additional green absorption band, together with the strong absorption of the material to blue light, make the UV-irradiated LGO:Cr discs appear to be reddish in room light condition.

Since the repetitive coloration/bleaching processes do not cause permanent change to the samples, the coloration phenomenon can be attributed to the formation of photochromic centers,[155,156] which may result from the trapping of photogenerated electrons by the deep-level lattice defects (such as oxygen vacancies adjacent to the chromium ions) in LGO:Cr. Also, since the fading of coloration is accompanied by the decrease of persistent luminescence intensity at room temperature, the deep-level lattice defects used to form the photochromic centers may also act as deep electron traps responsible for the long persistent luminescence.

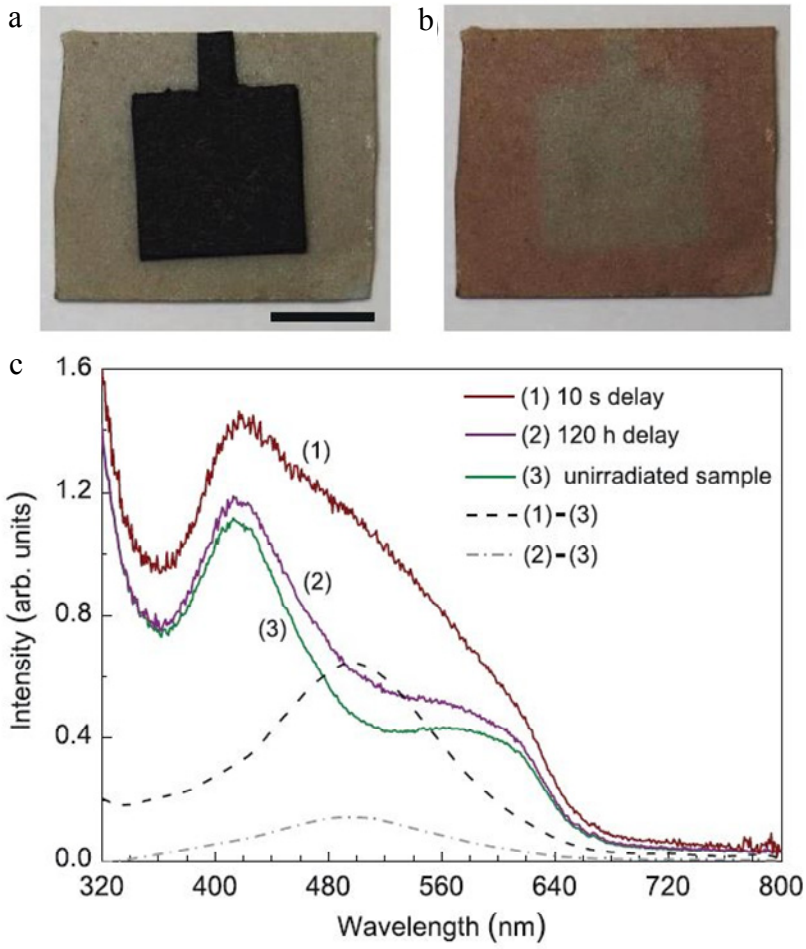

Figure 2.6 UV-irradiation-induced coloration and changes in diffuse reflectance absorption of LGO:Cr phosphor plates. **a**, Digital image of a 15 × 15 mm^2 LGO:Cr phosphor plate with its center covered by an 8 × 8 mm^2 black paper in room light environment. Scale bar, 5 mm. **b**, The same plate as the one in **a** after exposed to a 254 nm UV lamp for 5 min. The paper was removed after the irradiation. **c**, Diffuse reflectance absorption spectra acquired on LGO:Cr plates with and without UV irradiation. Curve 1 and curve 2 were recorded on a 300 nm-light-irradiated plate (for 20 min) with delay times of 10 s and 120 h, respectively. Curve 3 was acquired on a bleached plate (without UV pre-irradiation). The dash-line curve is the difference between curve 1 and curve 3. The dot-dash-line curve is the difference between curve 2 and curve 3.

To further understand the properties of electron traps and photochromic centers in LGO:Cr, we conducted thermoluminescence measurements on phosphor discs undergoing different delay

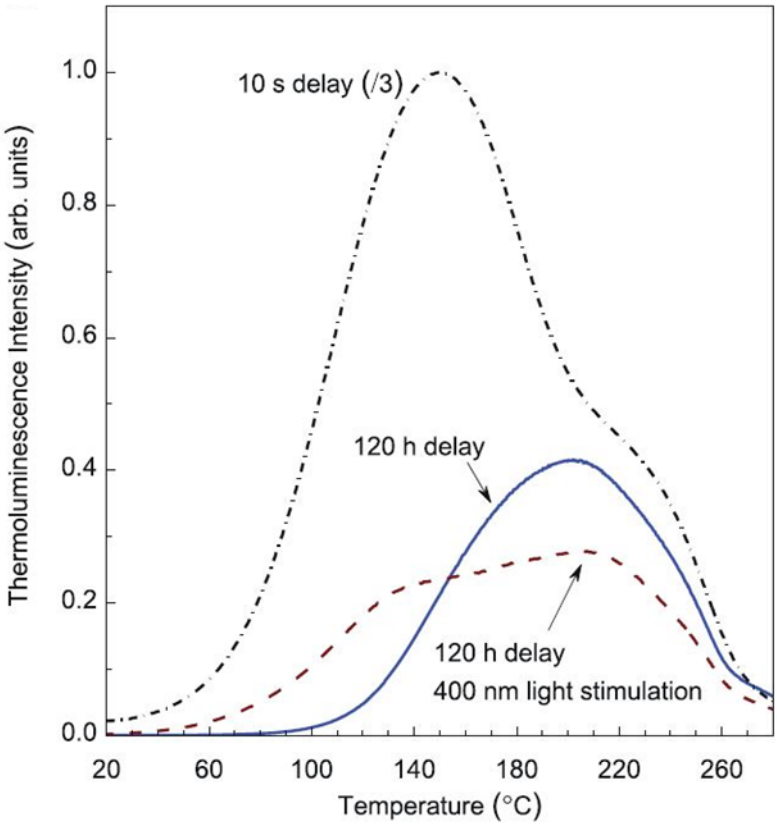

Figure 2.7 Thermoluminescence spectra of a LGO:Cr phosphor disc. Thermoluminescence curves monitored at 716 nm emission over 20–280 °C. The samples were pre-irradiated by 300 nm UV light for 20 min. The dot-dash-line curve and solid-line curve were acquired at delay times of 10 s and 120 h, respectively. The dash-line curve was acquired on a 120 h-decayed disc after stimulation by 400 nm light for 100 s.

times, as shown in Figure 2.7. The dot-dash-line curve in Figure 2.7 shows the thermoluminescence curve acquired immediately (delay time, 10 s) after the stoppage of 300 nm light irradiation (for 20 min). The curve consists of two broad bands with maxima at 150 °C and 220 °C, which correspond to the shallow and deep traps, respectively. When the delay time increases to 120 h (the solid-line curve in Figure 2.7), a majority of the shallow-trap band disappears and the deep-trap band still exists, indicating that it is the deep traps that are responsible for the super-long persistent luminescence at room temperature. Since the photo-stimulation method has been frequently used to study the photochromic centers in storage

phosphors,[12] we then conducted photostimulated thermoluminescence measurements on the decayed LGO:Cr samples. The dash-line curve in Figure 2.7 shows the thermoluminescence curve of a 120 h-decayed LGO:Cr disc after being exposed to 400 nm illumination for 100 s. Compared with the 120 h-decayed sample without photostimulation, the 400 nm-light stimulation significantly changes the thermoluminescence curve profile, *i.e.*, the deep-trap band intensity decreases while the shallow-trap band reappears. This means that after the 400 nm light photostimulation, some of the electrons in the deep traps are photo-released and the emptied shallow traps are refilled. (Note that the phenomenon of electron transfer from deep traps to shallow traps under external stimulation was also recently observed in some mechanoluminescent materials.[157,158]

2.4.3 Photostimulated persistent luminescence

The photostimulation induced electron trap redistribution, especially the refill of the shallow traps, suggests that photostimulation can affect the persistent luminescence behaviors of the UV pre-irradiated LGO:Cr phosphor. To verify this assumption, we illuminated a 120 h-decayed LGO:Cr disc with 400 nm light for 100 s and measured its persistent luminescence decay curve (monitored at 716 nm), as the brown curve shown in Figure 2.8. Figure 2.8 clearly shows that the 400 nm light illumination increases the persistent luminescence intensity and thus a new PSPL phenomenon occurs. For comparison, we also conducted the same measurement on a completely bleached (*i.e.*, without UV pre-irradiation) LGO:Cr disc, as the grey curve shown in Figure 2.8. No persistent luminescence was observed in the bleached sample after the 400 nm light illumination, which is consistent with the persistent luminescence excitation spectrum shown in the bottom inset of Figure 2.4. The inset of Figure 2.8 is the PSPL emission spectrum of the 120

h-decayed disc, which was recorded at 10 s after the stoppage of the stimulation. The profile of the PSPL emission spectrum is almost identical to that of the photoluminescence emission spectrum (Figure 2.3) and the persistent luminescence emission spectrum (upper inset of Figure 2.4).

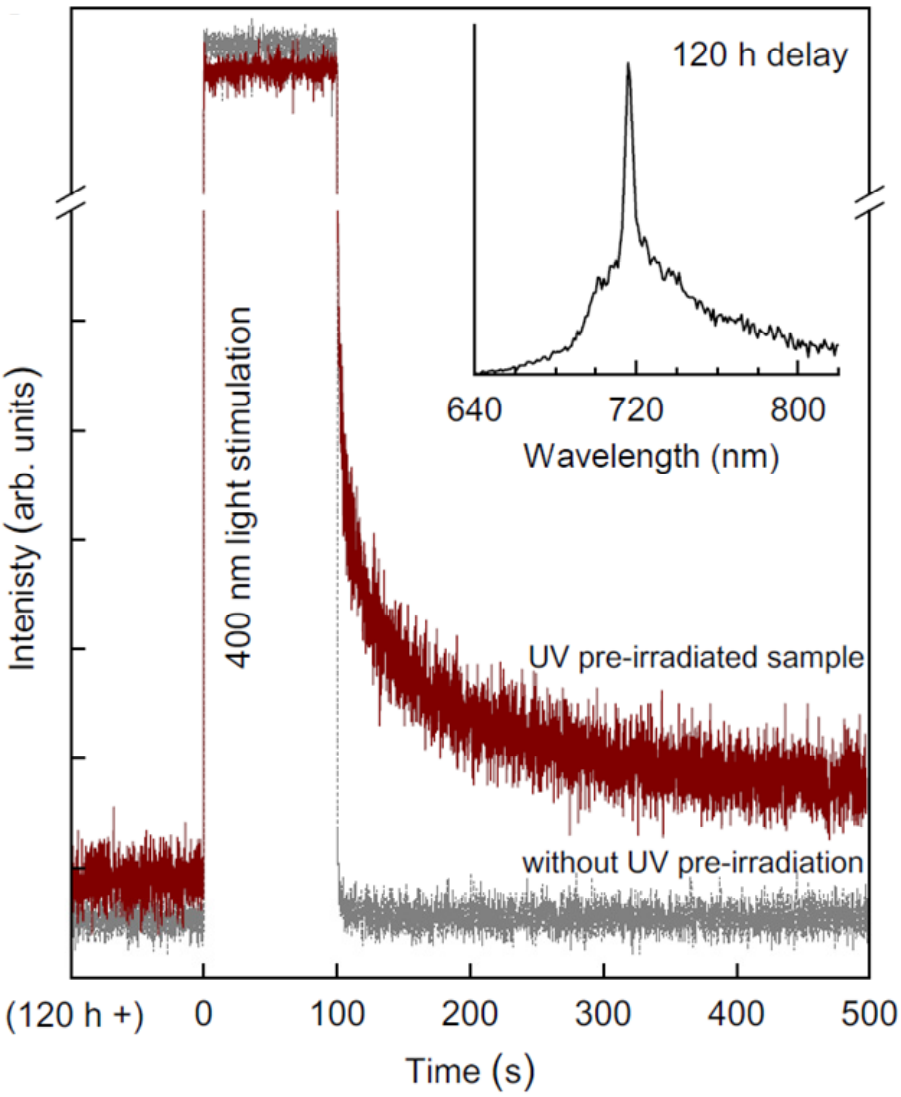

Figure 2.8 PSPL decay curves of a LGO:Cr phosphor disc monitored at 716 nm. The brown curve was acquired on a 120 h-decayed disc (pre-irradiated by 300 nm light for 20 min), while the grey curve was recorded on a bleached disc (without UV pre-irradiation). The inset is the PSPL emission spectrum of the 120 h-decayed disc, which was recorded at 10 s after the stoppage of the stimulation. The wavelength of the stimulation light is 400 nm.

The NIR PSPL phenomenon in LGO:Cr is analogous to the visible PSL in conventional photostimulable storage phosphors, indicating that the LGO:Cr phosphor has the potential to be used as a new type of erasable and rewritable optical memory media for optical information write-in and read-out. For the measurement in Figure 2.8, the write-in and read-out sources are 300 nm UV light and 400 nm visible light, respectively. To precisely determine the range of write-in and read-out energies needed for the NIR PSPL in LGO:Cr, we plotted PSPL write-in and read-out spectra by measuring PSPL decays over a wide range of wavelengths between 250–660 nm. In plotting the PSPL write-in spectrum, we irradiated a bleached LGO:Cr disc using monochromatic UV light between 250–380 nm in 10 nm steps and recorded the persistent luminescence decay curves with and without a 400 nm light stimulation. We defined the PSPL intensity as the difference between the persistent luminescence intensities of each set of decays with and without photostimulation at the time of 10 s after the stoppage of the stimulation. The PSPL write-in spectrum was then obtained by plotting the PSPL intensities as a function of the write-in wavelengths (250–380 nm), as the ball curve shown on the left panel of Figure 2.9. The write-in spectrum reveals that in order to induce NIR PSPL in LGO:Cr, the write-in wavelength should be shorter than 360 nm, and within the measured wavelengths of 250–360 nm the shorter the excitation wavelength the more effective the write-in process is. Moreover, by comparing Figure 2.9 with the bottom inset of Figure 2.4, it can be found that the PSPL write-in spectrum is identical in shape to the persistent luminescence excitation spectrum even though they were obtained by different methods and their physical meanings are different (The PSPL write-in spectrum shows the energy required to fill the deep traps, while the persistent luminescence excitation spectrum reveals the energy needed to photoionize the localized electrons from Cr^{3+} to

the conduction band). The coincidence of these two spectra clearly indicates that the filling of the deep traps accompanies the photoionization of Cr^{3+} in LGO.

In acquiring the PSPL read-out spectrum, the write-in wavelength was fixed at 300 nm, while the read-out wavelengths were tuned between 380–660 nm in 10 nm steps. Using the same method as above, we plotted the PSPL read-out spectrum, as shown on the right panel of Figure 2.9. The read-out spectrum reveals that the PSPL phenomenon can be induced by the entire visible spectrum and that the shorter the stimulation wavelength the more effective the read-out process is. It is worth noting from Figure 2.9 that there is no overlap between the PSPL write-in and PSPL read-out spectra in the LGO:Cr phosphor. This is important because while the visible light is reading the optical information written by the UV light, it does not write new information into the material. In addition, the very broad write-in and read-out spectra allow one to easily find suitable optical sources, such as inexpensive laser diodes and LEDs, for the optical information write-in and read-out processes.

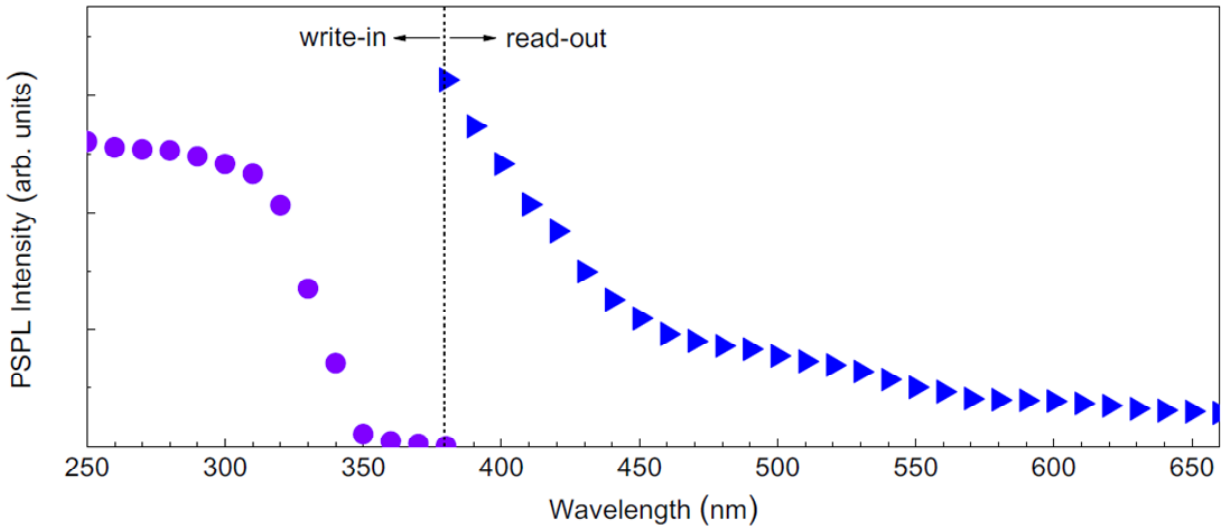

Figure 2.9 Optical write-in and read-out spectra for PSPL in LGO:Cr phosphor discs. Optical write-in spectrum: the ball curve in left panel; optical read-out spectrum: the triangle curve in right panel.

2.5 Luminescence mechanism of $LiGa_5O_8:Cr^{3+}$ phosphors

The above results on PSPL phenomenon in LGO:Cr at room temperature indicates that the PSPL write-in process fills the deep traps with electrons (*i.e.*, forms the photochromic centers), while the PSPL read-out process releases the captured electrons from the filled deep traps (*i.e.*, the photochromic centers) to the conduction band, followed by the refill of the emptied shallow traps. To gain insight into the interaction between the traps and the Cr^{3+} emitting centers, we conducted extended thermoluminescence measurements starting at liquid nitrogen temperature (−196 ˚C, *i.e.*, 77 K) and decay measurement at 77 K on LGO:Cr discs, as shown in Figure 2.10 and Figure 2.11, respectively.

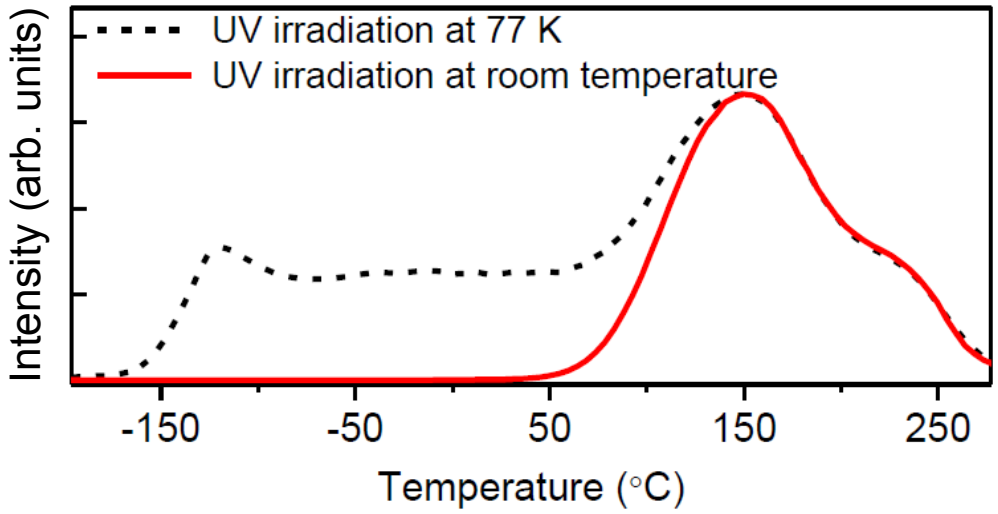

Figure 2.10 Low-temperature thermoluminescence in LGO:Cr phosphor discs. Thermoluminescence curves recorded by monitoring at 716 nm emission over −196–280 °C (77–553 K) on a LGO:Cr disc. The dash-line curve and solid-line curve were recorded after 300 nm UV light irradiations for 20 min at 77 K and at room temperature, respectively.

Figure 2.10 shows two thermoluminescence curves recorded over −196–280 °C (*i.e.*, 77–553 K) after irradiating the samples with 300 nm UV light for 20 min at 77 K (dash-line curve) and at room temperature (solid-line curve). (For the case of room-temperature irradiation, the sample was quickly transferred to liquid nitrogen environment for measurement after the stoppage of the

irradiation.) In high-temperature region (from room temperature to 280 °C), the two curves exhibits the same profile. In low-temperature region (from 77 K to room temperature), however, the 77 K pre-irradiated sample shows an additional thermoluminescence band, while the room-temperature pre-irradiated sample does not. This means that there exist low-temperature trap levels in LGO:Cr, but these low-temperature traps are inactive (*i.e.*, emptied) during room temperature irradiation due to the thermal energy available at room temperature. This trap information indicates that the low-temperature traps will not contribute to the persistent luminescence at 77 K for the samples irradiated at room temperature.

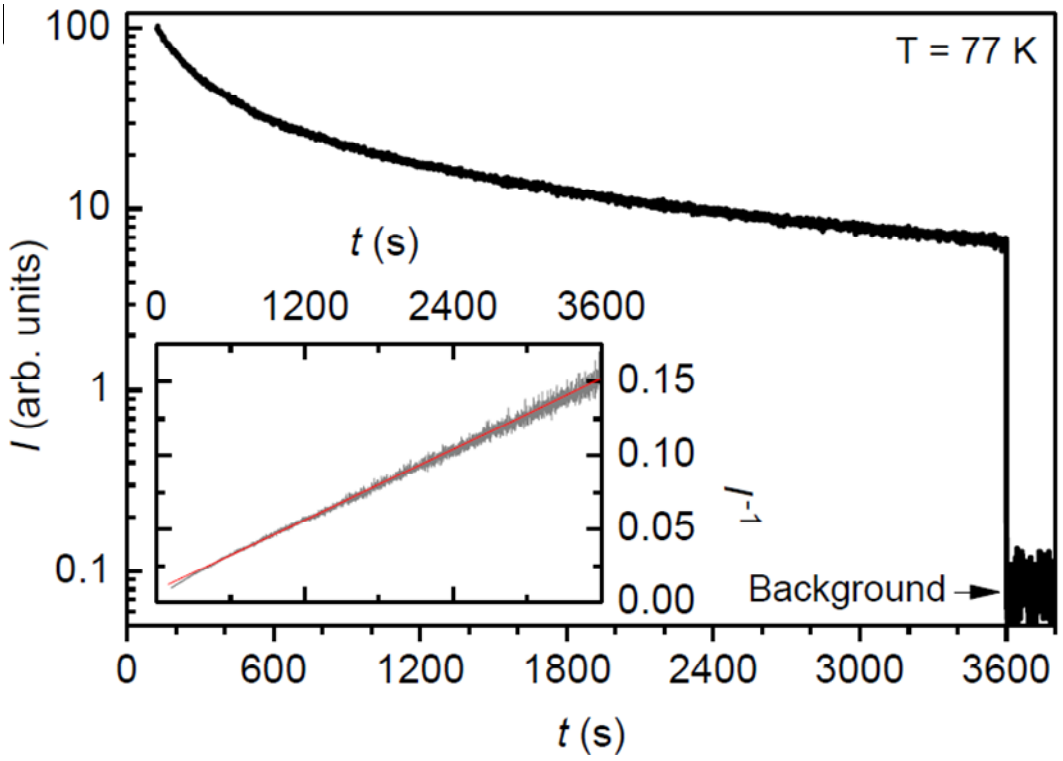

Figure 2.11 Low-temperature persistent luminescence measurements in LGO:Cr phosphor discs. Persistent luminescence intensity (I) monitored at 716 nm as a function of time (t) at 77 K for a LGO:Cr disc pre-irradiated at room temperature. Inset shows the same data plotted as I^{-1} versus t.

Figure 2.11 shows a decay curve measured at 77 K for a LGO:Cr disc pre-irradiated at room temperature. Before immersing the sample into liquid nitrogen for the measurement, the sample

was irradiated by 300 nm light at room temperature for 20 min. The interval between the stoppage of the room-temperature irradiation and the starting of the low-temperature measurement is 120 s. This decay curve was also plotted as a function of reciprocal persistent luminescence intensity versus time, as the linear curve shown in the inset of Figure 2.9. The presence of low-temperature persistent luminescence without the contribution from the low-temperature traps and the linear dependence of the reciprocal persistent luminescence intensity versus time are characteristics of a quantum tunneling process,[159,160] meaning that at 77 K the electrons captured in the deep traps can directly recombine with the nearby ionized Cr^{3+} ions *via* quantum tunneling, instead of going through the conduction band.[8] This tunneling process, which is temperature independent, proceeds at a slow rate, which on the one hand leads to the super-long-persistent luminescence at room temperature, and on the other hand maintains the electron population in the deep traps for a long time for the PSPL process.

Based on the above results and discussions, we propose a mechanism to account for the super-long NIR persistent luminescence and the new NIR PSPL phenomenon at room temperature in LGO:Cr, as schematically shown in Figure 2.12.[18] To simplify the description, we assign the shallow traps and the filled deep traps (*i.e.*, the photochromic centers) in the PSPL process as TRAP-1 and TRAP-2, respectively. Under UV (250–360 nm) excitation, the ground-state electrons of Cr^{3+} ions are photoionized to the conduction band (process 1). The conduction electrons are subsequently captured by TRAP-1 (process 2) and TRAP-2 (process 3). In the initial stage of the persistent luminescence process, the electrons captured in TRAP-1 escape thermally *via* the conduction band (process 4) and recombine with the ionized Cr^{3+} ions, which dominates the initial intense persistent NIR emission. Several hours later, the release of electrons

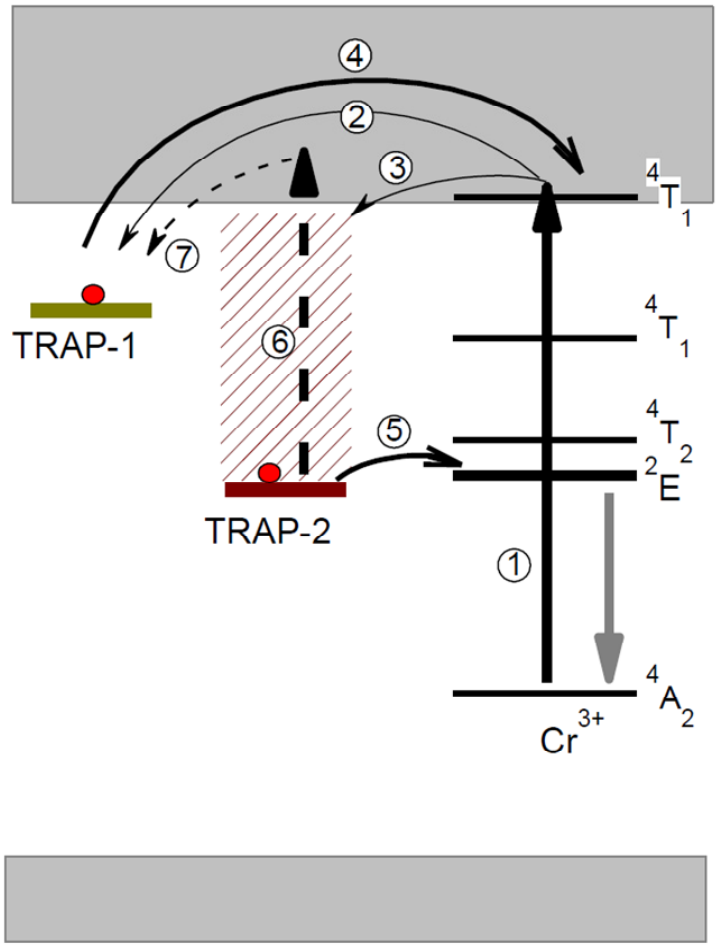

Figure 2.12 Schematic representation of NIR persistent luminescence and photostimulated NIR persistent luminescence mechanisms in LGO:Cr. The straight-line arrows and curved-line arrows represent optical transition and electron transfer processes, respectively.

through the conduction band can be neglected due to the depletion of TRAP-1. The NIR persistent luminescence subsequently originates mainly from TRAP-2 *via* quantum tunneling (process 5), giving weak but very-long NIR persistent luminescence. Under the stimulation of a visible or NIR light for a short time at room temperature, some of the electrons in TRAP-2 can be photo-released to the conduction band (process 6) and some of which refill the depleted TRAP-1 (process 7), resulting in enhanced persistent luminescence, *i.e.*, the PSPL phenomenon. Since only some of the electrons in TRAP-2 can be photo-released after photostimulation (owing

to short-time, moderate-intensity light stimulation, *e.g.*, an 85-lumen white LED for 20 s in the present study), the PSPL phenomenon can thus occur many times.

2.6 Summary

In summary, we have synthesized a novel Cr^{3+}-doped $LiGa_5O_8$ (LGO:Cr) NIR persistent phosphor that exhibits a super-long NIR persistent luminescence of more than 1000 h, which is the longest persistent luminescence reported to date. Remarkably, the LGO:Cr phosphor is also a superb photostimulable storage medium – the energy stored in the deep traps of the material can be liberated by photo-stimulation as intense NIR persistent luminescence signal, for multiple times over a very-long period of time (>2000 h), by short exposure (tens of seconds) to a white LED illumination – a new phenomenon that we referred to as PSPL. This NIR LGO:Cr phosphor can be used as a promising storage medium for long-time optical information storage and read-out. It is expected to find many other technologically important applications in security and medical diagnosis. For example, Since the LGO:Cr phosphor emits highly penetrating NIR light and the UV pre-irradiated samples can be repeatedly stimulated by long-wavelength light (visible and NIR light), the material in the form of nanoparticles may act as ideal optical probes for long-time *in vivo* deep-tissue bio-imaging.

CHAPTER 3

SYNTHESIS, CHARACTERIZATION AND SURFACE MODIFICATION OF CHROMIUM-DOPED LITHIUM GALLIUM OXIDE NANOPARTICLES

3.1 Introduction

Bulk LGO:Cr phosphor exhibits a super-long NIR persistent luminescence (peaking at 716 nm) after minutes of UV irradiation and intense NIR PSPL with short exposure to a white LED illumination, as presented in Chapter 2. These unique, novel optical properties suggest that LGO:Cr material in the form of nanoparticles can act as ideal self-illuminating NIR optical nanoprobes for long-term deep-tissue *in vivo* bioimaging. In this chapter, we report NIR persistent luminescence and PSPL properties from LGO:Cr nanoparticles synthesized by a sol-gel method followed by calcination. The LGO:Cr nanoparticles exhibit persistent luminescence and PSPL in the ~650–850 nm wavelength range (peaking at 716 nm) with an persistent luminescence time of more than ~100 h and an PSPL time of more than ~200 h at room temperature. For using LGO:Cr nanoparticles in *in vivo* experiments, surface modification of LGO:Cr nanoparticles is achieved by polymer coating (*i.e.*, PEI and PVP) and silica coating. LGO:Cr nanoparticles are also conjugated with cyclic Arg-Gly-Asp-D-Tyr-Lys [c(RGDyK)] peptides for *in vivo* targeted imaging.

3.2 Synthesis and measurements of $LiGa_5O_8:Cr^{3+}$ nanoparticles

3.2.1 Synthesis of LGO:Cr nanoparticles

The LGO:Cr nanoparticles were synthesized by a sol-gel method followed by calcinations at high temperature.[18] The synthesis process is briefly described as follows. A solution was

prepared by dissolving stoichiometric amount of 0.19 g lithium nitrate ($LiNO_3$, 99%, Alfa Aesar), 5.0 g gallium nitrate ($Ga(NO_3)_3$, 99.999%, Alfa Aesar), and 1.65 mg chromium nitrate ($Cr(NO_3)_3$, 98.5%, Alfa Aesar) into 44 mL methanol. The solution was then stirred for several hours on a magnetic stirrer. During the stirring process, a chelating agent, 5.0 mL acetylacetone (>99%, TCI America), was added into the solution to form chelate complexes. Aqueous ammonium solution (28 vol.%, J.T. Baker) was also added to stabilize the complexes and to adjust the pH of the sol to 8.4. When a homogeneous sol was formed, the solution was heated to 90 ˚C for several hours to form a dry gel. The dry gel was then calcinated in a muffle furnace at 1100 ˚C for 3 hours to form LGO:Cr particles with desirable NIR persistent luminescent properties. Since most of the as-calcinated particles are larger than 200 nm due to sintering, to obtain small nanoparticles in large scale (gram scale), the as-calcinated particles were wet grinded using a ball milling equipment (JBM-B035, Just Nanotech Co.) in 2-propanol medium. The grinded particles were suspended in 5 mM $NaOH_{(aq)}$ by ultrasonication and then filtered by 0.1 μm membrane filters (Supor-100, PALL life Sciences). The LGO:Cr nanoparticles suspended in the filtered suspension were then collected by centrifugation for subsequent use.

3.2.2 Measurements of LGO:Cr nanoparticles

The crystal structure of the as-synthesized materials was measured using a conventional powder X-ray diffractometer (XRD, PANalytical) with CuKα radiation (λ = 1.5406 Å). The diffraction patterns were analyzed using Crystallographica Search-Match (Version 2.1.1.0, Oxford Cryosystems Ltd.). The morphology and microstructure were studied using a transmission electron microscope (TEM, Hitachi HF-3300 STEM). The composition of the as-synthesized materials was analyzed using a inductively coupled plasma mass spectrometer (ICP-

MS, VG PlasmQuad 3). For ICP-MS measurements, 3 mg sample was mixed with 30 ml of 2% $HNO_{3(aq)}$ in a sealed sample vial, The sealed vial was heated at 120 ˚C until the sample dissolved in the aqueous solution. The solution was cooled down to room temperature and then diluted by 200 times with 2% $HNO_{3(aq)}$ for measurement.

The optical properties of the as-synthesized nanoparticles were measured by using a Horiba Fluorolog-3 spectrofluorometer, as mentioned in Section 2.4. The data acquired include photoluminescence emission and excitation spectra, persistent luminescence emission spectra, persistent luminescence decay curves, PSPL emission spectra and PSPL decay curves. To elicit the PSPL signal, a white LED (Olight, SR51) was used as the stimulation source.

NIR persistent luminescence and PSPL photos of the samples were taken in a dark room using a camera which was connected to a night vision monocular, as mentioned in Section 2.4. 250 mg LGO:Cr nanoparticles were pressed into a 20 mm-diameter disc. Before imaging, the sample was irradiated by a 254 nm UV lamp for 15 min. NIR persistent luminescence photos were then taken at different delay times (up to 96 h). After 96 h nature decay, the disc was illuminated by a Olight SR51 white LED flashlight for 10 s, and NIR PSPL photos were taken at 10 s and 1 h after the flashlight stimulation.

The persistent luminescence performance of LGO:Cr nanoparticles at different pH was also evaluated. LGO:Cr nanoparticles were dispersed in 1× PBS buffer solutions with pH values ranging from 3.0 to 11.0. The particle concentrations were all at 0.1 mg/mL. After 24 h incubation, the solutions were irradiated by a 254 nm UV lamp for 15 min. The intensities of the NIR persistent luminescence (in photons per second) were then acquired on an IVIS Lumina II imaging system.

3.3 Properties of $LiGa_5O_8:Cr^{3+}$ nanoparticles

3.3.1 Structure and morphology of LGO:Cr nanoparticles

Figure 3.1 is the XRD pattern of the as-synthesized LGO:Cr nanoparticles. The pattern can be indexed as cubic $LiGa_5O_8$, consistent with PDF No. 76-199. TEM study shows that nanoparticles have irregular shape with sizes ranging from 50 to 100 nm (Figure 3.2). The

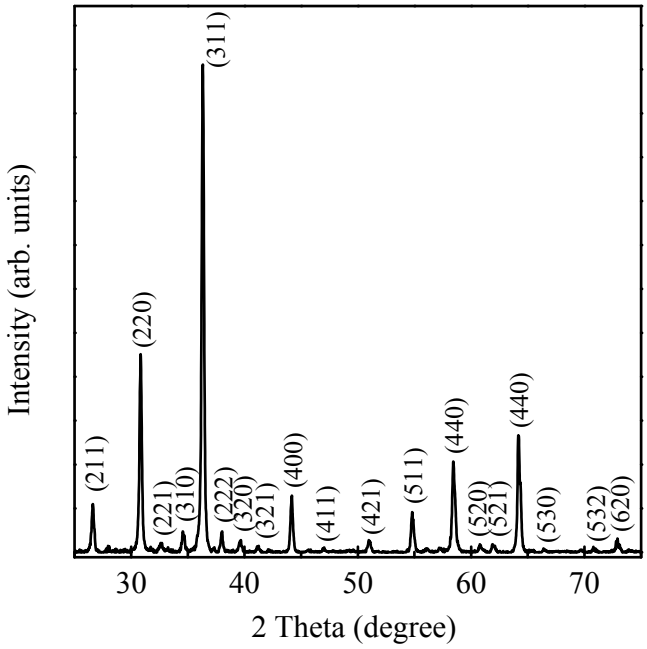

Figure 3.1 XRD pattern of LGO:Cr nanoparticles.

concentration of as-prepared LGO:Cr nanoparticles for ICP-MS analysis was 50 ng/mL. Element analysis using an ICP-MS system reveals that the concentrations of Li, Ga and Cr are 990, 71340 and 18.6 ppb, respectively (Table 3.1), which are at the same order of the designed concentrations.

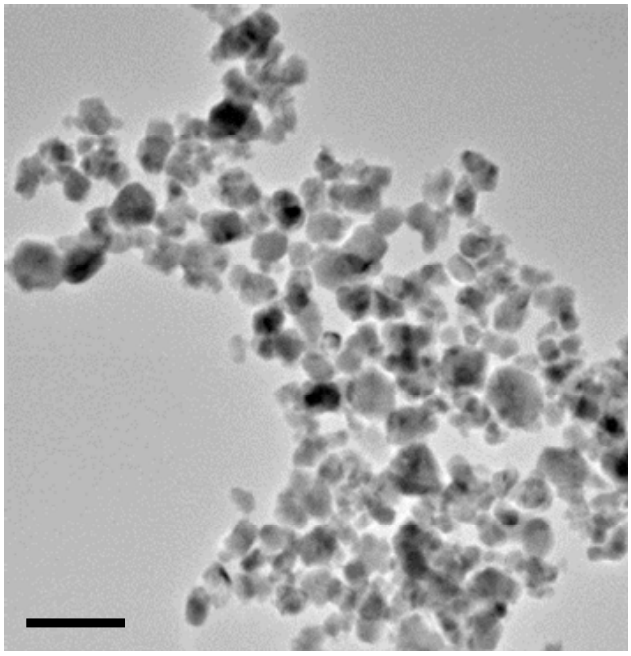

Figure 3.2 TEM image of LGO:Cr nanoparticles. (Scale bar, 200 nm)

Table 3.1 Element analysis of LGO:Cr nanoparticles

	Li (ppb)	Ga (ppb)	Cr (ppb)
LGO:Cr nanoparticles	990 ± 164	71340 ± 634	18.6 ± 2.8
Theoretic concentration	1435	72095	32.3

3.3.2 Optical properties of LGO:Cr nanoparticles

The LGO:Cr nanoparticles exhibit the similar optical properties as the LGO:Cr ceramics. Figure 3.3 shows the normalized photoluminescence emission and excitation spectra of the LGO:Cr nanoparticles. Under excitation at 400 nm, the LGO:Cr nanoparticles exhibits a narrow-band emission peaking at 716 nm (Figure 3.3), which is attributed to the spin-forbidden $^2E \rightarrow {}^4A_2$ transition of Cr^{3+} ions.[18,154] The associated broad background emission ranging from ~650 to ~800 nm originates mostly from the phonon sidebands of the $^2E \rightarrow {}^4A_2$ transition.[154] The LGO:Cr nanoparticles can be effectively excited by light of a broad range of wavelengths (from ~250 nm to ~660 nm). This photoluminescence excitation spectrum consists of three main excitation

bands originating from the inner transitions of Cr^{3+}, including the 300 nm band originating from the $^4A \rightarrow {}^4T_1$ transition, the 415 nm band originating from the $^4A \rightarrow {}^4T_1$ transition and the 605 nm band originating from the $^4A \rightarrow {}^4T_2$ transition.[154]

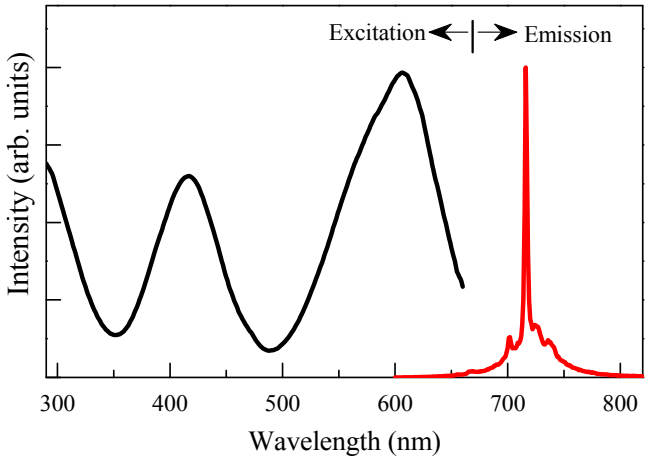

Figure 3.3 Normalized photoluminescence excitation and emission spectra of LGO:Cr nanoparticles. The excitation spectrum was obtained by monitoring at 716 nm emission. The emission spectrum was excited by 400 nm.

As their bulk counterpart (*i.e.*, LGO:Cr solid ceramic), the LGO:Cr nanoparticles also exhibit very long lasting NIR persistent luminescence after the removal of the excitation source. Figure 3.4 shows the persistent luminescence decay curve of LGO:Cr nanoparticles monitored at 716 nm after irradiation by a 254 nm UV lamp for 15 min. The recording lasts for 24 h. It is clear that after 24 h of persistent emission, the persistent luminescence intensity is still significantly high, meaning that the NIR afterglow should last much longer than 24 h. Indeed, when monitored using a night-vision goggle, the NIR emission from the LGO:Cr nanoparticles can be clearly observed even after 96 h natural decay, as shown in Figure 3.5a–c. The inset of Figure 3.4 is the persistent luminescence emission spectrum recorded at 10 s after the UV irradiation. The profile of the persistent luminescence spectrum is almost identical to that of the photoluminescence emission spectrum (Figure 3.3), indicating that the NIR persistent luminescence originates from

the Cr^{3+} emitting centers. Note that, unlike the NIR photoluminescence which can be excited by a wide range of wavelength (~250–660nm), the NIR persistent luminescence in LGO:Cr nanoparticles can only be induced by UV light irradiation.[18]

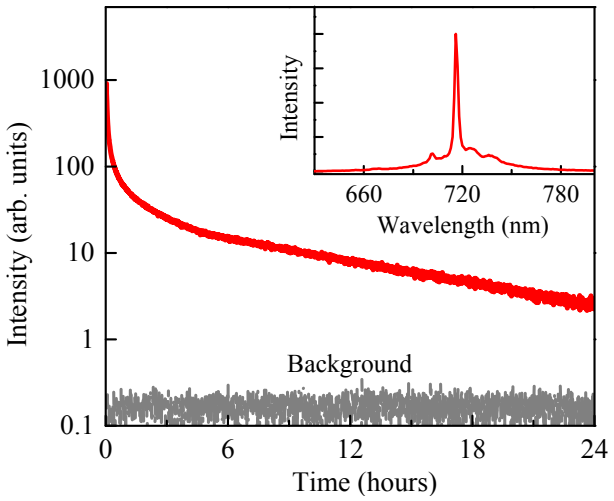

Figure 3.4 NIR persistent luminescence decay curve of LGO:Cr nanoparticles. The decay curve (red) was monitored at 716 nm after irradiation by a 254 nm UV lamp for 15 min. The bottom curve is the background. The inset is the persistent luminescence emission spectrum recorded at 10 s after the UV irradiation.

When the persistent luminescence signal becomes weak owing to the emptying of the shallow traps, short illumination by a white LED flashlight can stimulate the release of some of electrons in the deep traps to refill the emptied shallow traps, resulting in the rejuvenation of the persistent luminescence *via* a PSPL mechanism, as the NIR images shown in Figure 3.5.[18] The PSPL phenomenon occurs only in the UV pre-charged LGO:Cr nanoparticles disc (the red curve in Figure 3.6). Without the UV pre-irradiation, LGO:Cr nanoparticles stimulated by a white LED illumination did not produce PSPL signal (the grey curve in Figure 3.6), because the energy of

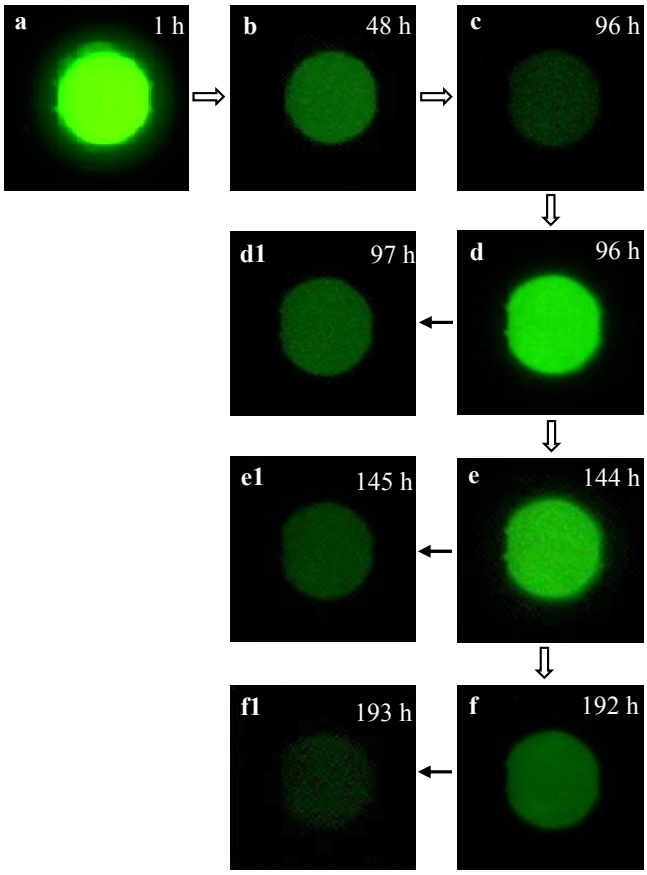

Figure 3.5 NIR images for persistent luminescence and PSPL in LGO:Cr nanoparticles disc at room temperature. **a**–**c**, Natural decay of persistent luminescence to 96 h. **d**–**f**, NIR PSPL up to 192 h. Starting from the 96 h time point, the sample was stimulated daily by a white LED flashlight. PSPL images (**d**–**f**) were taken at 10 s after the stimulation. Images (**d**1–**f**1) were taken at 1 h after the stimulation.

the white light is too low to photoionize the localized electrons from Cr^{3+} to the conduction band to fill the traps. The resulting PSPL signal can last for up to 1 h, and the process can be repeated multiple times (>10 times) over a period of about two hundred hours (Figure 3.5d–f). The upper inset of Figure 3.6 shows the PSPL emission spectrum recorded at 10 s after the stimulation. The profile of the PSPL emission spectrum is identical to that of the photoluminescence emission

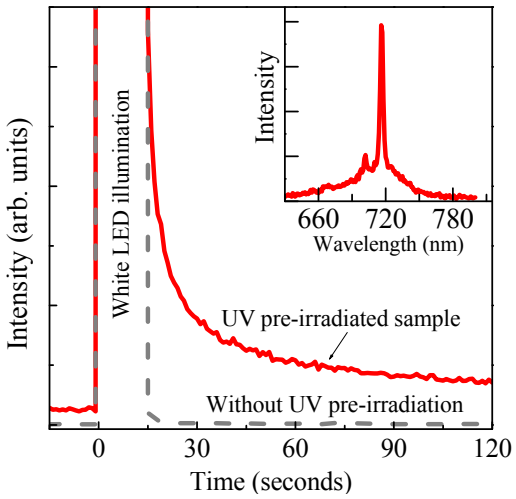

Figure 3.6 NIR PSPL decay curves and emission spectra of LGO:Cr nanoparticles. The red solid curve was acquired on a 24 h decayed sample (pre-irradiated by a UV lamp), while the grey dash line curve was recorded on a bleached sample (without UV pre-irradiation). The inset is the PSPL emission spectrum of the 24 h decayed sample, which was recorded at 10 s after the stimulation.

spectrum (Figure 3.3) and the persistent luminescence emission spectrum (upper inset of Figure 3.4), indicating that the NIR PSPL originated from the Cr^{3+} emitting center. Overall, like their bulk counterparts in Section 2.5, the LGO:Cr nanoparticles exhibit strong NIR photoluminescence, very-long NIR persistent luminescence, and multiple NIR PSPL.

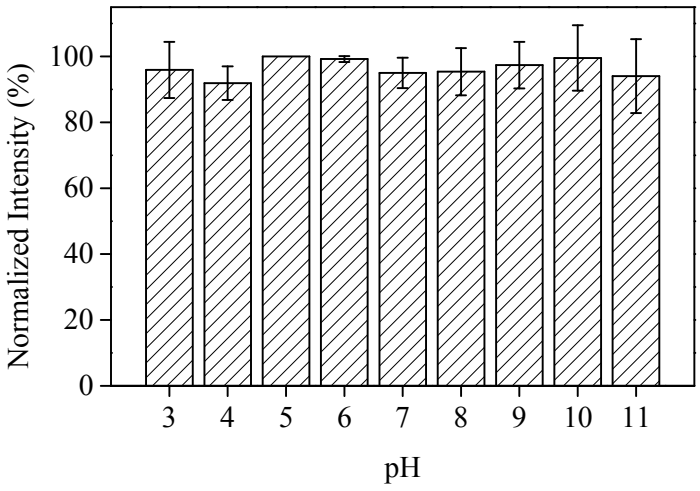

Figure 3.7 Persistent luminescence performance of LGO:Cr nanoparticles at different pH**.**

For bioimaging applications, the LGO:Cr nanoparticles have to be stable in biological environments. To test the stability of LGO:Cr nanoparticles, we measured the persistent luminescence intensities at different pH conditions. The LGO:Cr nanoparticles were found to be stable over a broad range of pH from 3.0 to 11.0, as shown in Figure 3.7.

3.4 Surface modification and functionalization of $LiGa_5O_8:Cr^{3+}$ nanoparticles

The discussion in Section 1.5 shows that surface modification and encapsulation of nanoparticles provides the opportunity to engineer the nanoparticle surface without aggregations. Various types of nanoparticles, including inorganic, organic, metal, metal oxide and semiconductor nanoparticles, can be modified and encapsulated by organic ligands and polymers for diverse biomedical applications. This is also true for the LGO:Cr nanoparticles.

For LGO:Cr nanoparticles, it is impossible to do surface modification during synthesis, because high temperature calcination removed all organic residues on particle surfaces. The reliable way to modify the LGO:Cr nanoparticles is to attach small organic ligands through ligand exchange. During ligand exchange at the surfaces of nanoparticles, the incoming ligands exchange outgoing surface ligands, which have the same charges and occupy the same number of coordination site. Small organic ligands such as citrates, cysteine, dimercaptosuccinic acid, cetyltrimethylammonium bromide have been used in metal oxide nanoparticles for stabilizing the nanoparticles, but such kinds of small organic modifiers only stabilized LGO:Cr nanoparticles for several hours, due to the weak interactions between these monodentate ligands and the surfaces of LGO:Cr nanoparticles. Therefore, multidentate macro-molecules, including PEI, PVP, human serum albumin (HSA), and permanent silica coating were adopted in this study.

3.4.1 Polymer coated LGO:Cr nanoparticles

Experiments. Two polymers, polyethylenimine (PEI, MW = 25K) and polyvinylpyrollidone (PVP, MW = 40K), were used to coat the LGO:Cr nanoparticles. 1 mg/mL LGO:Cr nanoparticles suspension were prepared in 12.5 wt% $PEI_{(aq)}$, 10 wt% $PVP_{(aq)}$ and 2.5 wt% PVP in ethanol solutions. The suspension stability was monitored. The morphology of the coated nanoparticles was measured using a field emission gun scanning electron microscope (FEG-SEM, FEI Inspect F).

Results and discussion. LGO:Cr nanoparticles in 12.5 wt% PEI aqueous solution were stable for at least 72 h. (Figure 3.8). SEM imaging (Figure 3.9) shows that PEI-coated LGO:Cr (PEI-LGO:Cr) nanoparticles were well dispersed. This is because at high concentration of PEI, the surfaces of nanoparticles adsorb positively charged PEI molecules. As a result, the repulsive forces between the positively charged nanoparticles prevent them for aggregating.[161] PVP is also considered as popular polymeric dispersants to form PVP coating for stabilizing nanoparticles in water.[149] The PVP coated nanoparticles later can conjugate with other molecules *via* ligand exchange. In 10 wt% PVP aqueous solution, the LGO:Cr nanoparticle suspension was stable for at least 48 h (Figure 3.10). In ethanol solution, however, only at least 2.5 wt% PVP was found to keep LGO:Cr nanoparticles suspension stable for more than 96 h (Figure 3.11).

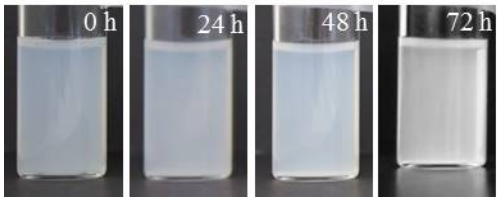

Figure 3.8 Stability of 12.5 wt% PEI encapsulated LGO:Cr nanoparticles in water.

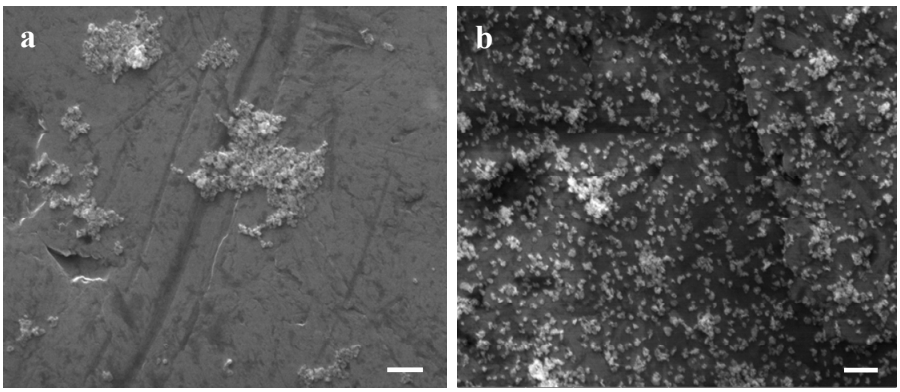

Figure 3.9 SEM images of LGO:Cr nanoparticles. **a**, LGO:Cr nanoparticles without coating. **b**, PEI coated LGO:Cr nanoparticles. (Scale bar, 1 μm)

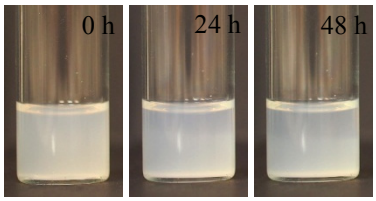

Figure 3.10 Stability of 10 wt% PVP encapsulated LGO:Cr nanoparticles in water

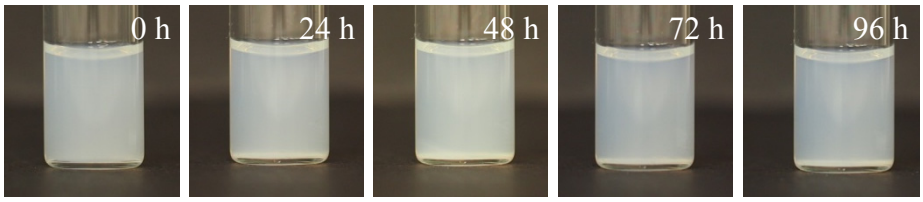

Figure 3.11 Stability of 2.5 wt% PVP encapsulated LGO:Cr nanoparticles in ethanol.

3.4.2 Silica coated LGO:Cr nanoparticles

Experiments. The LGO:Cr nanoparticles (>200 nm) were coated with silica shells using a sol-gel procedure. PVP coated LGO:Cr (PVP-LGO:Cr) nanoparticles prepared in Section 3.4.1 were treated with TEOS in a solution of 4% (v/v) aqueous ammonia in ethanol. PVP acted as a dispersive agent in ethanol, and the PVP molecules left the surfaces of LGO:Cr nanoparticles once the TEOS attached to the surfaces *via* ligand exchange. The silica shell thickness was

determined by the reaction time and the amount of TEOS. The morphology of silica coated LGO:Cr nanoparticles was studied using FEG-SEM (Zeiss, Sigma VP) and TEM.

Results and discussion. The average size of silica coated LGO:Cr nanoparticles is 211.9 ± 52.1 nm (Figure 3.12a), when starting with LGO:Cr nanoparticles with size of ~200 nm. The thickness of silica coating can be tuned from 1 nm to 10 nm by adjusting the reaction time and the concentration of TEOS (Figure 3.12b and Table 3.2).

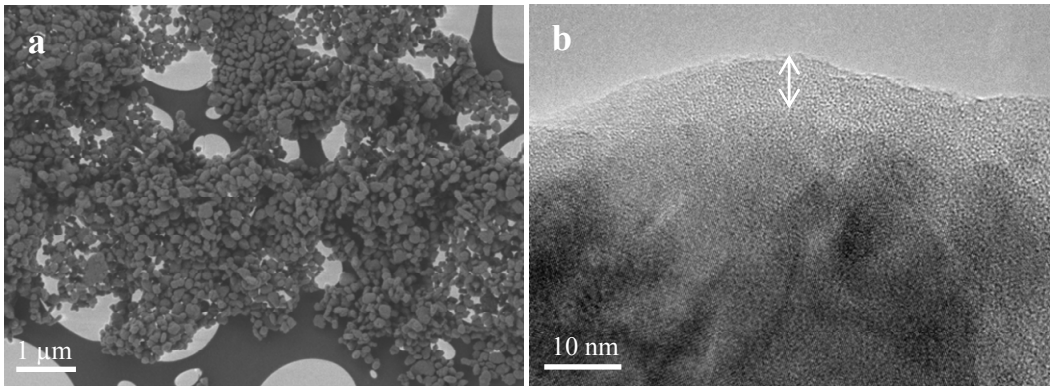

Figure 3.12 Electron microscopy images of silica coated LGO:Cr nanoparticles. **a**. SEM image of silica coated LGO:Cr nanoparirlces. **b**. TEM image of silica coated LGO:Cr nanoparticles. The thickness of silica layer is indicated by a double arrow.

Table 3.2 The thickness of silica layer prepared in different reaction conditions

		Silica Thickness (nm)		
Reaction Time (h)		2	4	6
TEOS/LGO (μL/mg)	1.0	1.3 ± 0.4	2.2 ± 0.4	3.1 ± 1.0
	2.5	4.2 ± 0.7	6.2 ± 1.0	7.6 ± 1.8
	5.0	5.1 ± 1.6	8.4 ± 1.2	13.4 ± 2.5

3.5 Summary

We have synthesized novel photostimulable $LiGa_5O_8:Cr^{3+}$ (LGO:Cr) nanoparticles by a sol-gel method followed by calcination at 1100 °C. The LGO:Cr nanoparticles are crystalline and have diameters in the range of 50–100 nm. The LGO:Cr nanoparticles exhibit long NIR (peaking at 716 nm) persistent luminescence of more than 100 h after minutes of UV irradiation. Remarkably, the LGO:Cr nanoparticles are also superb photostimulable storage medium – the energy stored in the deep traps of the materials can be liberated by photo-stimulation as intense NIR persistent luminescence signal, for multiple times over a long period of >200 h, by short exposure (tens of seconds) to a white LED flashlight illumination through a PSPL mechanism. The 716 nm persistent luminescence and PSPL emission is in the transparency window of tissues. The LGO:Cr nanoparticles can be readily encapsulated by PEI and PVP polymers, coated by silica shells. All these properties indicate that the LGO:Cr nanoparticles are the ideal nanoscale optical probes for long-duration, deep-tissue bioimaging.

CHAPTER 4

CELL UPTAKE OF CHROMIUM-DOPED LITHIUM GALLIUM OXIDE NANOPARTICLES

4.1 Introduction

The results in Chapter 3 show that the LGO:Cr nanoparticles are the ideal optical nanoprobes for *in vivo* bioimaging applications. Before *in vivo* imaging, however, extensive *in vitro* experiments are needed to evaluate the toxicity of the nanoparticles to cells, as well as the capacity of cells to uptake the nanoparticles. The most common way to evaluate the toxicity of nanomaterials is *in vitro* cytotoxicity study using different cell lines and different incubation conditions. *In vitro* cytotoxicity study can determine the viability of cells in a population based on plasma membrane integrity and esterase activity.[166-168] The results can be examined by flow cytometry, fluorescence microscopy, fluorescence microplate readers, and cells counting.

Mammalian cells can uptake and internalize nanoparticles *via* deformation of the membrane and generation of membrane-bound carriers. This endocytosis process involves various endocytic mechanisms, including phagocytosis and pinocytosis.[167-169]

Phagocytosis in mammals is performed only by immune cells, such as dendritic cells, mast cells, macrophages, and neutrophils. Immune cells can clear large pathogens, dead cells and cell debris *via* phagocytosis, which is triggered by specific cell-surface receptors and Rho-family GTPases.[170] This process directs a cup-shaped membrane distortion that gradually engulfs the particles. The distortion of the membrane ends with the formation of a phagosome, with shape and size, dictated by the up-taken materials, as large as 5–10 μm.[161-173] The phagosome cargo travels to a specific subcellular organelle. Pinocytosis can happen in almost any eukaryotic cell

and is further sub-classified by the different membrane proteins and lipids into several mechanisms, including clathrin-, caveolae-, RhoA-, CDC42-, ARF6-, and flotillin- mediated endocytosis, except for macropinocytosis.[167,174-178] Macropinocytosis, unlike the above mentioned endocytosis mechanisms and phagocytosis, is an actin-regulated endocytoic process that is not directly driven by the cargo or the receptors associated with it.[167,169,179]

For increasing the cell uptake efficiency of nanoparticles, polycationic polymers such as poly-L-lysine (PLL) and PEI are widely used as transfection agents in cell labeling and gene transfection because they facilitate cell internalization.[180-183] PLL, *via* electrostatic interactions, can complex negatively charged superparamagnetic iron oxide nanoparticles such as FDA-approved Feridex® and chaperon, and then facilitates the detection of the labeled stem cells' migration by MRI.[183] PEI with high positive charge density (20–25 mEq/g) facilitates ionic interaction with negatively charged molecules, *via* the protonation of amine groups taken from the surrounding medium. Two types of PEI are used in transfection: branched PEI (mainly of molecular weights 25 and 800 KDa) and linear PEI (22 kDa).[184,185] Branched PEI has three kinds of amine groups – primary, secondary and tertiary – with an amine ratio of 1:2:1, while linear PEI amines are exclusively secondary. Thus, while linear PEI acquires its positive charge density through the protonation of secondary groups, branched PEI possesses additional primary amine groups for protonation. In addition to being most basic and also most reactive, the primary amine groups are amenable to chemical modification and have been used to covalently attach different types of molecules with the aim of conferring additional properties to the vector. Nucleic acid-PEI binding slightly changes the PEI protonation profile, one-half to one-third of the amine groups being protonated at physiological pH. Therefore, in contrast to PLL, PEI possesses a great buffering capacity over a very wide pH range.[186]

4.2 Cytotoxicity study of polyethylenimine coated $LiGa_5O_8:Cr^{3+}$ (PEI-LGO:Cr) nanoparticles

To understand the toxicity of nanoparticles, we need to accurately measure how they are distributed in the body after exposure, and how they interact with pertinent organs and cells. Ideally, biodistribution studies should be performed *in vivo*, but *in vitro* models are often needed for ethical and practical reasons.[187,188] In present study, the cytotoxicity of the PEI-LGO:Cr nanoparticles were evaluated on three cell lines: 4T1 murine breast cancer cells, RAW264.7 murine macrophage cells, and murine embryonic stem cells (ESCs).

Experiments. Purified PEI-LGO:Cr nanoparticles were dispersed in 1× phosphate buffered saline (PBS, pH 7.4, 0.067 M, HyClone, Thermo SCIENTIFIC) as a stock solution. In preparing the assays of 4T1 cells and RAW264.7 cells, the cells (2×10^4/well) were added to the stock solution of PEI-LGO:Cr nanoparticles with concentrations varying from 0 to 100 μg/mL, and co-incubated in a 24-well plate for 24 h in RPMI-1640 medium with 10% fetal bovine serum. The incubated cells were collected by trypsin treatment, followed by centrifugation and re-suspension in 0.01 M PBS (1×, pH 7.4). A Trypan blue solution (0.4%, w/v) was then added into the suspension and the dead cells were counted under a microscope using a hemacytometer. In preparing the mouse ESCs assay, the cells (0.5×10^4/well) were cultured in 0.1% gelatin-coated 96-well plates using DMEM (Hyclone) medium supplemented with 10% FBS, 10% KSR (Gibco), 1% non-essential amino acids, 4 mM L-glutamine, 100 U/ml penicillin, 100 μg/ml streptomycin, 0.1 mM β-mercaptoethanol, and 1000 U/mL leukemia inhibitory factor (ESGRO, Chemicon). The cells were maintained in a humidified cell culture incubator at 37 °C under 5% CO_2. After 12 h of incubation, the wells were replenished with fresh medium and treated with various concentrations of PEI-LGO:Cr nanoparticles (0−100 μg/mL) for 72 h, followed by

addition of WST8 solution for 1 h. The plates were read at 450 nm using an OPTImax microplate reader (Molecular Devices), and the percentage of cell viability was then calculated. For all the three types of cells, the measurement at each concentration of PEI-LGO:Cr nanoparticles was repeated 3 times.

The impacts of PEI-LGO:Cr nanoparticles on the renewal and differentiation of mouse ESCs were studied by analyzing three key biomarkers: Nanog, Nestin and Sox17 (Table 4.1). A stock solution of PEI-LGO:Cr nanoparticles was first sterilized in an autoclave. Mouse ESCs (0.5×10^4/well) were cultured in 0.1% gelatin-coated 96-well plates using DMEM (Hyclone)

Table 4.1 Summary of information of the primers associated with cell pluripotency.

Primer	Primer Sequence: Forward (F) and Reverse (R)	Product size (bps)	Purpose of maker
Nanog	F: GAGGAAGCATCGAATTCTGG R: TGCAGAGCATCTCAGTAGCAG	100	Self renewal
Nestin	F: AGGCGCTGGAACAGAGATT R: TTCCAGGATCTGAGCGATCT	131	Differentiation to neural cells
Sox17	F: CTTTATGGTGTGGGCCAAAG R: GCTTCTCTGCCAAGGTCAAC	122	Differentiation to endoderm

medium supplemented with 10% FBS, 10% KSR (Gibco), 1% non-essential amino acids (NEAA), 4 mM L-glutamine, 100 U/mL penicillin, 100 μg/mL streptomycin, and 0.1 mM β-mercaptoethanol. The cells were maintained in a humidified cell culture incubator at 37 ºC under 5% CO_2. After 12 h of incubation, the wells were replenished with fresh medium and treated with various concentrations of PEI-LGO:Cr (0−37.5 μg/mL) for 72 h. The cells were then collected and subjected to RNA isolation (RNeasy min kit, QIAGEN), cDNA synthesis (iScript cDNA synthesis kit, BioRad), and qRT-PCR amplification (iQ SYBR Green Supermix, BioRad) using three specific primers, *i.e.*, Nanog, Nestin and Sox17, to identify different mRNAs.

Normalized qPCR-run CT values (iCycler, BioRad) were analyzed to yield relative mRNA abundance compared to that of the untreated samples.

Results and Discussion. Both cell lines, including 4T1 and RAW264.7 cells, were exposed to PEI-LGO:Cr nanoparticles at 0, 12.5, 25, 50, 100 µg/mL for 24 h; ESCs were exposed to PEI-LGO:Cr nanoparticles at 0, 25, 50, 75, 100 µg/mL for 72 h. 4T1 cells' viability (expressed as

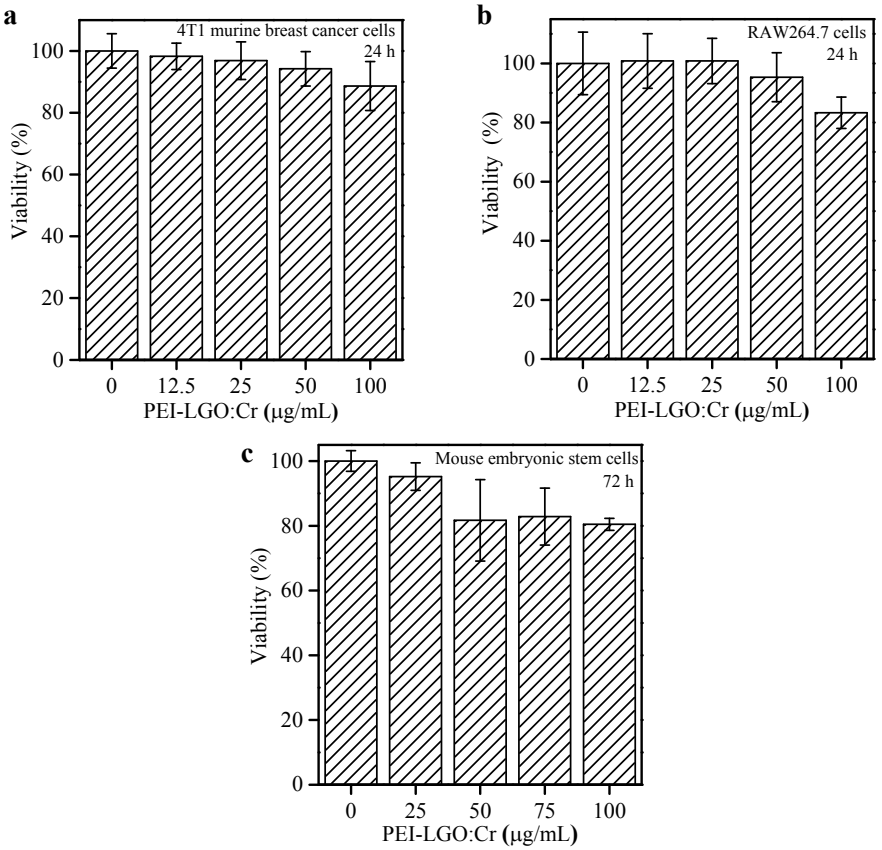

Figure 4.1 Viability assay with PEI-LGO:Cr nanoparticles. **a**, 4T1 murine breast cancer cells. **b**, RAW264.7 murine macrophage cells. **c**, murine ESCs.

mean (%) ± standard deviation (SD)) measured by cell counting under the optical microscope was 100 ± 5.6%, 98.3 ± 4.3%, 96.9 ± 6.1%, 94.2 ± 5.6%, 88.6 ± 7.9%, respectively. (Figure 4.1a) RAW264.7 cells' viability was 100 ± 10.6%, 100.8 ± 9.2%, 100.8 ± 7.7%, 95.3 ± 8.3%, 83.3 ±

5.3%, respectively (Figure 4.1b). ESCs' viability measured by colorimetric assays was 100 ± 3.2%, 95.2 ± 4.2%, 81.7 ± 12.6%, 82.8 ± 8.8%, 80.4 ± 1.9%, respectively (Figure 4.1c). Both 4T1 and RAW264.7 cells exhibited >94% viability in the investigated concentration range (0–50 μg/mL) for 24 h exposure to PEI-LGO:Cr nanoparticles. Due to long term exposure (72 h) of ESCs to PEI-LGO:Cr nanoparticles, ESCs cells only showed 80.4% viability at 100 μg/mL. Although three cell lines shows the viability decreased as a function of nanoparticle concentration, they all showed >80% viability in the tested concentration range up to 100 μg/mL (equal to 200 μM).

Chen *et al.* reported only 600 nM cytotoxic concentrations for 72 h exposure of CdTe QDs on HEK293 cells.[189] Other short term cytotoxicity tests of QDs were summarized in two reviews.[190,191] Due to deterioration of the QD lattices in cells, the liberation of free Cd^{2+} ions can cause significantly cytotoxicity, especially in long term tests.[192] For the cytotoxicity of upconversion nanoparticles, bone marrow-derived stem cells' viability was 65.3% for 24 h exposure with 100 μg/mL PEI-$NaYF_4$:Yb^{3+},Er^{3+} nanoparticles.[193] In sharp contrast to QDs, ESCs show no obvious cytotoxicity after exposure to 100 μg/mL (equal to 200 μM) PEI-LGO:Cr nanoparticles for 72 h in this study. The demonstrated cells have a high tolerance to LGO:Cr nanoparticles.

For ESCs, we also studied the impact of the LGO:Cr nanoparticle labeling on cell renewal and differentiation by analyzing three key biomarkers: Nanog, Nestin and Sox17.[194] Nanog, Nestin and Sox17 were used as a pluripotency marker (self-renewal), a neuroectoderm marker (differentiation to neural cells) and an endoderm marker (differentiation to endoderm), respectively. RNA transcripts for three evaluated genes were all detected in the ESCs exposed to 0–37.5 μg/mL PEI-LGO:Cr nanoparticles for 72 h. The relative abundance of the analyzed

transcripts, as shown in Figure 4.2, was normalized to 0 μg/mL PEI-LGO:Cr nanoparticles exposure. The relative abundance values were expressed in arbitrary units, as mean ± SD for 12.5 μg/mL, 25.0 μg/mL, and 37.5 μg/mL being, respectively, 1.35 ± 0.19, 1.12 ± 0.25, and 1.12 ± 0.25 for Nanog, 1.35 ± 0.20, 1.13 ± 0.20, and 0.94 ± 0.14 for Nestin, and 0.75 ± 0.44, 0.60 ± 0.20, and 0.49 ± 0.21 for Sox17. Expression of Nanog and Nestin did not evidence any statistical difference on the quantitative level. This high level of expression of Nanog and Nestin in ESCs demonstrated that PEI-LGO:Cr nanoparticles had no significant impact on self-renewal and differentiation to neural cells. The relative abundance value of Sox17 decreased while increasing the PEI-LGO:Cr nanoparticle concentration. However, the minor fluctuations at the expression level of Sox17 suggested that ESCs could tolerate the PEI-LGO:Cr nanoparticles up to 37.5 μg/mL. In summary, PEI-LGO:Cr nanoparticles have low impact on cell pluripotency and differentiation, which is in agreement with the low cytotoxicity of PEI-LGO:Cr nanoparticles in cell viability assay.

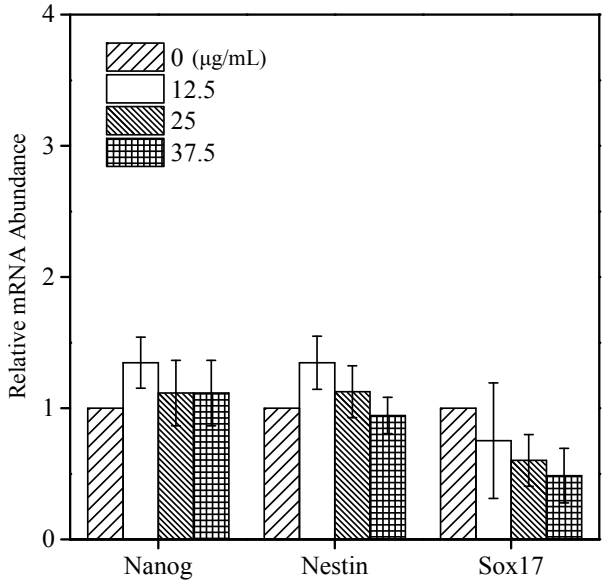

Figure 4.2 Impact of PEI-LGO:Cr nanoparticles on renewal and differentiation of mouse ESCs.

Such good biocompatibility is not unexpected given that all the three constituting metal elements – lithium, gallium and trivalent chromium – are known to have relatively low toxicity profiles. Lithium is regarded as essential nutrients for the human body,[195] a trace amount of trivalent chromium in diet has no adverse effect to human health[196] and gallium-based probes, for instance gallium-67 citrate, were once widely used for cancer diagnosis and staging in the clinic.[197]

4.3 Quantification of $LiGa_5O_8:Cr^{3+}$ nanoparticles in RAW264.7 cells and 4T1 cells

To determine the amount of nanoparticles in cells, ICP-MS method and persistent luminescence measurement were used.

Experiments. For ICP-MS measurement, the PEI-LGO:Cr nanoparticles labeled RAW264.7 cells were mixed with aqueous nitric acid and then heated to dissolve all nanoparticles. The more detailed sample preparation was described in Section 3.2.2.

For persistent luminescence measurement, PEI-LGO:Cr nanoparticles labeled RAW264.7 cell or 4T1 cell suspension (4.0×10^6 cells/mL) was placed in a 96-well plate under irradiation by a 254 nm UV lamp for 5 min. Each well contained 0.25 mL cell suspension. After stoppage of the UV irradiation, persistent luminescence images were taken on an IVIS imaging system in the bioluminescence mode. The exposure time is 1 min. The persistent luminescence from each well was quantified using Living Image software (Version 4.3.1 SP1) at binning of 4, and smooth of 5×5.

Results and discussion. The amount of gallium element in each RAW264.7 cell was quantified as 11.43 pg by the ICP-MS method. According to the chemical formula of LGO:Cr nanoparticles ($LiGa_5O_8:Cr^{3+}$), the total amount of LGO:Cr nanoparticles was estimated as 15.85

pg per RAW264.7 cell. Persistent luminescence measurement shows that the amount of PEI-LGO:Cr nanoparticles internalized in each RAW264.7 cell was about 2.3 times of that in 4T1 cell, as shown in Table 4.2.

Table 4.2 Quantification of persistent luminescence intensities of PEI-LGO:Cr labeled RAW264.7 cells and 4T1 cells.

Cells	RAW264.7	4T1
Total Flux ($\times 10^4$)	8.21	3.57
Normalized	2.3	1

4.4 Thin-section TEM imaging of $LiGa_5O_8:Cr^{3+}$ labeled 4T1 cells

The most common method for studying the biodistribution of nanoparticles in cells is transmission electron microscopy (TEM) imaging.[188,198] TEM imaging requires extensive and careful sample preparation in the entire process, including sample fixing, dehydrating, staining, resin embedding, and ultra-microtome sectioning. TEM can provide excellent spatial resolution (~1 nm), which is required to distinguish nanoparticles from cell structures.[198]

Experiments. 4T1 cells (1.0×10^6 cells/mL) were exposed to sterilized PEI-LGO:Cr nanoparticles (100 μg/mL) and co-incubated in cell culture flask for 2 days using RPMI-1640 medium containing 10% fetal bovine serum. The cells were then collected by treatment with trypsin. For successive culturing, the cells from the first generation were further cultured in medium without the presence of additional PEI-LGO:Cr nanoparticles, till the third generation. These three generations of cells and blank cells (without co-incubated with PEI-LGO:Cr nanoparticles) were then subjected to thin-section TEM imaging. Cells were fixed with Karnovsky's EM fixative (2.5% glutaraldehyde and 2% paraformaldehyde in 80 mM phosphate buffer, pH 7.3–7.4) for 12 h at 4 °C. Secondary fixation was conducted in 1% osmium tetroxide with 1.5% potassium ferrocyanide in double distilled H_2O for 1 h at 4 °C. Dehydration was

carried out in ethanol. Pure Epon-Araldite resin was added and infiltrated overnight at room temperature. All resin was removed the next day, and fresh resin was added to the appropriate depth. The sample was polymerized for 18 h. Ultrathin sections of cells were obtained by cutting *en face* (parallel to the surface on which the cells were grown) using a ultramicrotome, and then stained with uranyl acetate and lead citrate before viewing in the TEM.

Results and discussion. Figure 4.3 shows the thin-section TEM images of three generations of 4T1 cell labeled with PEI-LGO:Cr nanoparticles as well as a control cell (cells not incubated with PEI-LGO:Cr nanoparticles). In the control cell (Figure 4.3a), a variety of organelles was found, including the plasma membrane, the nucleus, the mitochondria and lysosome. In contrast to the control cell, many nanoparticles were found in the cell's endosomes/lysosomes (Figure 4.3b–d) for the 4T1 cells incubated with PEI-LGO:Cr nanoparticles.[198,199] The accumulation of LGO:Cr nanoparticles in the cell endosomes/lysosomes, suggests that the particle uptake was mainly mediated by endocytosis. These nanoparticles remained stable in the endosomes/lysosomes, and were able to be carried over to the daughter cells up to the third generations. The acidic lysosomal environment has no detectable impact on the particles' morphology and, as the long-term *in vitro* and *in vivo* tracking results shown in Section 4.6 and Section 5.3, respectively, the particles' NIR performance. In fact, the LGO:Cr nanoparticles were found to be stable over a broad range of pH from 3.0 to 11.0, as shown in Figure 3.7. For the first generation of 4T1 cells labeled with PEI-LGO:Cr nanoparticles, we observed that pseudopods extended from the cell surface, creating a phagocytic cup beneath the PEI-LGO:Cr nanoparticle (Figure 4.4). These pseudopods could extend further, wrapping around the particle and pulling it into the cell.[175,200] Besides, TEM images also show that the PEI-LGO-Cr nanoparticles tended to

aggregate to from nanoparticles clusters, a phenomenon that was observed by Zhou *et al*. with iron oxide nanoparticles,[201] and by Ahlinder *et al*. with titania and goethite nanoparticles.[188]

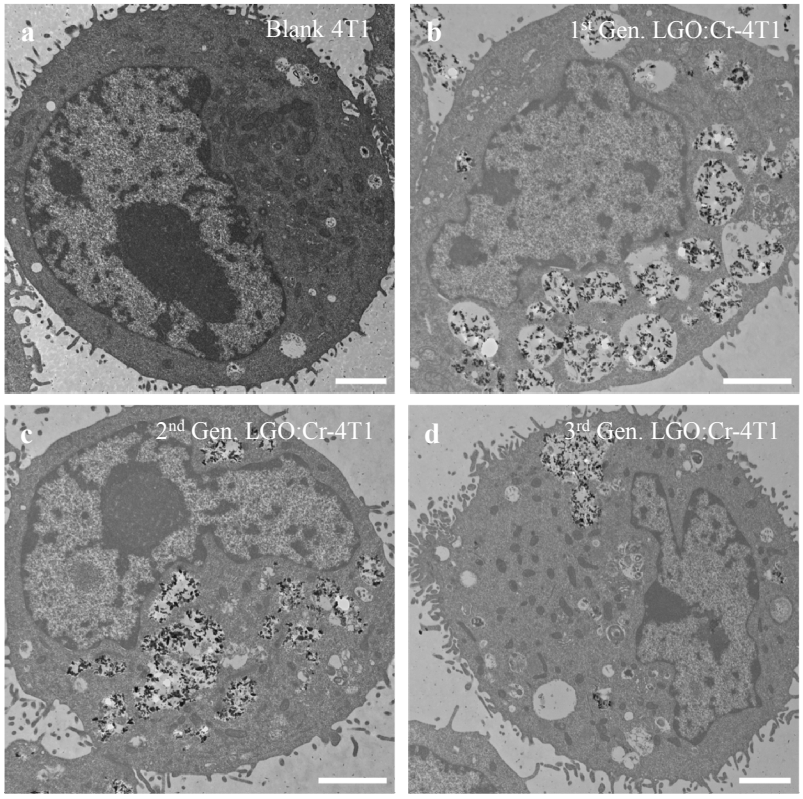

Figure 4.3 TEM images of PEI-LGO:Cr labeled 4T1 cells from different passages. Blank 4T1 cells (without PEI-LGO:Cr co-incubation) and three generations 4T1 cells co-incubated with PEI-LGO:Cr nanoparticles were fixed for thin section TEM. Scale bars, 2 μm.

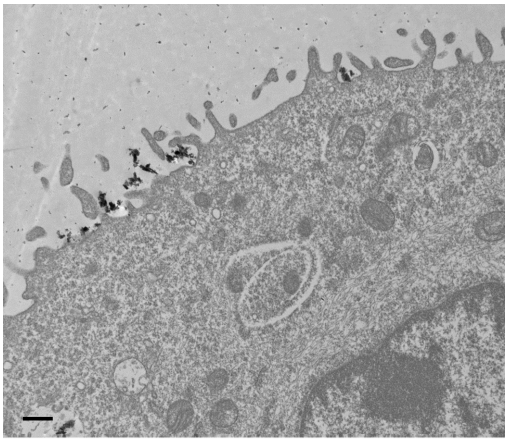

Figure 4.4 TEM image of first generation 4T1 cells labeled with LGO:Cr nanoparticles. Scale bar, 500 nm.

4.5 *In vitro* luminescence microscopic studies of PEI-LGO:Cr labeled cells

The thin-section TEM images in Section 4.4 provides direct evidence about the distribution of LGO:Cr nanoparticles in the cells. Another powerful technique commonly used to study the bio-distribution of nanoparticles in cells is bioluminescence microscopy.

Experiments. PEI-LGO:Cr labeled cells were fixed in ethanol solution and irradiated by a 254 nm UV lamp for 5 min. The persistent luminescence from the PEI-LGO:Cr labeled cells was imaged using an Olympus LV200 bioluminescence microscope. A Cy5.5 emission filter (HQ725/50M) was used for collecting the NIR persistent luminescence signals.

We also used living firefly luciferase-expressing 4T1 (f-luc-4T1) cells labeled with PEI-LGO:Cr nanoparticles for bioluminescence imaging. The PEI-LGO:Cr-labeled f-luc-4T1 cells were incubated with D-luciferin (150 μg/mL) for 10 min before the imaging. The emission filter was set as "open" during collecting bioluminescence signals from the f-luc. The cells were then irradiated by a 254 nm UV lamp for 5 min and the Cy5.5 emission filter was used when collecting the NIR persistent luminescence signals. All images were processed using CellSens Dimension software (Version 1.71, Olympus Corporation, Tokyo).

Results and Discussion. After charged by a 254 nm UV lamp, almost all the cells were clearly visualized (Figure 4.5) owing to the strong NIR persistent luminescence from the LGO:Cr nanoparticles and the complete elimination of the background noise in the imaging system. The NIR signals lasted for at least 30 min before diminished below the detection threshold. To our best knowledge, this is the first visualization and imaging of individual cells based on persistent luminescence signals.

Owing to the narrow emission band in the NIR, the LGO:Cr nanoparticles can work along with visible bioluminescence probes, like firefly luciferase (f-luc), for multiplexed imaging. To

differentiate the LGO:Cr nanoparticles' NIR persistent luminescence (~650–850 nm peaking at 716 nm) from the f-luc's bioluminescence (~460–670 nm peaking at 557 nm)[202], a Cy5.5 filter was used when collecting the NIR signals (only 698–752 nm light can pass the filter). Indeed, luminescence from both sources was clearly visualized, as the images shown in Figure 4.6. While overlaps were observed across the scope, discrepancies were also found in many cells, suggesting good discrimination of the two signals (Figure 4.6b,c). Notably, the intensity of the NIR persistent luminescence from LGO:Cr nanoparticles is comparable to that of the bioluminescence from f-luc; the latter is by far the most sensitive optical method for cell tracking.[202,203]

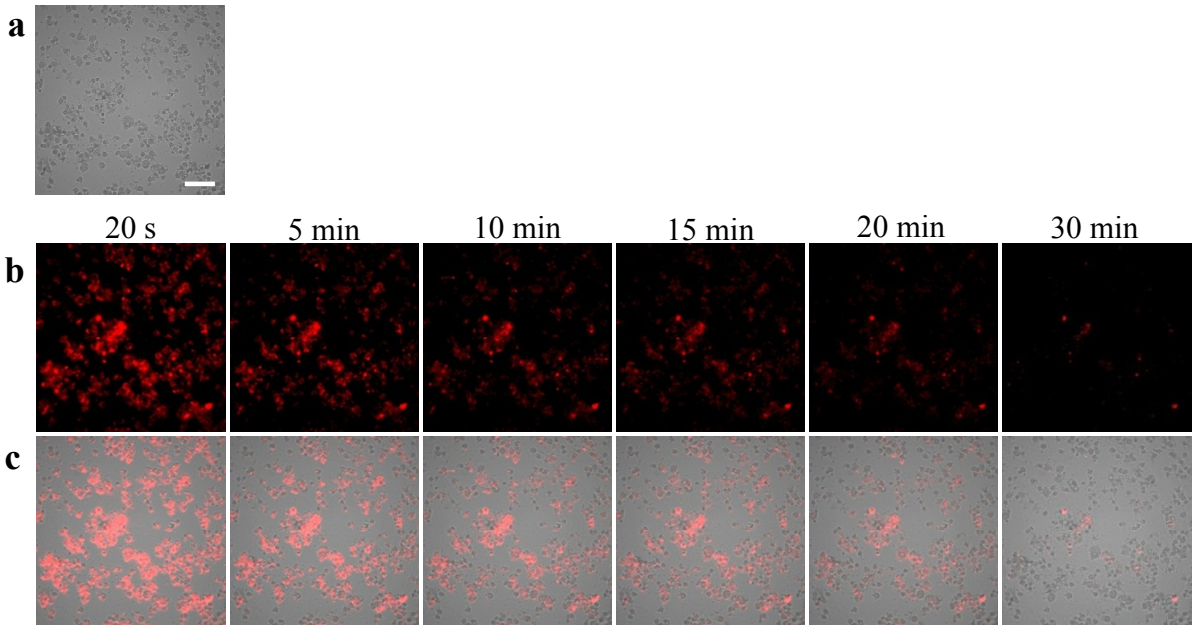

Figure 4.5 NIR persistent luminescence microscopic images of fixed 4T1 cells labeled with PEI-LGO:Cr nanoparticles. **a**, Bright-field optical image of PEI-LGO:Cr labeled 4T1 cells. (Scale bar, 100 μm). Row **b**, NIR persistent luminescence images of UV pre-irradiated PEI-LGO:Cr labeled cells. Row **c**, Merged images by overlapping **a** with the images in Row **b**.

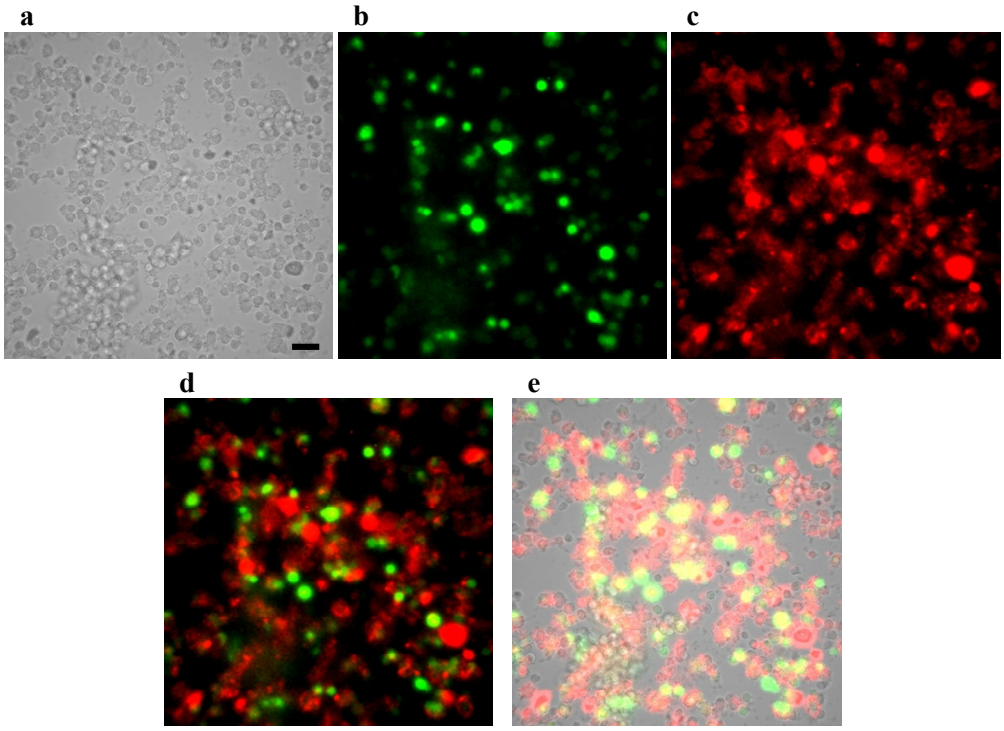

Figure 4.6 Luminescence microscopic studies of living f-luc-4T1 cells labeled with PEI-LGO:Cr nanoparticles. **a**, Bright-field image. (Scale bar, 100 μm) **b**, Bioluminescence image of PEI-LGO:Cr labeled 4T1-f-luc cells. **c**, NIR persistent luminescence image of UV pre-irradiated PEI-LGO:Cr labeled 4T1-f-luc cells. **d**, Merged image of **b** and **c**. **e**, Merged image of **a**, **d**.

4.6 *In vitro* NIR photostimulated persistent luminescence studies of PEI-LGO:Cr labeled cells

The bioluminescence microscopic study in Section 4.5 shows that the NIR persistent luminescence from PEI-LGO:Cr nanoparticles labeled 4T1 cells can be observed for up to 30 min. To increase the observation time of PEI-LGO:Cr nanoparticles, NIR emission *via* PSPL process is studied in this section.

Experiments. PEI-LGO:Cr labeled and unlabeled 4T1 cells ($2x10^6$ cells in 1.5 mL ethanol aqueous solution) were placed in a 24-well plate. Both the labeled and unlabeled 4T1 cells were irradiated by a 254 nm UV lamp for 15 min. NIR persistent luminescence image of the PEI-LGO:Cr labeled 4T1 cells was taken at 10 s after the removal of the UV irradiation using an

IVIS Lumina II imaging system in the bioluminescence mode. At every 24 h, the two types of cells were imaged by the IVIS system, followed by stimulation with a white LED flashlight (Olight SR51, 900 Lumens) for 15 s with the flashlight being placed at 6 cm above the 24-well plate. The NIR PSPL images were then taken at 10 s after the stoppage of the stimulation. The imaging process lasted for 192 h. The images were processed using the Living Image software (Version 4.3.1 SP1) at binning of 4 and smooth of 5×5.

Results and discussion. The NIR persistent luminescence of the PEI-LGO:Cr labeled 4T1 cells lasted for 90 min, as shown in Figure 4.7. The decay of the persistent luminescence was

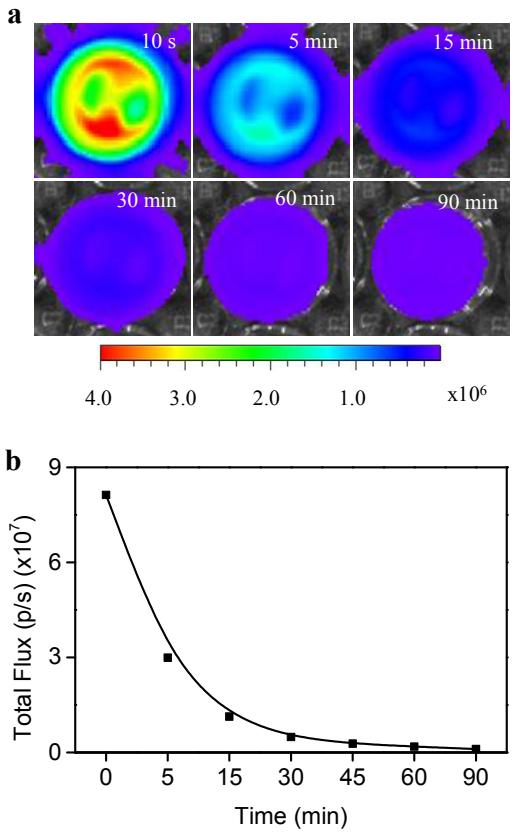

Figure 4.7 Cell phantom studies of UV pre-irradiated PEI-LGO:Cr labeled 4T1 cells. **a**, NIR persistent luminescence images. **b**, Quantification of total flux of the NIR persistent luminescence signals at different instant in **a**. The color scale bar represents the luminescence intensity in the unit of radiance, p/sec/cm^2/sr.

clearly presented in pseudocolor images (Figure 4.7a) derived from mapping luminescence intensity to a color. The total intensity of persistent luminescence was quantified as 8.13×10^7 p/s, 2.99×10^7 p/s, 1.13×10^7 p/s, 4.89×10^6 p/s, 2.80×10^6 p/s, 1.87×10^6 p/s and 1.089×10^6 p/s at 10 s, 5 min, 15 min, 30 min, 45 min, 60 min and 90 min, respectively, after the removal of UV irradiation (Figure 4.7b). The 2×10^6 PEI-LGO:Cr labeled 4T1 cells imaged by the IVIS system only exhibit 90 min NIR persistent luminescence, due to the very low amount of LGO:Cr nanoparticles (~13 μg) in cells.

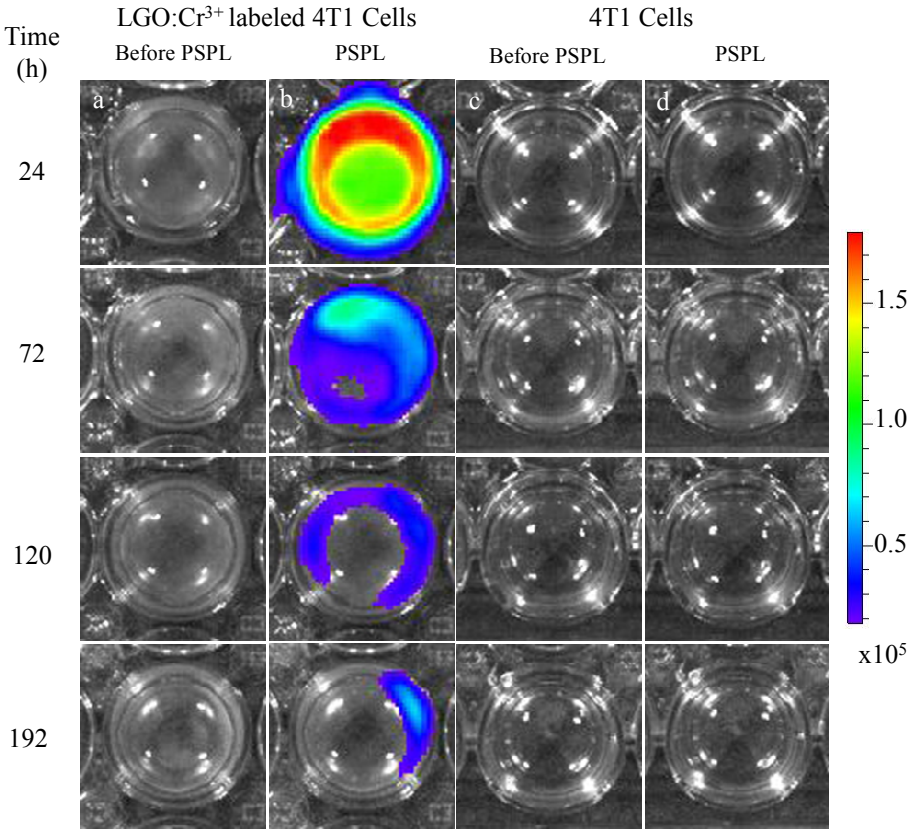

Figure 4.8 NIR PSPL images of 4T1 cells labeled and un-labeled with PEI-LGO:Cr nanoparticles for 192 h monitoring. **a**,**b**, 4T1 cells labeled with PEI-LGO:Cr nanoparticles in a 24-well plate. **c**,**d**, Unlabeled 4T1 cells in a 24-well plate. Both the labeled and unlabeled 4T1 cells were pre-irradiated by UV irradiation. The PSPL images were taken by stimulation with a white LED flashlight for 15 s. The images were taken on an IVIS Lumina II imaging system in the bioluminescence mode. The exposure time is 2 min. The color scale bar represents the luminescence intensity in the unit of radiance, p/sec/cm^2/sr.

At 24 h after the removal of the UV irradiation, no NIR persistent luminescence from the PEI-LGO:Cr labeled 4T1 cells as well as the 4T1 control cells (without PEI-LGO:Cr labeling) was detected by the IVIS imaging system, as shown in Figure 4.8. After stimulation with white light, only PEI-LGO:Cr labeled 4T1 cells emitted intense PSPL signals. The monitoring experiments on the PSPL signals showed that the PEI-LGO:Cr labeled 4T1 cells exhibit enhanced NIR PSPL emission after each stimulation, and the PSPL signal can still be clearly detected after 8 times of white LED stimulations and a total of 192 h decay (Figure 4.8). The total intensity of the PSPL signals was quantified as 4.05×10^6 p/s, 1.13×10^6 p/s, 5.26×10^5 p/s, 4.54×10^5 p/s and 3.90×10^5 p/s at 24 h, 72 h, 120 h, 168 h and 192 h, respectively (Figure 4.9). Such repeated NIR PSPL signals permit a very-long tracking window for bioimaging.

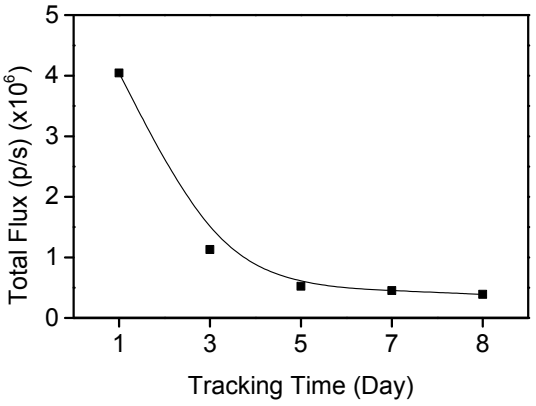

Figure 4.9 Quantification of total flux of the NIR PSPL signals in Figure 4.8.

4.7 Summary

Cytotoxicity studies show that the PEI-LGO:Cr nanoparticles are less toxic to a variety of cell lines including 4T1 cells, RAW264.7 cells and ESCs. More than 80% of the tested cells were survived after 24 h (4T1 cells and RAW264.7 cells) or 72 h (ESCs) of incubation with up to 100 μg/mL PEI-LGO:Cr nanoparticles. The PEI-LGO:Cr nanoparticles also have low impact to cell renewal and differentiation, which were verified by three key biomarkers: Nanog, Nestin and Sox17. The cytotoxicity evaluation clearly show that the PEI-LGO:Cr nanoparticles are fairly biocompatible and can be used as optical probes for *in vivo* bioimaging study.

Thin sectional TEM studies on the PEI-LGO:Cr nanoparticles labeled 4T1 cells show that the PEI-LGO:Cr nanoparticles can be efficiently internalized by the cells and the internalized nanoparticles can be transferred to daughter cells up to three generation in a 6 days of incubation. The amount of PEI-LGO:Cr nanoparticles internalized in each cell is about 15.85 pg (pico-gram), as determined by ICP-MS analyss. After UV irradiation, the PEI-LGO:Cr nanoparticles labeled 4T1 cells emit detectable NIR persistent luminescence, which can be readily detected by an Olympus LV200 bioluminescence microscope for up to 30 min. This is the first visualization and imaging of individual cells based on persistent luminescence signals. Moreover, the intensity of the NIR persistent luminescence from the LGO:Cr nanoparticles is comparable to that of the bioluminescence from f-luc, the most sensitive optical imaging probe for cell tracking. Finally, by using the unique PSPL phenomenon, we have extended the *in vitro* tracking window for the PEI-LGO:Cr nanoparticles labeled cells to up to 8 days (192 h).

CHAPTER 5

IN VIVO BIOIMAGING AND TUMOR TARGETING USING CHROMIUM-DOPED LITHIUM GALLIUM OXIDE NANOPARTICLES AS THE OPTICAL NANOPROBES

5.1 Introduction

In Chapter 4, we have shown that the LGO:Cr nanoparticles can function as both a self-sustained NIR persistent material exhibiting an intense, super-long NIR persistent luminescence and a new type of photostimulable material exhibiting repeatedly photostimulated NIR persistent luminescence in *in vitro* cell experiments. Moreover, the ability to render LGO:Cr biocompatible and non-toxic extends their applicability to *in vivo* targeting imaging and tracking. The key concern regarding the *in vivo* applications of nanoparticles is to understand their pharmacokinetics and biodistribution. Chemical and physical properties of the nanoparticles, including size and surface chemistry, are important factors that determine their pharmacokinetics and biodistribution.[204] LGO:Cr nanoparticles as optical nanoprobes are subject to intravenous administration, and reach the targeting sites through blood circulation. Therefore, the *in vivo* behavior of the nanoparticles is further controlled by the size and surface condition of the nanoparticles.

For *in vivo* applications, nanoparticles injected into the animals or human bodies are captured by a reticulo-endothelial system (RES) or are filtered by kidney and excreted in urine.[205-208] Nanoparticles with hydrodynamic diameters larger than 10 nm in bloodstream can be recognized as invaders by opsonin proteins (in blood serum), seized by macrophages (*e.g.* Kupffer cells). Due to the easier accessibility, most of the nanoparticles are uptaken by the macrophages in the

liver and spleen. Between these two organs, there is a tendency that nanoparticles with the size of larger than 200 nm prefer to be taken up by the spleen.[205] And then nanoparticles are eventually eradicated through the RES system.[209-212] Although opsonin proteins cannot recognize the sub-10 nm nanoparticles, sub-10 nm nanoparticles are easily cleared through urinary excretion.[74,210,213] Therefore, developing nanoparticles with the size between 10 nm and 200 nm and without being recognized by the opsonin proteins is necessary for intravenous injections.

5.1.1 *In vivo* targeting

Passive and active tumor targeting models are currently used to explain delivery of nanoparticles to the tumor sites.[214,215] In the passive targeting mode, nanoparticles preferentially accumulate at tumor sites through an enhanced permeability and retention (EPR) effect.[216-219] Tumors secret high concentration of vascular permeability factors (*e.g.*, bradykinin, nitric oxide, peroxynitrite, prostaglandins, vascular endothelial growth factor, matrix metalloproteinases, kallikrein, and tumor necrosis factor) to accelerate the formation of new blood vessels (neovascularization or angiogenesis) which supply oxygen and nutrients for tumor growth. This results in leaky vasculature in most tumors. This tumor vasculature is hyperpermeable and allows nanoparticles to access tumor tissue.[220-222] Moreover, tumors lack an effective lymphatic drainage system, which leads to nanoparticle accumulation.[217,223]

In the active targeting mode, the nanoparticles are conjugated with tumor-binding ligands. These ligands as a targeting moiety help nanoparticles to recognize and enter into tumor cells *via* endocytosis (discussed in Chapter 4.1). For example, a prostate-specific membrane antigen (PSMA) has been identified as a cell surface marker for both prostate epithelial cells and neovascular endothelial cells. Consequently, PSMA has been chosen as an attractive target for

both imaging and therapeutic intervention of prostate cancer.[224] Nanoparticles conjugated to PSMA monoclonal antibodies, which recognize the extracellular domain of PSMA, can be used as targeting probes for imaging of prostate cancer.[217]

5.1.2 *In vivo* cell tracking

In recent years, cell-based therapies have been emerging as a potential strategy to treat different kinds of diseases, involving cancer, cardiac infarction, neurodegenerative diseases, inflammation, immunological disorders, and stroke.[225] This requires the administered cells (*e.g.*, stem cells, immune cells and cancer cells) migrate expeditiously to the intended target in sufficient numbers to provoke responses.[225,226] Therefore, the ability to non-invasively track the cells to their target sites would allow better understanding of the mechanisms of disease development and intervention.[227-231]

In preclinical *in vivo* studies of cell tracking, different fluorescent probes, including NIR organic dyes (IRDye800CW[232] and Vivotag680[233]), fluorescent proteins,[204] luciferase[204,234] and QDs,[235] have been used to labeled cells to study cancer immunotherapy and inflammatory diseases. In addition to optical imaging, cell tracking also succeeded in MRI with magnetic nanoparticles labeled cells. However, only radionuclide scintigraphy, mainly using γ camera or SPECT, has been clinically established for cell tracking so far,[226] owing to the long penetration depth and high sensitivity.

To improve the detectable signals in *in vivo* optical nanoparticles-based cell tracking, loading adequate amount of nanoparticles into cells and tuning optical properties of nanoparticles into the biological transparency window are necessary. For loading nanoparticles into cells, a variety of transfection agents (such as PLL and PEI) were effectively employed to enhance the uptake

through the electrostatic interaction.[180-183] The tuned optical performance of LGO:Cr nanoparticles for *in vivo* applications were studied in the following sections. Later, LGO:Cr nanoparticles were applied in in vivo imaging with mice models.

5.2 Detection sensitivity and depth of $LiGa_5O_8:Cr^{3+}$ based bioimaging

The detection sensitivity of LGO:Cr nanoparticles was evaluated in a mouse model and was compared with two commonly used optical probes, *i.e.*, QDs and firefly luciferase. All the animal studies were performed according to a protocol approved by the Institutional Animal Care and Use Committee of the University of Georgia. The detection depth was studied in a pork model.

5.2.1 Detection sensitivity of LGO:Cr based cell labeling

Experiments. To evaluate the detection sensitivity, elevated numbers (~5, 50, 100, 500, and 1,000) of PEI-LGO:Cr labeled RAW264.7 cells and PEI-LGO:Cr labeled 4T1 cells were subcutaneously injected onto the back of a nude mouse. The cells were fixed and irradiated by a 254 nm UV lamp for 5 min before the injection. The images were taken on an IVIS imaging system in the bioluminescence mode. The exposure time is 5 min. The NIR persistent luminescence of PEI-LGO:Cr labeled RAW264.7 cells was quantified by Living Image Software (Version 4.3.1 SP1) at the ROI of 38%, binning of 4, and smooth of 5×5.

Results and discussion. The detection sensitivity of PEI-LGO:Cr labeled RAW264.7 cells is exceptional. As few as ~5 cells can be clearly visualized, as shown in Figure 5.1a. This sensitivity is comparable to f-luc-based cell tracking,[203] but several orders of magnitude higher than that of QDs[46] and organic dyes.[236]

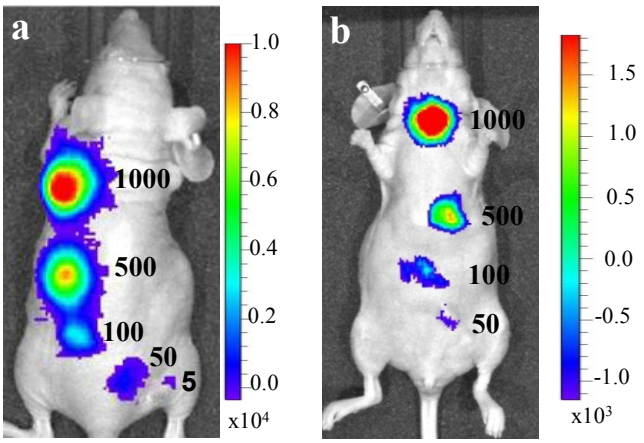

Figure 5.1 Detection sensitivity of PEI-LGO:Cr-based cell labeling. **a**, Elevated numbers (~5, 50, 100, 500, and 1,000) of PEI-LGO:Cr labeled RAW264.7 cells. **b**, Elevated numbers (50, 100, 500, and 1,000) of PEI-LGO:Cr labeled 4T1 cells. These pre-irradiated PEI-LGO:Cr-based cells were subcutaneously injected onto the back of the nude mice.

Quantitative measurements of the persistent luminescence intensity of the PEI-LGO:Cr labeled RAW264.7 cells revealed an excellent linear relationship between the total luminescence flux and the number of cells measured (Figure 5.2). The detection sensitivity of the PEI-LGO:Cr

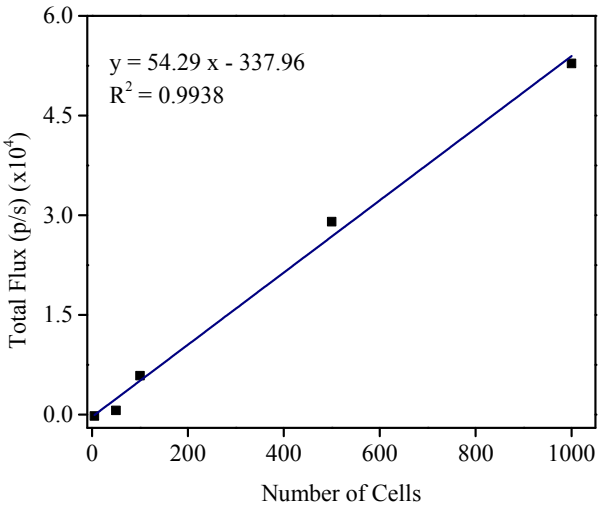

Figure 5.2 Quantification of subcutaneously injected PEI-LGO:Cr labeled RAW264.7 cells in a mouse model. The NIR persistent luminescence signals were acquired using an IVIS imaging system.

labeled 4T1 cells is about 50 cells, as shown in Figure 5.1b. The lower detection sensitivity of the PEI-LGO:Cr labeled 4T1 cells compared with the RAW264.7 cells is because more PEI-LGO:Cr nanoparticles were internalized in RAW264.7 cells than in 4T1 cells. The RAW264.7 cells are expected to contain more PEI-LGO:Cr nanoparticles than 4T1 cells, because RAW264.7 cells (mouse macrophage) are programmed to engulf and digest any foreign nanoparticles through the process of phagocytosis.[169,170]

5.2.2 Comparison of the luminescence between QDs and LGO:Cr nanoparticles

Experiments. To evaluate the luminescence performance between QDs and LGO:Cr nanoparticles, 32 μg QDs (emission at 705 nm) and PEI-LGO:Cr nanoparticles were subcutaneously injected into the back of nude mice. The imaging experiment was carried out on an IVIS Lumina II imaging system in fluorescence mode for QDs and in bioluminescence mode for PEI-LGO:Cr nanoparticles. In both modes, a Cy5.5 filter was used. The QDs were excited by 570 nm light while imaging. The exposure time for QDs-based imaging is 1 s. The PEI-LGO:Cr nanoparticles were irradiated by a 254 nm UV lamp for 15 min before injection. The exposure time for PEI-LGO:Cr nanoparticles-based imaging is 2 min. The S/N ratio was determined by quantifying the luminescence intensity.

Results and discussion. As shown in Figure 5.3a, the total number of photons generated in the LGO:Cr-based bioluminescence imaging is generally weak, about 3–5 orders of magnitude lower than that generated by the same amount (32 μg) of QDs (Figure 5.3c). But due to the elimination of the external excitation and along with it, the autofluorescence, the background noise for the LGO:Cr-based imaging is at the minimum, producing an S/N ratio of 1740, which is about one order of magnitude higher than the QDs-based imaging (Figure 5.3e). The benefit of

the absence of autofluorescence becomes overwhelmingly significant when the mouse was viewed in the supine position (*i.e.*, face up): the NIR persistent luminescence signals from the LGO:Cr nanoparticles can be sharply visualized (Figure 5.3b), but the fluorescence signals from QDs is submerged by the overwhelming autofluorescence signals from the skin and the intestine (Figure 5.3d). The ventral view image in Figure 5.3b also revealed the exceptionally deep tissue

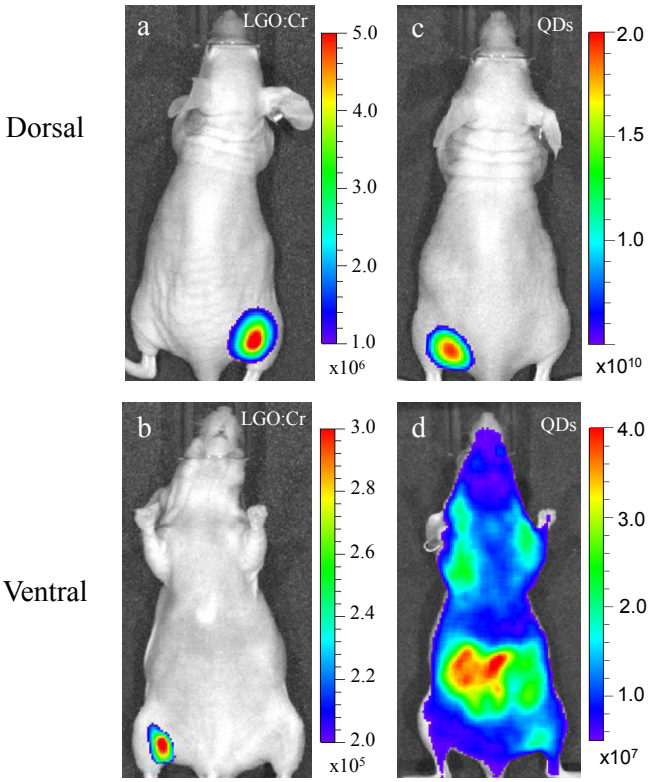

e

	Peak Signal (photons per secons)	Average Noise (photons per secons)	S/N ratio
QD	1.938×10^{10}	2.564×10^{8}	755
LGO:Cr	5.799×10^{6}	-3.334×10^{3}	1740

Figure 5.3 Comparison of the luminescence intensity between QDs and LGO:Cr nanoparticles. **a**,**b**, Dorsal and ventral views, respectively, of a nude mouse subcutaneously implanted with 32 μg UV pre-irradiated PEI-LGO:Cr nanoparticles. **c**,**d**, Dorsal and ventral views, respectively, of a nude mouse subcutaneously implanted with 32 μg QDs (emission at 705 nm). The QDs were excited by 570 nm light while imaging. **e**, S/N ratios in **b** and **d**.

penetration of the LGO:Cr nanoparticle-based imaging (the thickness of the hind limb of the mouse in Figure 5.3c is about 15 mm), and such an ability of "seeing" through a small animal has seldom been achieved optically. In addition to a clean background, the deep penetration is also credited to the NIR luminescence to which the tissue is relatively more transparent.[29]

5.2.3 Comparison of the luminescence between firefly luciferase and LGO:Cr nanoparticles.

To demonstrate the higher tissue penetrating power of the NIR light over the visible light, we compared the LGO:Cr-based imaging with the firefly-luciferase-based imaging under the same bioluminescence imaging condition.

Experiments. 4T1 cells stably expressing firefly luciferase were labeled with PEI-LGO:Cr nanoparticles. The dually labeled 4T1 cells were divided into two equal parts with each part containing about 1.0×10^6 cells. One part was incubated with D-luciferin (150 μg/ml), and 10 min later was subcutaneously injected onto the back of the left hind limb of a nude mouse for imaging. The other part was irradiated by a 254 nm UV lamp for 15 min (without D-luciferin incubation), and then subcutaneously injected onto the back of the right hind limb of a nude mouse for imaging. All the images were acquired on an IVIS Lumina II imaging system in the bioluminescence mode with the emission filter set as "open", and with an exposure time of 2 min. The total flux of luminescence was qualified by Living Image software (Version 4.3.1 SP1) at binning of 4 and smooth of 5×5.

Results and discussion. Firefly luciferases emit green light (~557 nm) in the presence of oxygen, ATP, Mg^{2+} and luciferin at room temperature, but the emission shifts to red light (612 nm) at 37 ˚C in the mouse body.[237] For mice bioimaging in this dissertation, all mice were placed

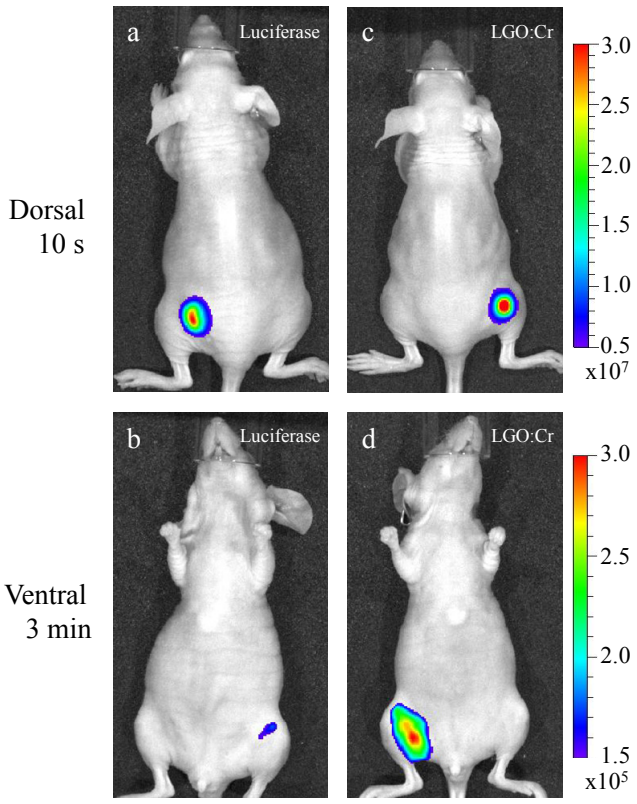

e

	Time	View	Total Flux (p/s)
Luciferase	10 s	Dorsal	9.726×10^7
	3 min	Ventral	1.740×10^5
LGO:Cr	10 s	Dorsal	8.025×10^7
	3 min	Ventral	2.547×10^6

Figure 5.4 Comparison of the luminescence intensity between f-luc and LGO:Cr nanoparticles. **a**,**b**, Dorsal and ventral views, respectively, of a nude mouse subcutaneously implanted with f-luc-4T1 cells labeled LGO:Cr without UV pre-irradiation. **c**,**d**, Dorsal and ventral views, respectively, of a nude mouse subcutaneously implanted with f-luc-4T1 cells labeled LGO:Cr with UV pre-irradiation. **e**, S/N ratios in **b** and **d**.

on a 37 ˚C warm stage to keep mice body temperature stable in the IVIS imaging system. Therefore, the emission of f-luc-4T1 mixed with D-luciferin is 612 nm in the mouse body, instead of the green emission (557 nm) of f-luc-4T1 mixed with D-luciferin at room temperature as discussed in Chapter 4. (Figure 4.6) The signals of f-luc bioluminescence and LGO:Cr

persistent luminescence are comparable when the animals were viewed from the dorsal side (Figure 5.4a,c). In ventral view (Figure 5.4b,d), however, the intensity of the LGO:Cr persistent luminescence is about one order of magnitude higher than that of the f-luc bioluminescence, showing greater penetration of the NIR light than the visible light.

5.2.4 Imaging Depth

The deep penetration capability of the NIR persistent luminescence from LGO:Cr nanoparticles is further demonstrated using pork as a model tissue.

Experiments. LGO:Cr nanoparticles were dispersed in water to form 0.3 mg/mL and 3 mg/mL suspensions. The two suspensions were irradiated with a 254 nm UV lamp for 5 min. 50 μL of the UV-irradiated suspensions, containing about 15 μg and 150 μg LGO:Cr nanoparticles, were injected into two pieces of pork at 2.5 cm and 3.7 cm deep, respectively. NIR persistent luminescence images were taken after the LGO:Cr nanoparticles injection. Then, the two pork, injected with 15 μg and 150 μg LGO:Cr nanoparticles, were illuminated by an Olight SR51 white LED flashlight (900 lumens) for 15 s to elicit NIR PSPL signals, at the 30 min and 60 min time point. NIR PSPL images were taken at 2 min after the LED stimulation. The images were taken on an IVIS Lumina II imaging system in the bioluminescence mode with an exposure time of 2 min.

Results and discussion. The NIR persistent luminescence signals from the LGO:Cr nanoparticles injected into 2.5 cm and 3.7 cm deep of pork can be clearly detected in the IVIS imaging system (Figure 5.5 and Figure 5.6). For the 15 μg UV pre-irradiated LGO:Cr nanoparticles injected into 2.5 cm deep of a pork, the NIR persistent luminescence signals from the LGO:Cr nanoparticles can be clearly detected by the IVIS imaging system for more than 30

min (Figure 5.5a–d). For the 150 µg LGO:Cr nanoparticles injected into 3.7 cm of a pork, the persistent luminescence signals remained detectable for about 60 min, as shown in Figure 5.6a–d.

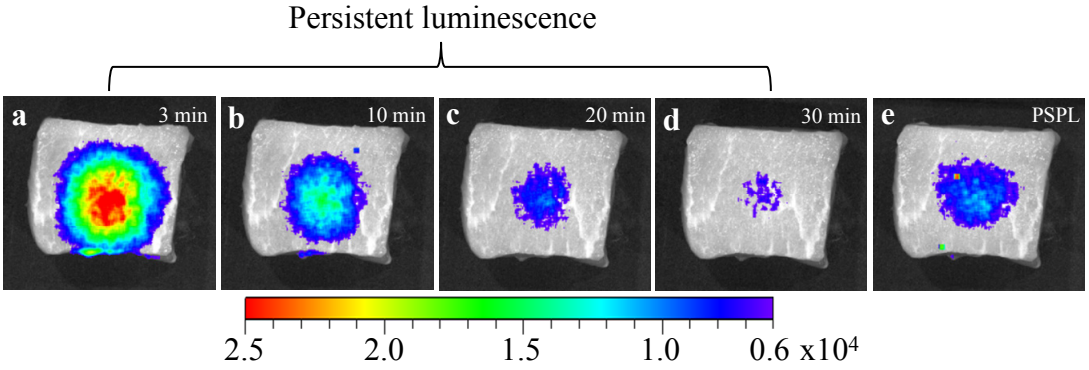

Figure 5.5 NIR persistent luminescence and PSPL signals from 15 µg LGO:Cr nanoparticles injected into 2.5 cm depth inside the pork. **a**–**d**, NIR persistent luminescence images taken at 3–30 min after the injection. **e**, Image of NIR PSPL signals taken at 2 min after the LED stimulation.

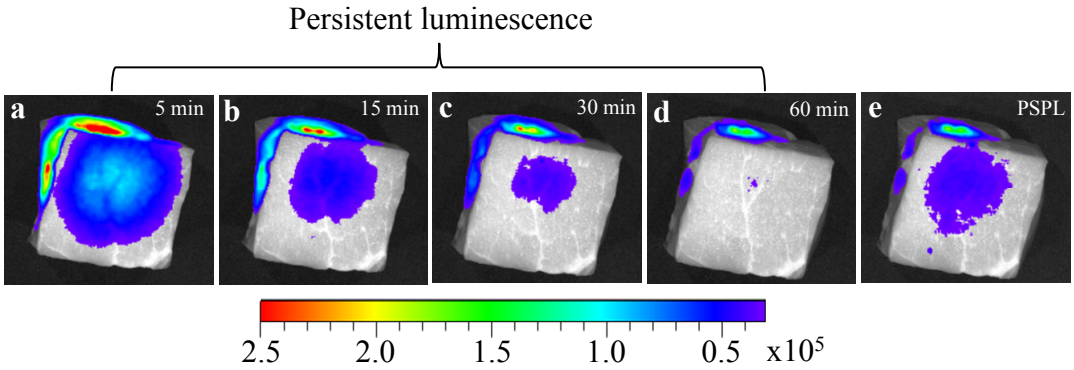

Figure 5.6 NIR persistent luminescence and PSPL signals from 150 µg LGO:Cr nanoparticles injected into 3.7 cm depth inside the pork. **a–d**, NIR persistent luminescence images taken at 5–60 min after the injection. **e**, Image of NIR PSPL signals taken at 2 min after the LED stimulation.

The effectiveness of white LED stimulation in eliciting PSPL signals from UV pre-irradiated LGO:Cr nanoparticles was demonstrated using the present pork model. PSPL signals from 15 µg LGO:Cr nanoparticles located at 2.5 cm deep and from 150 µg LGO:Cr nanoparticles located at 3.7 cm deep can be readily elicited by short-time white light illumination at the 30 min and 60

min time points, as shown in Figure 5.5e and Figure 5.6e, respectively. These penetration depths of > 2.5 cm are significantly greater than that afforded by fluorescence imaging (< 1 cm) and bioluminescence imaging (< 2 cm),[29] as well as NIR-to-NIR upconversion luminescence imaging (< 2 cm).[74,238]

5.3 NIR photostimulated persistent luminescence imaging of PEI-LGO:Cr nanoparticles-labeled 4T1 cells

We have shown the use of NIR PSPL in longitudinal cellular imaging application in Chapter 4. Here we demonstrate the application of this novel PSPL phenomenon in long-duration *in vivo* bioimaging.

Experiments. PEI-LGO:Cr labeled 4T1 cells (~2.5×10^7 cells) were irradiated by a 254 nm UV lamp for 15 min, and then subcutaneously injected into the back of a nude mouse. The decay of NIR persistent luminescence was monitored for 4 h (Figure 5.7a). From the 4 h time point, the mouse was exposed every 30 min to a white LED flashlight (for 15 s) for a total of 15 times to elicit NIR PSPL signals (Figure 5.7b). From the 72 h time point, the mouse was irradiated daily by the LED flashlight (for 15 s), and PSPL images were taken at 10 s and 5 min after each stimulation (Figure 5.7b). All images were acquired with IVIS imaging system in the bioluminescence mode with an exposure time of 2 min.

Results and Discussion. As aforementioned, a major restriction of current persistent luminescence-based imaging is its short observation window (up to 15 h for subcutaneous injection and up to 7.5 h for intravenous injection)[21,70] which needs to be significantly increased in order to meet the demand of longitudinal imaging such as cell tracking which often needs a

window of days or even weeks. This longitudinal tracking demand can be perfectly satisfied by utilizing the unique PSPL phenomenon possessed by the LGO:Cr nanoparticles.

For LGO:Cr nanoparticles-bearing 4T1 cells (~2.5×10^7 cells) subcutaneously implanted into a mouse, the initial NIR persistent luminescence signals remained detectable for more than 4 h (Figure 5.7a). When the dimming animal was illuminated with a white LED flashlight for 15 s, the NIR emission from the LGO:Cr nanoparticles *in vivo* was immediately recovered (Figure 5.7b–e). The resulting PSPL signal was detectable for up to 30 min *in vivo* and repeated 15 times within 1 day (Figure 5.7b). At the 4 h time point, the quantified total fluxes of the NIR signals before and after the LED stimulation are about 7.4×10^5 and 4.9×10^6 photons per second, respectively, as shown in Figure 5.8. This means that the intensity of the NIR luminescence was gained about 6.6 times after the first stimulation. After 15 times of white LED stimulations, the intensity of the PSPL signal is still higher than that at the instant before the first stimulation. This PSPL properly extends the tracking window from several hours to more than 10 days, as shown in Figure 5.7c–e. Although the PSPL intensity dropped as the number of stimulations increased (Figure 5.9), the PSPL signals remained detectable even on day 10, at which time a still high S/N ratio of 24.6 was obtained. Note that an even longer tracking window, *e.g.*, one month, is expected if a less frequent stimulation scheme is adopted.[18]

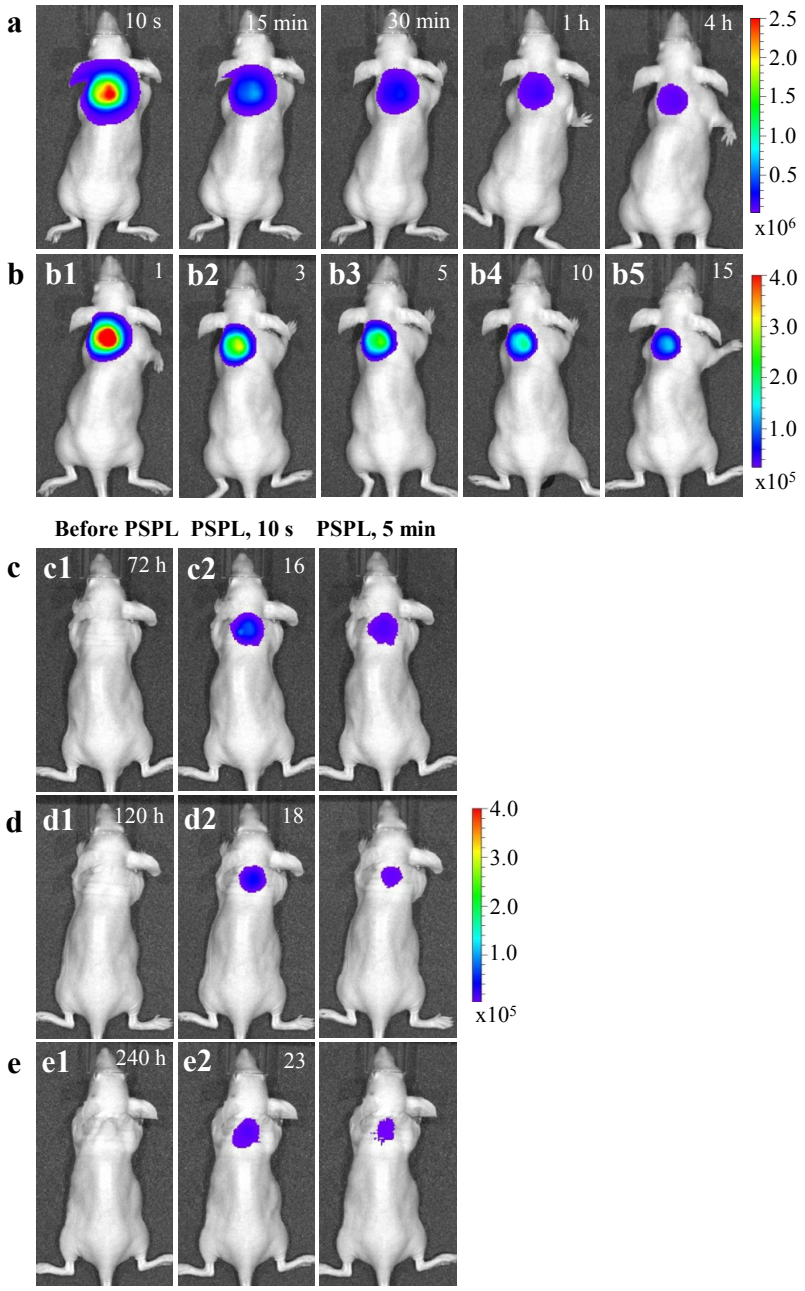

Figure 5.7 Acquisition of NIR persistent luminescence and NIR PSPL signals from PEI-LGO:Cr nanoparticles-labeled 4T1 cells. Pre-irradiated PEI-LGO:Cr nanoparticles labeled 4T1 cells (~2.5×10^{7} cells) were subcutaneously injected onto the back of a nude mouse. Row **a**, Decay of NIR persistent luminescence to 4 h. Starting from the 4 h time point, the mouse was exposed to a white LED flashlight to elicit NIR PSPL signals. Row **b**, PSPL images taken immediately (~10 s delay) after 1, 3, 5, 10, and 15 times of stimulation. Row **c–e**, PSPL images. From the 72 h time point, the mouse was irradiated daily by the LED flashlight (for 15 s), and imaged 10 s and 5 min after each stimulation. **c1**, **d1** and **e1** are the images taken right before the stimulation. The numbers at the upper right corners of the images in Row **b**, **c2**, **d2** and **e2** indicate the stimulation times.

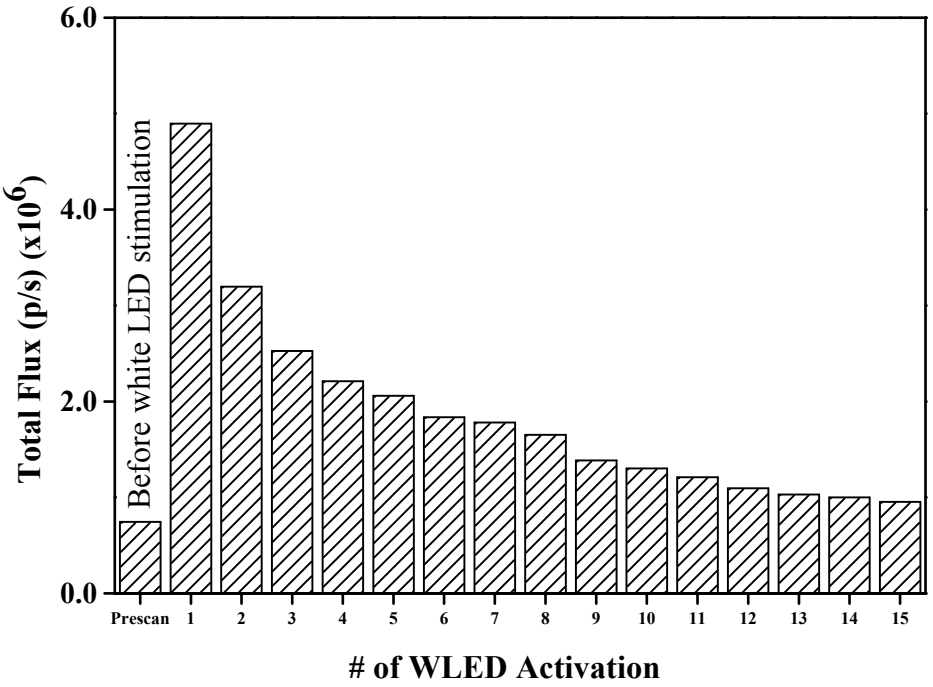

Figure 5.8 Quantification of the intensities of the PSPL signals in Figure 5.7b. In Figure 5.7b, only the PSPL images taken after 1, 3, 5, 10, 15 times of stimulations were shown. In this figure, all the PSPL intensities for the 15 times of stimulations are given.

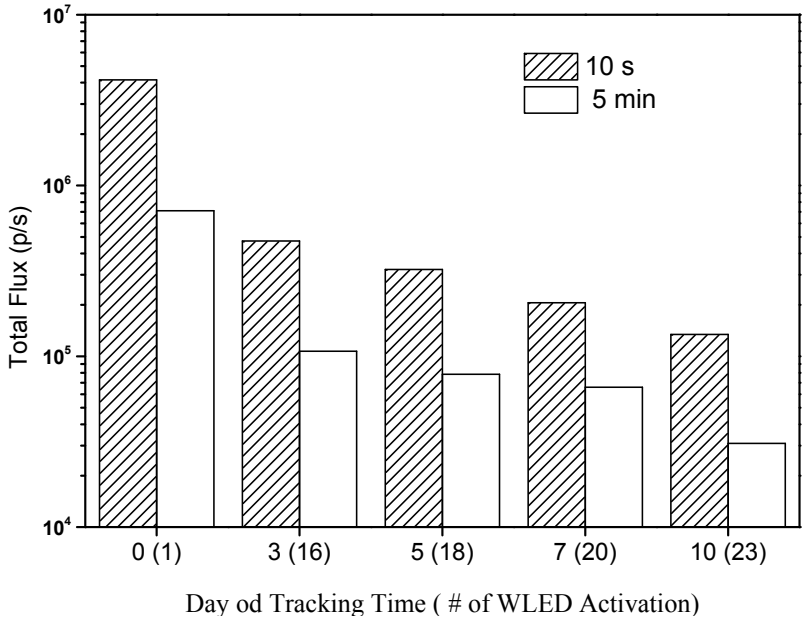

Figure 5.9 Quantification of the intensifies of the NIR PSPL signals in Figure 5.7, covering 10 days and a total of 23 times of stimulations.

5.4 *In vivo* NIR photostimulated persistent luminescence imaging of a mouse brain

The white LED flashlight can work as a non-invasive, safe, cheap and convenient switcher to turn on the LGO:Cr nanoparticles *in vivo*. Owing to the good tissue penetration of the white light and the high power of the Olight SR51 flashlight (900 lumens), the white LED stimulation is expected to lighten up LGO:Cr nanoparticles located in the tissues deeper than the skin region. This is verified by the imaging experiment in a mouse brain.

Experiments. About 25 μg PEI-LGO:Cr nanoparticles were irradiated by a 254 nm UV lamp for 15 min and then were implanted into the brain of a mouse (the location of the nanoparticles is about 2 mm beneath the head skin). At the 6 h, 72 h and 120 h time points, the mouse head was illuminated by a white LED flashlight for 15 s, and then imaged (1 min delay) on an IVIS imaging system in the bioluminescence mode with an exposure time of 2 min. The quantification was achieved by analyzing the NIR PSPL signals within the region of interests (ROIs) using Living Image software (Version 4.3.1 SP1).

Results and Discussion. As expected, intense NIR PSPL signals were repeatedly obtained over a 120 h period (Figure 5.10). At the 6 h time point, the PSPL signals at 30 min after the stimulation are still detectable by the IVIS imaging system (Figure 5.11). Although the PSPL signals at the 120 h time point only lasted to 10 min, it is sufficient to acquire the images.

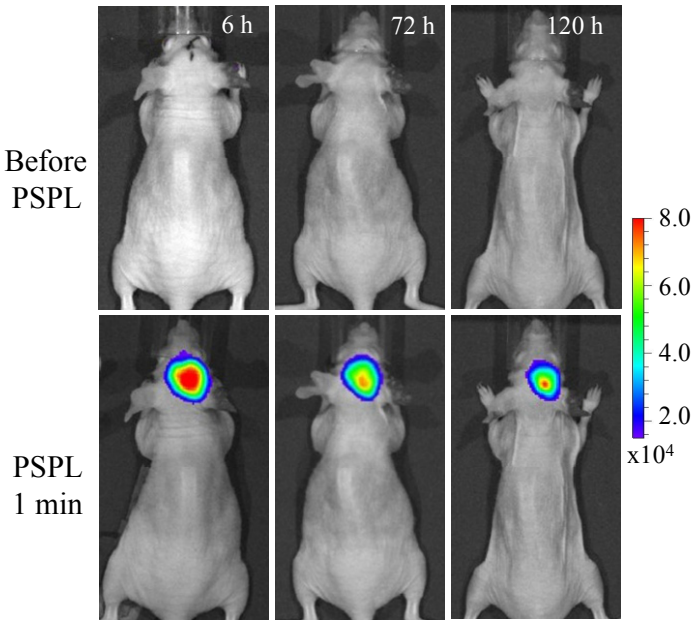

Figure 5.10 Stimulation and acquisition of NIR PSPL signals from PEI-LGO:Cr nanoparticles inoculated into the brain of a nude mouse. Images were taken at the 6 h, 72 h, and 120 h time points.

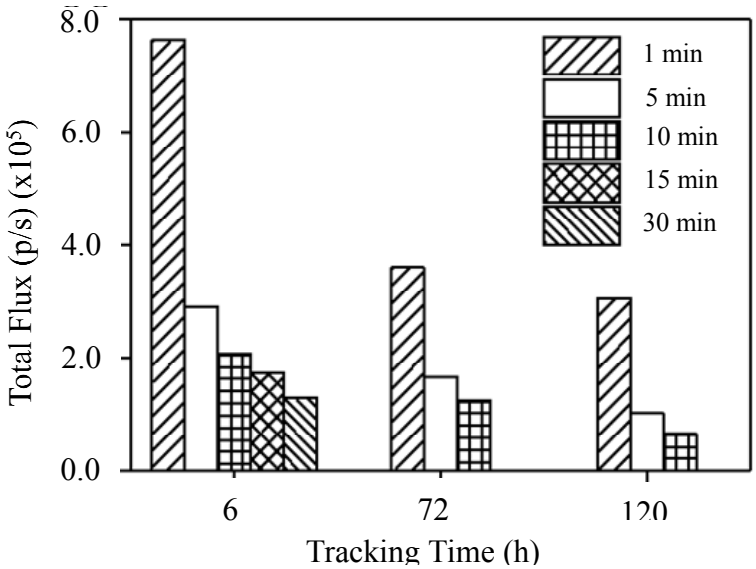

Figure 5.11 Quantification of the NIR PSPL signals in a mouse brain model in Figure 5.10. In the actual experiment, PSPL images were taken at 1, 5, 10, 15 and 30 min after the stimulation at the 6 h time point, and 1, 5 and 10 min after the stimulation at the 72 h and 120 h time points.

5.5 Long-term *in vivo* cell tracking and tumor targeting

The long-term tracking window *in vivo*, together with the high cell labeling efficiency, the high detection sensitivity and the deep-tissue imaging capability, makes the photostimulable LGO:Cr nanoparticles very suitable for long-term *in vivo* cell tracking and active tumor targeting.

5.5.1 *In vivo* cell tracking

Experiments. We performed a proof-of-concept cell tracking study by intravenously tail vein injecting PEI-LGO:Cr-bearing RAW264.7 cells into a 4T1 subcutaneous tumor model, and tracking their migration *in vivo*. PEI-LGO:Cr nanoparticles were UV pre-irradiated by a 254 nm UV lamp for 15 min, and then loaded into RAW264.7 cells for a 48 h incubation in the dark. The labeled RAW264.7 cells (~1.0×10^6 cells) were intravenously injected under a safelight condition to avoid energy loss caused by regular room-light illumination. Whole body luminescence images were acquired before and after illuminating the mouse by a white LED flashlight (for 15 s) at 30 min, 24 h, and 72 h after the cell injection (Figure 5.12). All images were acquired on an IVIS imaging system in the bioluminescence mode with an exposure time of 3 min.

After imaging, mice were sacrificed by cervical dislocation under deep isoflurane anesthesia. Tumor, liver, lung, spleen, kidney, heart, and brain were harvested, UV-irradiated, and then subjected to bioluminescence imaging using an IVIS imaging system (Figure 5.13). NIR persistent luminescence images were acquired on an IVIS Lumina II imaging system in the bioluminescence mode with the emission filter set as “open”, and with an exposure time of 5 min. The fluxes (in photons per second) of luminescence from the organs and tumor before and after the UV excitation were recorded on the IVIS system. Biodistribution of the NIR persistent luminescence signals from the organs and tumor was calculated by the net flux of each organ as

well as the tumor. The net flux was obtained by subtracting the flux obtained before UV excitation from the flux obtained after UV excitation. The net flux of each organ and tumor was then normalized to that of the liver.

Later, the tumors collected from the mice were then snap-frozen, cut into 6–8 μm thick sections, and mounted on a coverslip. After fixed in acetone at room temperature for about 2 h, the sections were gently washed with 1× PBS (pH 7.4) for 3 times, irradiated by a 254 nm UV lamp for 5 min, and subjected to bioluminescence histology study on a Olympus LV200 microscope (Figure 5.14).

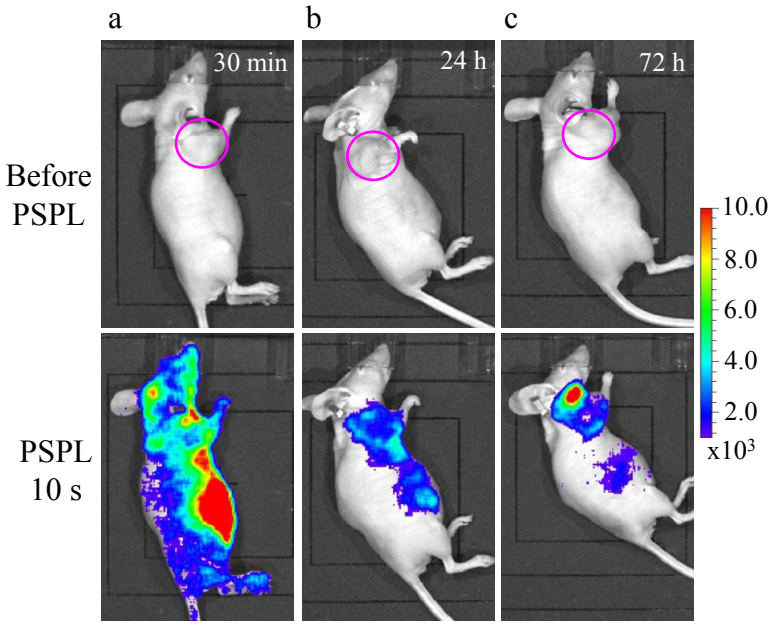

Figure 5.12 *In vivo* cell tracking with PEI-LGO:Cr labeled RAW264.7 cells. Whole body luminescence images were acquired before and after illuminating the mouse by a white LED flashlight (for 15 s) at 30 min (**a**), 24 h (**b**), and 72 h (**c**) after the cell injection. The tumor sites are indicated by pink circles.

Results and discussion. Since the UV pre-irradiated LGO:Cr nanoparticles had already experienced 48 h of decay in the incubation process at the instant of injection, the intensity of the NIR persistent luminescence signals *in vivo* was too low to be detected by the IVIS imaging

system (see the top row images in Figure 5.12). However, intense NIR PSPL signals can be elicited by short-time (15 s) white LED stimulation. Imaging at 30 min after the injection (bottom image in Figure 5.12a) revealed NIR PSPL signals all over the mouse body, with the most intensive signals in the liver and the intestine. At 72 h, however, most signals were found in the tumor area (bottom image in Figure 5.12c). Such tropism is expected because macrophages are an important player in tumor proliferation and angiogenesis, and are heavily recruited to tumor sites,[239] as was observed by others.[240,241] After the 72 h imaging, the animal was sacrificed to be used in *ex vivo* biodistribution study. The *ex vivo* biodistribution study revealed the strongest NIR persistent luminescence signals in the tumor (Figure 5.13), consistent with the *in vivo* results.

The tumor was further studied using a LV200 bioluminescence microscope. The bioluminescence microscopy study showed inhomogeneous but strong presence of LGO:Cr nanoparticles in the tumor, as shown in Figure 5.14. To our knowledge, the present study is the first demonstration on harnessing persistent luminescence for *in vivo* cell tracking and *ex vivo* histology examination. Moreover, the strong NIR PSPL signals from such deep organs as liver and intestine further confirm that the LGO:Cr nanoparticles in the deep tissues can be readily elicited to emit NIR PSPL by white light illumination. This capability combined with the high penetration depth of the NIR light, suggests that the LGO:Cr-based imaging can be used for whole mouse study.

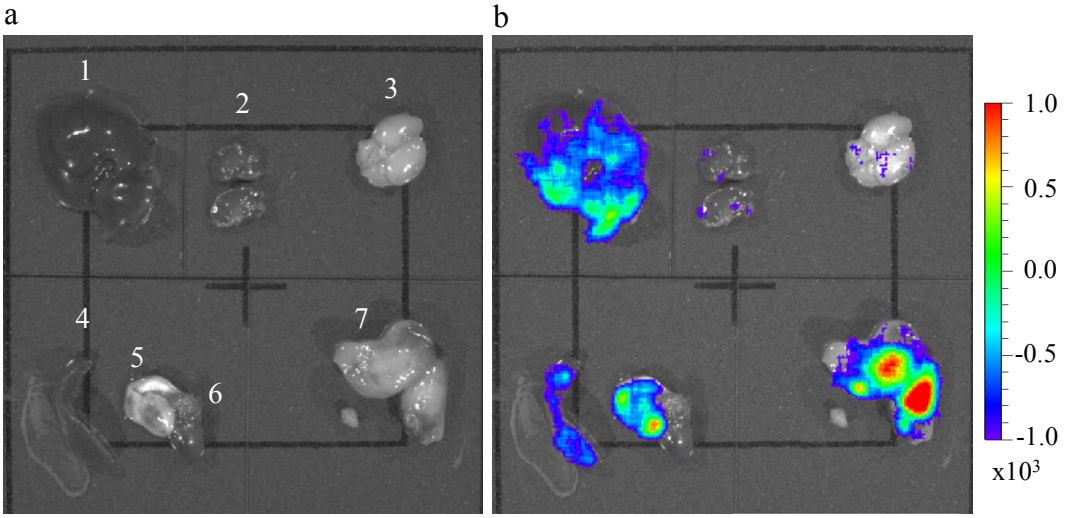

c

Organs	Normalized Percentage of Total Flux (%)	Relative Standard Derivation (RSD) (%)
Liver	100.0	2.5
Tumor	111.3	0.8
Lung	30.0	6.2
Spleen	13.6	2.2
Kidney	3.5	9.9
Heart	1.6	17.8
Brain	2.2	6.9

Figure 5.13 *Ex vivo* images and biodistribution of NIR persistent luminescence signals among tumor and major mouse organs for cell tracking with PEI-LGO:Cr nanoparticles labeled RAW264.7 cells in 4T1 tumor model. **a**, Background image of major organs, including liver (1), kidneys (2), brain (3), spleen (4), lung (5) and heart (6), and tumor (7) before UV irradiation. **b**, Image taken after the organs and tumor were irradiated by a 254 nm UV lamp for 15 min. The signals were attributed to the NIR persistent luminescence from the LGO:Cr nanoparticles. **c**, Biodistribution of the NIR persistent luminescence signals from the organs and tumor.

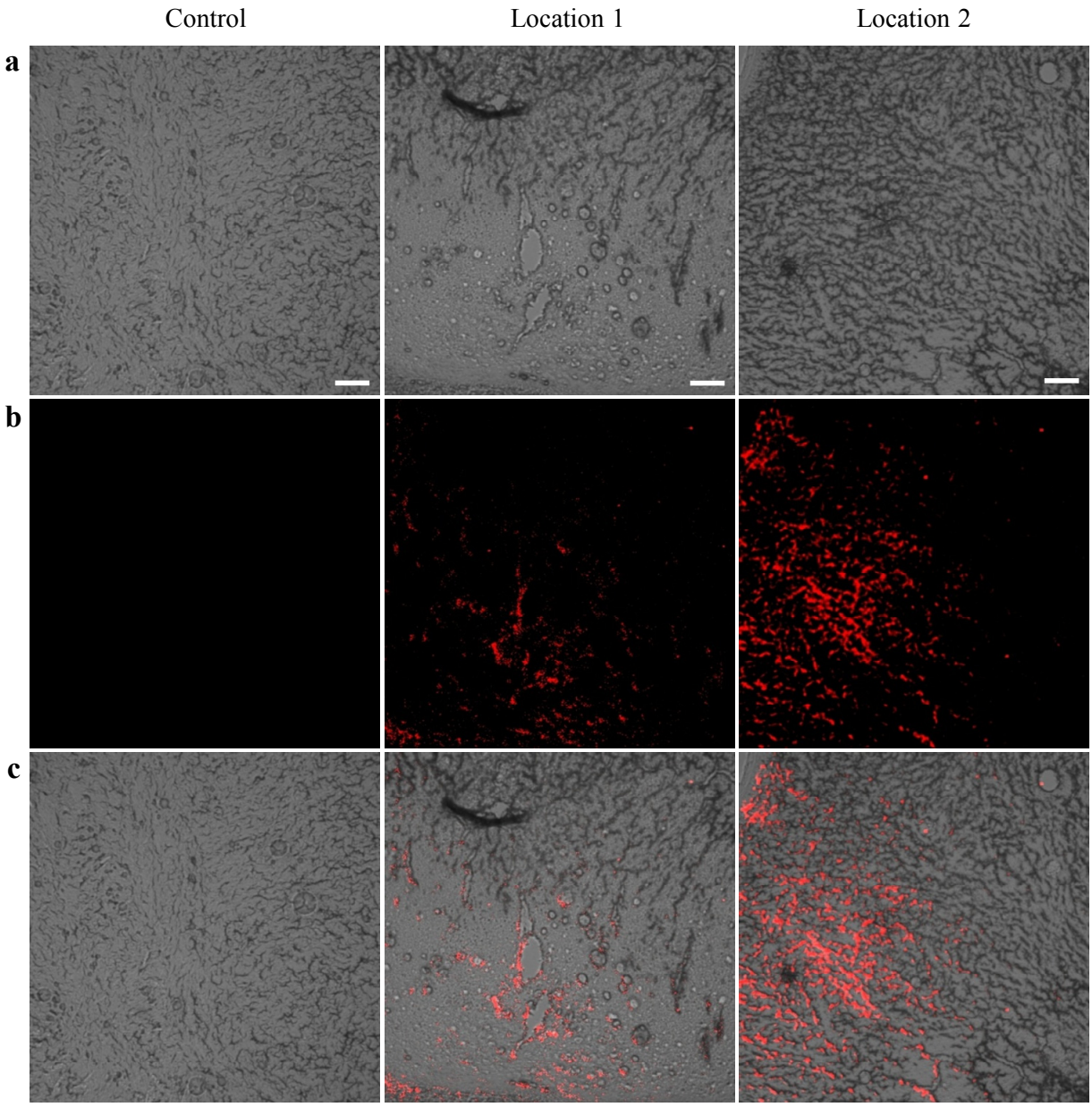

Figure 5.14 Microscopic study of 4T1 tumors with/without PEI-LGO:Cr labeled RAW264.7 cells. Row **a**, Bright-field images of control 4T1 tumor and labeled 4T1 tumor (in two locations). (Scale bars, 200 μm). Row **b**, Bioluminescence images of 4T1 tumors. Row **c**, Merged images by overlapping the same column images in Row **a** and Row **b**.

5.5.2 *In vivo* active targeting imaging

Besides cell tracking, the LGO:Cr nanoparticles can also be used for tumor targeting if appropriate surface chemistry for nanoparticle modification is applied. We adapted c(RGDyK)-LGO:Cr nanoparticles for active targeting, since cRGD is a small peptide with high affinity toward integrin $\alpha_v\beta_3$, a tumor biomarker overexpressed on tumor vasculature as well as on tumor cells of various types.[242]

Experiments. To prepare c(RGDyK)-LGO:Cr nanoparticles for *in vivo* active targeting, the LGO:Cr nanoparticles were first modified using PVP and HSA, and then conjugated with c(RGDyK) peptides. The LGO:Cr nanoparticles were coated by human serum albumin (HSA) proteins, because the albumin molecules possess certain functional groups (*e.g.*, amino- and carboxyl- groups) that can form covalent bonding with targeting molecules, c(RGDyK) peptides.[162,163] The HSA-coated LGO:Cr nanoparticles were prepared using the following procedure. LGO:Cr nanoparticles were dispersed in ethanol to a concentration of 1 mg/mL. PVP (MW = 40k) was added into the solution, and the mixture was magnetically stirred in dark for 48 h. The resulting PVP-LGO:Cr nanoparticles were collected *via* centrifugation and washed with ethanol for 3 times. The purified PVP-LGO:Cr nanoparticles were added to a HSA solution (3 mg HSA/mL), and the mixture was incubated for 4 h. HSA proteins were adsorbed onto the surface of LGO:Cr nanoparticles, and the product was collected by centrifugation and washed with water for 3 times. For bioconjugation, the HSA-coated LGO:Cr nanoparticles were first reacted with bis(sulfosuccinimidyl) suberate (BS^3, Thermo Scientific) in a 50 mM borate buffer solution (pH 8.0) for 30 min at room temperature. The particles were purified by centrifugation and re-dispersed in PBS (pH 7.4). The c(RGDyK) peptide was added to the solution, and the

reaction was conducted at room temperature for 2 h. The final products as c(RGDyK)-conjugated LGO:Cr nanoparticles were purified by centrifugation and re-dispersed in PBS.

0.5 mg c(RGDyK)-LGO:Cr nanoparticles were irradiated by a 254 nm UV lamp for 15 min before intravenous tail vein injection. Luminescence images were acquired before and after the stimulation (for 15 s) by a LED flashlight at 6 h and 24 h after the injection (Figure 5.15). All images were acquired on an IVIS Lumina II imaging system in the bioluminescence mode with an exposure time of 3 min. After imaging, the mouse was sacrificed. The tumor and the different mouse organs were collected and UV-irradiated, and then subjected to *ex vivo* biodistribution study on an IVIS imaging system (Figure 5.16).

Results and discussion. Figure 5.15 shows a tumor targeting study where c(RGDyK)-LGO:Cr nanoparticles were intravenously injected into 4T1 tumor bearing mice (n = 3). The intensity of the NIR PSPL signals in the 4T1 tumor region was much higher than other region several hours post the injection. This suggests that the c(RGDyK)-LGO:Cr nanoparticles accumulated in tumor. After imaging, *ex vivo* evaluation of NIR persistent luminescence from dissected organs and tumor at 24 h post-injection revealed good accumulation of nanoparticles in the 4T1 tumor, as shown in Figure 5.16. The *ex vivo* observation is consistent with the *in vivo* imaging study. It should be noted that 24 h post-injection provided enough time for the nanoparticles to reach most organs through blood stream circulation and diffusion.[201] It is anticipated that other targeting molecules, either antibody-, peptide-, or aptamer-based, can be coupled onto LGO:Cr nanoparticles to allow for targeting different specific biomarkers.

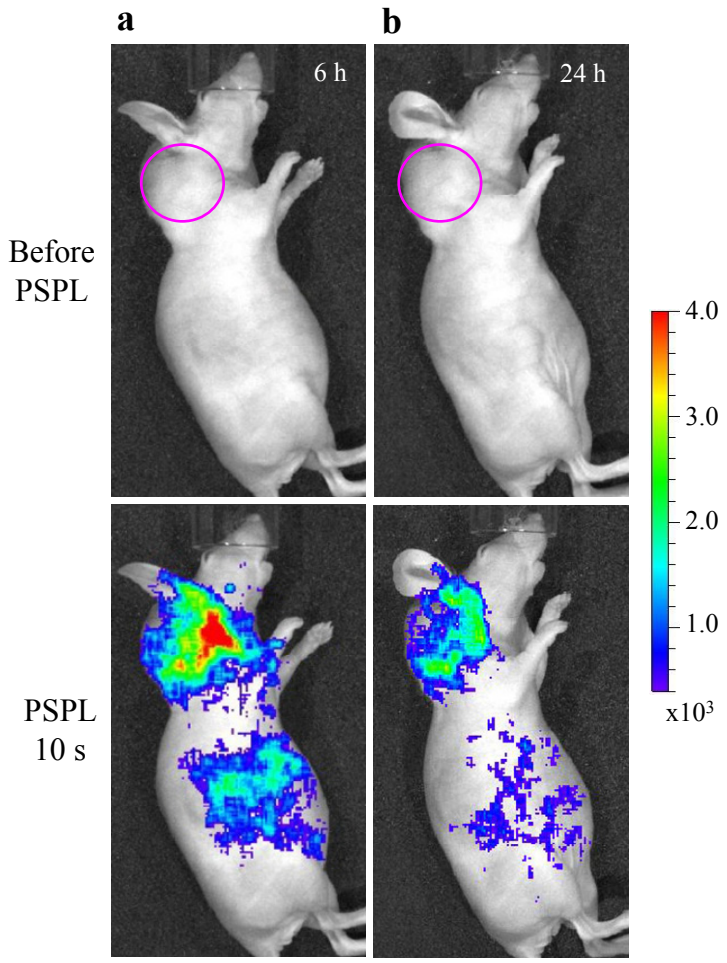

Figure 5.15 *In vivo* active tracking with c(RGDyK)-LGO:Cr nanoparticles. Whole body luminescence images were acquired before and after illuminating the mouse by a white LED flashlight (for 15 s) at 6 h (**a**), and 24 h (**b**) after the nanoparticles injection. The tumor sites are indicated by pink circles.

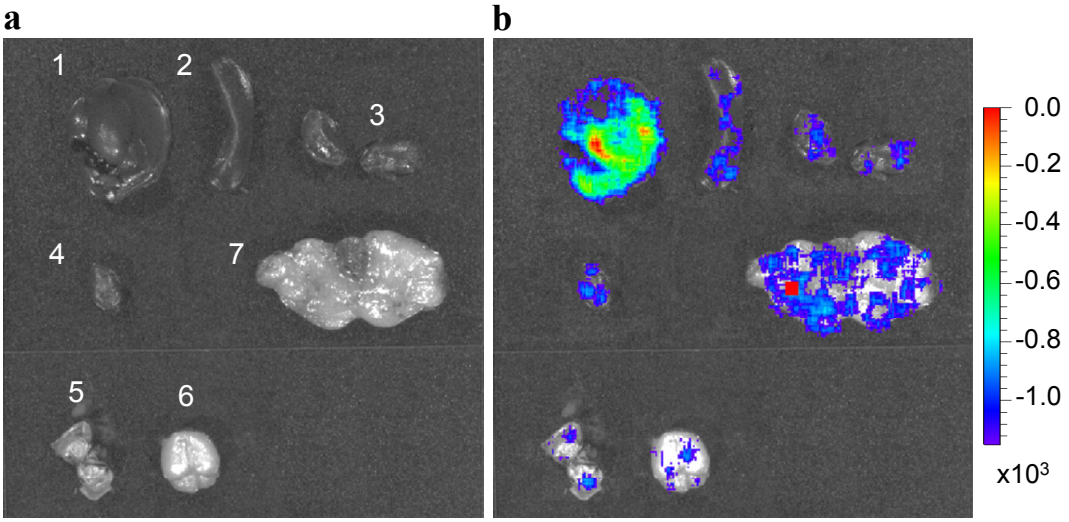

c

Organs	Normalized Percentage of Total Flux (%)	Relative Standard Derivation (RSD) (%)
Liver	100.0	2.6
Tumor	122.0	0.6
Lung	9.5	18
Spleen	13.4	20.4
Kidney	11.9	15.6
Heart	4	13.9
Brain	6.3	3

Figure 5.16 *Ex vivo* images and biodistribution of NIR persistent luminescence signals among tumor and major mouse organs for active tumor targeting with c(RGDyK)-LGO:Cr nanoparticles in 4T1 tumor model. **a**, Background image of major organs, including liver (1), spleen (2), kidney (3), heart (4), lung (5) and brain (6), and tumor (7) before UV irradiation. **b**, Image taken after the organs and tumor were irradiated by a 254 nm UV lamp for 15 min. The signals were attributed to the NIR persistent luminescence from the LGO:Cr nanoparticles. **c**, Biodistribution of the NIR persistent luminescence signals from the organs and tumor.

5.6 Summary

We have developed a new type of optical nanoprobes, LGO:Cr NIR persistent luminescent nanoparticles, with strong, long-lasting, and photostimulable NIR persistent luminescence that allows for ultrasensitive, deep-tissue, and long-term tracking of cells and molecule objects *in vivo*. This LGO:Cr-based imaging technique can be conveniently used on existing imaging systems to improve the quality and capacity of optical imaging, and holds the following promising prospects. Firstly, for cell tracking, LGO:Cr nanoparticles offers sensitivity and penetration depths that are comparable or superior to bioluminescence which is by far the most sensitive optical method. Unlike bioluminescence-based cell tracking that requires tedious and sometimes challenging transfection to label cells as well as repeated injection of enzyme substrates, cell labeling with LGO:Cr nanoparticles demands no more than simple incubation. In addition, LGO:Cr-labeled cells can be examined histologically, an option that is not possible with bioluminescence-based cell tracking because luciferase proteins cannot survive the process of tissue fixation. Secondly, LGO:Cr-based imaging allows one to "see" through a mouse body, breaking the dogma that optical imaging can only investigate superficial conditions. The underlying impact can be tremendous. Taking cancer research as an example, orthotopic, spontaneous and metastatic tumor models, which were previously studied by more expensive and less available imaging tools such as PET, are now able to be investigated on an optical imaging system. Such a transition would save massive cost and significantly expedite the process of basic research and drug development.[31] Thirdly, our cellular imaging results suggest great promise of LGO:Cr nanoparticles in quantitative cell assays such as flow cytometry and immunostaining. The advantages, aside from a clean background, also include the exceptional photo- and chemical-stability of the LGO:Cr nanoparticles. Fourthly, owing to a deep penetration depth

(>3.7 cm with 150 μg LGO:Cr nanoparticles) of the NIR luminescence, LGO:Cr nanoparticles also have a perspective in clinical translation for, for instance, mapping lymph nodes, most of which are about 3 cm beneath the skin of human beings.[243] This is possible due to the biocompatibility of LGO:Cr, given that all the three comprising metals are relatively well tolerated.

CHAPTER 6

CONCLUSION

In this dissertation, a new, novel type of photostimulable NIR persistent luminescent phosphor, $LiGa_5O_8:Cr^{3+}$ (LGO:Cr), in the forms of solid ceramics and nanoparticles were developed and investigated, and the applications of LGO:Cr nanoparticles as optical nanoprobes in bioimaging were comprehensively studied. The studies show that the LGO:Cr phosphors are not only superb NIR (peaking at 716 nm) persistent materials exhibiting a super-long persistent luminescence of more than 1,000 h, which is the longest persistent luminescence reported to date, but also remarkable photostimulable storage media exhibiting a new optical read-out form – photostimulated persistent luminescence (PSPL) in the NIR. Owing to the high-penetrating power of the NIR light in tissues and the very-long persistent luminescence and the unique PSPL capability of the LGO:Cr nanoparticles, the LGO:Cr nanoparticles-based bioimaging offers a excitation-free and thus autofluorescence-free imaging condition. The bioimaging studies reveal promising potential of these LGO:Cr nanoprobes in cell tracking and tumor targeting, exhibiting very-long imaging window (>10 days) and exceptional sensitivity and penetration that far exceed those afforded by conventional fluorescence imaging.

The main conclusions of this dissertation are summarized as below.

New, novel Cr^{3+}-doped $LiGa_5O_8$ (LGO:Cr) NIR persistent luminescent ceramics. The LGO:Cr ceramics were fabricated by a solid-state reaction method, in which stoichiometric amounts of Li_2CO_3, Ga_2O_3 and Cr_2O_3 powders were sintered at 1300 °C in a high temperature furnace in air. The LGO:Cr ceramic phosphors can be effectively activated by a broad range of

wavelengths ranging from ~250 nm to ~660 nm and emit a narrow NIR photoluminescence band (~650–850 nm peaking at 716 nm) attributed to the spin-forbidden Cr^{3+} $^2E \rightarrow {}^4A_2$ transition. After irradiation with a 254 nm UV lamp for a short time, e.g., 1 min, the energy stored in the LGO:Cr phosphor can sustain a very long NIR persistent luminescence of more than 1000 h. Remarkably, an intense NIR PSPL signal peaking at 716 nm can be repeatedly obtained in a period of more than 2000 h when an UV pre-irradiated LGO:Cr ceramic is repeatedly stimulated with a white LED flashlight.

Cr^{3+}-doped $LiGa_5O_8$ (LGO:Cr) NIR persistent nanoparticles. The LGO:Cr nanoparticles were synthesized by a sol-gel method using $LiNO_3$, $Ga(NO_3)_3$ and $Cr(NO_3)_3$ as the precursors, followed by calcinations at 1100 ˚C and then wet mechanical grinding. The particle sizes are in the range of 50–100 nm. The LGO:Cr nanoparticles exhibit the similar NIR photoluminescence, NIR persistent luminescence and NIR PSPL properties as their ceramic counterpart, except for a shorter detectable persistent luminescence time (~100 h) due to the smaller particle volume. The LGO:Cr nanoparticles are chemically stable over a broad range of pH from 3.0 to 11.0.

Easy surface modification and functionalization of LGO:Cr nanoparticles. The LGO:Cr nanoparticles can be readily encapsulated with PEI and PVP polymers, coated with silica shells, or conjugated with HSA proteins and c(RGDyK) peptides. The PEI- and PVP-encapsulated LGO:Cr nanoparticles remain stable in aqueous solutions for more than 72 h and 48 h, respectively. For silica coating, the thickness of the silica layer can be tune from 1 nm to 10 nm by adjusting the reaction parameters. The ability to be conjugated with c(RGDyK) peptides enables the LGO:Cr nanoparticles to be used for active tumor targeting.

Low cytotoxicity of LGO:Cr nanoparticles. The cytotoxicity of the PEI-LGO:Cr nanoparticles were evaluated on a variety of cell lines, including 4T1 murine breast cancer cells,

RAW264.7 murine macrophage cells, and murine ESCs. Although the viability of the three cell lines decreased as the nanoparticle concentration increased, the evaluations showed >80% viability in the tested concentrations up to 100 μg/mL after 24 h of incubation with 4T1 cells and RAW264.7 cells, and 72 h with ESCs. In addition, the PEI-LGO:Cr nanoparticles also showed low impact to cell renewal and differentiation using three key biomarkers: Nanog, Nestin and Sox17.

Efficient internalization of PEI-LGO:Cr nanoparticles in RAW264.7 cells and 4T1 cells. Thin sectional TEM study showed that the PEI-LGO:Cr nanoparticles can be efficiently internalized by RAW264.7 and 4T1 cells via endocytosis of the cells, and the internalized nanoparticles can be transferred to daughter cells up to three generations in a 6 days incubation. The amount of LGO:Cr nanoparticles internalized by RAW264.7 cells was quantified as ~15.85 pg per cell by the ICP-MS method, while the amount internalized by 4T1 cells was estimated as ~6.89 pg per cell by the persistent luminescence measurement.

***In vitro* cell imaging based on NIR persistent luminescence and NIR PSPL signals.** Individual 4T1 cells labeled with PEI-LGO:Cr nanoparticles were clearly visualized using an Olympus LV200 bioluminescence microscope. This is the first visualization and imaging of individual cells based on persistent luminescence signals. Significantly, the intensity of the NIR persistent luminescence from the LGO:Cr nanoparticles is comparable to that of the bioluminescence from firefly luciferase (f-luc); the latter is the most sensitive optical imaging probe for cell tracking. Moreover, by making use of the unique PSPL property, the *in vitro* tracking window for the PEI-LGO:Cr nanoparticles labeled 4T1 cells was expanded to 8 days using an IVIS Lumina II imaging system.

Excellent detection sensitivity of LGO:Cr nanoparticle-based bioimaging. Due to the elimination of the external excitation and along with it, the autofluorescence, the background noise in animal bioimaging is at the minimum. This enables the PEI-LGO:Cr nanoparticle labeled RAW264.7 cells to be visualized at an exceptionally high sensitivity of as few as ~5 cells. This sensitivity is comparable to the f-luc-based cell tracking, but several orders of magnitude higher than that of QDs and organic dyes.

The benefit brought by the LGO:Cr nanoparticles' excitation-free imaging condition was perfectly reflected in comparison experiments with QDs. It shows that with the same amount of LGO:Cr nanoparticles and QDs, the LGO:Cr-based imaging yielded a S/N ratio about an order of magnitude higher than the QDs-based imaging.

Deep detection depth of LGO:Cr nanoparticle-based bioimaging. Since the emission (716 nm) of LGO:Cr nanoparticles is in the first tissue transparency window, the LGO:Cr nanoparticle-based imaging exhibited deeper tissue penetration than the green-emitting f-luc-based imaging. In the experiments using pork as the tissue model, detection depths of 2.5 cm and 3.7 cm were achieved when 15 μg and 150 μg LGO:Cr nanoparticles were injected into the pork, respectively. Such penetration depths are significantly greater than those afforded by the fluorescence imaging (< 1 cm), bioluminescence imaging (< 2 cm) and upconversion luminescence imaging (< 2 cm).

Longitudinal *in vivo* monitoring based on LGO:Cr nanoparticles' PSPL property. For LGO:Cr nanoparticles-bearing 4T1 cells (~2.5×10^7 cells) implanted into a mouse (the cells were pre-irradiated by a 254 nm UV lamp before the injection), the initial NIR persistent luminescence signals were detectable for about 4 h. The tracking window can be significantly extended by making use of the LGO:Cr nanoparticles' PSPL capability. Our imaging

experiments showed that LGO:Cr nanoparticles pre-charged by UV light were able to be repeatedly (>20 times) stimulated *in vivo*, even in deep tissues (such as in brain), by short-exposure (~15 seconds) to a white LED flashlight, giving rise to multiple NIR PSPL that extended the tracking window from hours to 10 days. Such a long tracking window is sufficient for longitudinal *in vivo* cell tracking which needs a window of days or even weeks.

Long-term *in vivo* cell tracking and active tumor targeting. A proof-of-concept cell tracking study was performed by intravenously tail vein injecting UV pre-irradiated PEI-LGO:Cr-bearing RAW264.7 cells into a 4T1 subcutaneous tumor model, and tracking their migration *in vivo*. Intense PSPL signals were detected in the tumor area 72 h after the injection, showing significant recruitment of the PEI-LGO:Cr-bearing RAW264.7 cells in the tumor site. This *in vivo* tracking result was confirmed by subsequent *ex vivo* biodistribution study and *ex vivo* histology examination from the collected tumors.

LGO:Cr nanoparticles were used as tags of targeting molecules, c(RGDyK) peptide, for cancer imaging. The c(RGDyK)-conjugated LGO:Cr nanoparticles were intravenously injected into 4T1 tumor bearing mice, and showed good accumulation in the tumors 6 h after the injection. The *in vivo* observation was consistent with the *ex vivo* imaging study of the collected tumors.

REFERENCES

1 Braslavsky SE (2007) Glossary of terms used in photochemistry 3rd edition (IUPAC recommendations 2006). *Pure Appl Chem* 79:293.
2 Valeur B, Berberan-Santos MN (2011) A brief history of fluorescence and phosphorescence before the emergence of quantum theory. *J Chem Educ* 88:731.
3 McKeever SWS (1988) *Thermoluminescence of Solids* (Cambridge).
4 Blasse G, Grabmaier BC (1994) *Luminescent Materials* (Springer).
5 Shinde KN, Dhoble SJ, Swart HC, Park K (2012) *Phosphate Phosphors for Solid-State Lighting* (Springer).
6 Yen WM, Shionoya S, Yamamoto H (2007) *Phosphor Handbook*, 2nd ed. (CRC).
7 Lakowicz JR (2007) *Principles of Fluorescence Spectroscopy* (Springer).
8 Kitai A (2008) *Luminescent Materials and Applications* (Wiley).
9 Ronda CR (2008) *Luminescence: From Theory to Applications* (Wiley).
10 Yen WM, Shionoya S, Yamamoto H (2006) *Fundamentals of Phosphors* (Taylor & Francis).
11 Albani JR (2008) *Principles and Applications of Fluorescence Spectroscopy* (Wiley).
12 Schweizer S (2001) Physics and current understanding of x-ray storage phosphors. *Phys Status Solidi A* 187:335.
13 Brito HF*, et al.* (2012) Persistent luminescence mechanisms: human imagination at work. *Opt Mater Express* 2:371.
14 Yukihara EG, McKeever SWS (2011) *Optically Stimulated Luminescence: Fundamentals and Applications* (Wiley).
15 Meijerink A, Blasse G (1991) Photostimulated luminescence and thermally stimulated luminescence of some new X-ray storage phosphors. *J Phys D: Appl Phys* 24:626.
16 Von Seggern H (1999) Photostimulable X-ray storage phosphors: a review of present understanding. *Braz J Phys* 29:254.
17 Riesen H, Liu ZQ (2012) *Current Topics in Ionizing Radiation Research* (InTech).
18 Liu F*, et al.* (2013) Photostimulated near-infrared persistent luminescence as a new optical read-out from Cr^{3+}-doped $LiGa_5O_8$. *Sci Rep* 3:1554.
19 Hölsä J (2009) Persistent luminescence beats the afterglow: 400 years of persistent luminescence. *Electrochem Soc Interface* 18:42.
20 Chen R, McKeever SWS (1997) *Theory of Thermoluminescence and Related Phenomena* (World Scientific).
21 Van den Eeckhout K, Smet PF, Poelman D (2010) Persistent luminescence in Eu^{2+}-doped compounds: a review. *Materials* 3:2536.
22 Dodeigne C, Thunus L, Lejeune R (2000) Chemiluminescence as diagnostic tool. A review. *Talanta* 51:415.
23 Badr CE, Tannous BA (2011) Bioluminescence imaging: progress and applications. *Trends Biotechnol* 29:624.
24 Weissleder R, Pittet MJ (2008) Imaging in the era of molecular oncology. *Nature* 452:580.
25 Ehman RL*, et al.* (2007) Blueprint for imaging in biomedical research. *Radiology* 244:12.
26 Baker M (2010) Whole-animal imaging: the whole picture. *Nature* 463:977.
27 De Chermont QLM*, et al.* (2007) Nanoprobes with near-infrared persistent luminescence for *in vivo* imaging. *Proc Natl Acad Sci USA* 104:9266.
28 Choy G*, et al.* (2003) Comparison of noninvasive fluorescent and bioluminescent small animal optical imaging. *Biotechniques* 35:1022.
29 Massoud TF, Gambhir SS (2003) Molecular imaging in living subjects: seeing fundamental biological processes in a new light. *Genes Dev* 17:545.
30 So MK, Xu CJ, Loening AM, Gambhir SS, Rao JH (2006) Self-illuminating quantum dot conjugates for *in vivo* imaging. *Nat Biotechnol* 24:339.
31 Willmann JK, van Bruggen N, Dinkelborg LM, Gambhir SS (2008) Molecular imaging in drug development. *Nat Rev Drug Discovery* 7:591.
32 Wu YC, Xi P, Ge WK, Yuen PW, Qu JY (2004) Fluorescence spectroscopy of biological tissue: single- and two-photon excitation. In: *Multiphoton Microscopy in the Biomedical Sciences IV*, Periasamy A, So OTC, eds. Proceeding of SPIE, 5323:377.
33 Wang LV, Wu H (2007) *Biomedical Optics: Principles and Imaging* (Wiley).

34 Quist A, Timchenko V, Dombrovsky LA (2012) A simplified model of laser hyperthermia of superficial tumors including variation of human tissue optical properties with thermal damage. In: *ASME 2012 International Mechanical Engineering Congress and Exposition*: *Biomedical and Biotechnology*, Coats M, eds. Proceeding of IMECE, 2:701.
35 Vo-Dinh T (2003) *Biomedical Photonics Handbook* (Taylor & Francis).
36 Quek CH, Leong KW (2012) Near-infrared fluorescent nanoprobes for *in vivo* optical imaging. *Nanomaterials* 2:92.
37 Welsher K, Sherlock SP, Dai HJ (2011) Deep-tissue anatomical imaging of mice using carbon nanotube fluorophores in the second near-infrared window. *Proc Natl Acad Sci USA* 108:8943.
38 Jacques SL (2013) Optical properties of biological tissues: a review. *Phys Med Biol* 58:R37.
39 Luo SL, Zhang EL, Su YP, Cheng TM, Shi CM (2011) A review of NIR dyes in cancer targeting and imaging. *Biomaterials* 32:7127.
40 Panchuk-Voloshina N*, et al.* (1999) Alexa dyes, a series of new fluorescent dyes that yield exceptionally bright, photostable conjugates. *J Histochem Cytochem* 47:1179.
41 Shu XK*, et al.* (2009) Mammalian expression of infrared fluorescent proteins engineered from a bacterial phytochrome. *Science* 324:804.
42 Chalfie M, Tu Y, Euskirchen G, Ward WW, Prasher DC (1994) Green fluorescent protein as a marker for gene-expression. *Science* 263:802.
43 Filonov GS*, et al.* (2011) Bright and stable near-infrared fluorescent protein for *in vivo* imaging. *Nat Biotechnol* 29:757.
44 Michalet X*, et al.* (2005) Quantum dots for live cells, *in vivo* imaging, and diagnostics. *Science* 307:538.
45 Resch-Genger U, Grabolle M, Cavaliere-Jaricot S, Nitschke R, Nann T (2008) Quantum dots versus organic dyes as fluorescent labels. *Nat Methods* 5:763.
46 Walling MA, Novak JA, Shepard JRE (2009) Quantum dots for live cell and *in vivo* imaging. *Int J Mol Sci* 10:441.
47 Aswathy RG, Yoshida Y, Maekawa T, Kumar DS (2010) Near-infrared quantum dots for deep tissue imaging. *Anal Bioanal Chem* 397:1417.
48 Welsher K*, et al.* (2009) A route to brightly fluorescent carbon nanotubes for near-infrared imaging in mice. *Nat Nanotechnol* 4:773.
49 Wang F, Banerjee D, Liu YS, Chen XY, Liu XG (2010) Upconversion nanoparticles in biological labeling, imaging, and therapy. *Analyst* 135:1839.
50 Xiong L, Shuhendler AJ, Rao J (2012) Self-luminescing BRET-FRET near-infrared dots for *in vivo* lymph-node mapping and tumour imaging. *Nat Commun* 3:1193.
51 Haugland RP, Spence MTZ, Johnson ID (2005) *The Handbook: A Guide to Fluorescent Probes and Labeling Technologies*, 10th ed.(Molecular Probes).
52 Sapsford KE, Berti L, Medintz IL (2006) Materials for fluorescence resonance energy transfer analysis: beyond traditional donor–acceptor combinations. *Angew Chem Int Ed* 45:4562.
53 Alander JT*, et al.* (2012) A review of indocyanine green fluorescent imaging in surgery. *Int J Biomed Imaging* 2012:940585.
54 Labas YA*, et al.* (2002) Diversity and evolution of the green fluorescent protein family. *Proc Natl Acad Sci USA* 99:4256.
55 Shaner NC*, et al.* (2004) Improved monomeric red, orange and yellow fluorescent proteins derived from *Discosoma* sp. red fluorescent protein. *Nat Biotechnol* 22:1567.
56 Wang L, Jackson WC, Steinbach PA, Tsien RY (2004) Evolution of new nonantibody proteins *via* iterative somatic hypermutation. *Proc Natl Acad Sci USA* 101:16745.
57 Zimmer M (2009) GFP: from jellyfish to the Nobel prize and beyond. *Chem Soc Rev* 38:2823.
58 Shcherbakova DM, Verkhusha VV (2013) Near-infrared fluorescent proteins for multicolor *in vivo* imaging. *Nat Meth* 10:751.
59 Feng W, et al. (2006) Luminescent nanomaterials for biological labelling. *Nanotechnology* 17:R1.
60 Mazumder S, Dey R, Mitra MK, Mukherjee S, Das GC (2009) Biofunctionalized quantum dots in biology and medicine. *J Nanomater* 2009:1.
61 Medintz IL, Uyeda HT, Goldman ER, Mattoussi H (2005) Quantum dot bioconjugates for imaging, labelling and sensing. *Nat Mater* 4:435.
62 Gao JH, Chen XY, Cheng Z (2010) Near-infrared quantum dots as optical probes for tumor imaging. *Curr Top Med Chem* 10:1147.

63 Bachilo SM*, et al.* (2002) Structure-assigned optical spectra of single-walled carbon nanotubes. *Science* 298:2361.
64 Liu Z*, et al.* (2008) Circulation and long-term fate of functionalized, biocompatible single-walled carbon nanotubes in mice probed by Raman spectroscopy. *Proc Natl Acad Sci USA* 105:1410.
65 Hong GS*, et al.* (2012) Multifunctional *in vivo* vascular imaging using near-infrared II fluorescence. *Nat Med* 18:1841.
66 Cheng L, Wang C, Liu Z (2013) Upconversion nanoparticles and their composite nanostructures for biomedical imaging and cancer therapy. *Nanoscale* 5:23.
67 Shen J*, et al.* (2013) Tunable near infrared to ultraviolet upconversion luminescence enhancement in (α-$NaYF_4$:Yb,Tm)/CaF_2 core/shell nanoparticles for *in situ* real-time recorded biocompatible photoactivation. *Small* 9:3213.
68 Mai HX, Zhang YW, Sun LD, Yan CH (2007) Highly efficient multicolor up-conversion emissions and their mechanisms of monodisperse $NaYF_4$:Yb,Er core and core/shell-structured nanocrystals. *J Phys Chem C* 111:13721.
69 Yin AX, Zhang YW, Sun LD, Yan CH (2010) Colloidal synthesis and blue based multicolor upconversion emissions of size and composition controlled monodisperse hexagonal $NaYF_4$:Yb,Tm nanocrystals. *Nanoscale* 2:953.
70 Wang F, Liu XG (2008) Upconversion multicolor fine-tuning: visible to near-infrared emission from lanthanide-doped $NaYF_4$ nanoparticles. *J Am Chem Soc* 130:5642.
71 Liu Q, Feng W, Yang T, Yi T, Li F (2013) Upconversion luminescence imaging of cells and small animals. *Nat Protoc* 8:2033.
72 Hemmer E*, et al.* (2013) Upconverting and NIR emitting rare earth based nanostructures for NIR-bioimaging. *Nanoscale* 5:11339.
73 Gu Z*, et al.* (2013) Recent advances in design and fabrication of upconversion nanoparticles and their safe theranostic applications. *Adv Mater* 25:3758.
74 Liu Q*, et al.* (2011) Sub-10 nm hexagonal lanthanide-doped $NaLuF_4$ upconversion nanocrystals for sensitive bioimaging *in vivo*. *J Am Chem Soc* 133:17122.
75 Zhou J*, et al.* (2010) Dual-modality *in vivo* imaging using rare-earth nanocrystals with near-infrared to near-infrared (NIR-to-NIR) upconversion luminescence and magnetic resonance properties. *Biomaterials* 31:3287.
76 Zhan Q*, et al.* (2011) Using 915 nm laser excited Tm^{3+}/Er^{3+}/Ho^{3+}-doped $NaYbF_4$ upconversion nanoparticles for *in vitro* and deeper *in vivo* bioimaging without overheating irradiation. *ACS Nano* 5:3744.
77 So MK, Loening AM, Gambhir SS, Rao JH (2006) Creating self-illuminating quantum dot conjugates. *Nat Protoc* 1:1160.
78 Frangioni JV (2006) Self-illuminating quantum dots light the way. *Nat Biotechnol* 24:326.
79 Matsuzawa T, Aoki Y, Takeuchi N, Murayama Y (1996) A new long phosphorescent phosphor with high brightness, $SrAl_2O_4$:Eu^{2+},Dy^{3+}. *J Electrochem Soc* 143:2670.
80 Van den Eeckhout K, Poelman D, Smet PF (2013) Persistent luminescence in non-Eu^{2+}-doped compounds: a review. *Materials* 6:2789.
81 Abdukayum A, Chen JT, Zhao Q, Yan XP (2013) Functional near infrared-emitting Cr^{3+}/Pr^{3+} co-doped zinc gallogermanate persistent luminescent nanoparticles with superlong afterglow for *in vivo* targeted bioimaging. *J Am Chem Soc* 135:14125.
82 Blasse G, Grabmaier BC, Ostertag M (1993) The afterglow mechanism of chromium-doped gadolinium gallium garnet. *J Alloys Compd* 200:17.
83 Kostyk L, Luchechko A, Zakharko Y, Tsvetkova O, Kuklinski B (2009) Cr-related centers in $Gd_3Ga_5O_{12}$ polycrystals. *J Lumin* 129:312.
84 Jia D, Lewis LA, Wang XJ (2010) Cr^{3+}-doped lanthanum gallogermanate phosphors with long persistent IR emission. *Electrochem Solid-State Lett* 13:J32.
85 Yan WZ*, et al.* (2010) Near infrared long-persistent phosphorescence in $La_3Ga_5GeO_{14}$:Cr^{3+} phosphor. *Opt Express* 18:20215.
86 Pan ZW, Lu YY (2011) Near infrared doped phosphors having a zinc, germanium, gallate matrix. University of Georgia Research Foundation, PCT/US patent application WO 2011/035292 A2.
87 Pan ZW, Lu YY, Liu F (2012) Sunlight-activated long-persistent luminescence in the near-infrared from Cr^{3+}-doped zinc gallogermanates. *Nat Mater* 11:58.
88 Yan WZ, Pan ZW (2011) Near infrared doped phosphors having an alkaline gallate matrix. University of Georgia Research Foundation, PCT/US patent application WO 2011/035294 A2.

89 Basavaraju N, *et al*. (2013) Red persistent luminescence in $MgGa_2O_4:Cr^{3+}$; a new phosphor for *in vivo* imaging. *J Phys D: Appl Phys* 46:375401.
90 Lu YY, Liu F, Gu ZJ, Pan ZW (2011) Long-lasting near-infrared persistent luminescence from β-$Ga_2O_3:Cr^{3+}$ nanowire assemblies. *J Lumin* 131:2784.
91 Bessiere A*, et al.* (2011) $ZnGa_2O_4:Cr^{3+}$: a new red long-lasting phosphor with high brightness. *Opt Express* 19:10131.
92 Zhuang YX, Ueda J, Tanabe S (2013) Enhancement of red persistent luminescence in Cr^{3+}-doped $ZnGa_2O_4$ phosphors by Bi_2O_3 codoping. *Appl Phys Express* 6:052602.
93 Allix M*, et al.* (2013) Considerable improvement of long-persistent luminescence in germanium and tin substituted $ZnGa_2O_4$. *Chem Mater* 25:1600.
94 Zhuang Y, Ueda J, Tanabe S (2013) Tunable trap depth in $Zn(Ga_{1-x}Al_x)_2O_4$:Cr,Bi red persistent phosphors: considerations of high-temperature persistent luminescence and photostimulated persistent luminescence. *J Mater Chem C* 1:7849.
95 Rogers WJ, Meyer CH, Kramer CM (2006) Technology insight: *in vivo* cell tracking by use of MRI. *Nat Clin Pract Card* 3:554.
96 Yen WM, Weber MJ (2004) *Inorganic Phosphors: Compositions, Preparation and Optical Properties* (CRC).
97 Ding J, Liu XY, Wang J, Shi Y (2000) Ultrafine ferrite particles prepared by coprecipitation/mechanical milling. *Mater Lett* 44:19.
98 Chen IC, Chen TM (2001) Sol-gel synthesis and the effect of boron addition on the phosphorescent properties of $SrAl_2O_4:Eu^{2+},Dy^{3+}$ phosphors. *J Mater Res* 16:644.
99 Hang T, Liu Q, Mao DL, Chang CK (2008) Long lasting behavior of $Gd_2O_2S:Eu^{3+}$ phosphor synthesized by hydrothermal routine. *Mater Chem Phys* 107:142.
100 Yu NY, Liu F, Li XF, Pan ZW (2009) Near infrared long-persistent phosphorescence in $SrAl_2O_4:Eu^{2+},Dy^{3+},Er^{3+}$ phosphors based on persistent energy transfer. *Appl Phys Lett* 95:231110.
101 Drbohlavova J*, et al.* (2009) Preparation and properties of various magnetic nanoparticles. *Sensors* 9:2352.
102 Cushing BL, Kolesnichenko VL, O'Connor CJ (2004) Recent advances in the liquid-phase syntheses of inorganic nanoparticles. *Chem Rev* 104:3893.
103 Choi SH, Kim NH, Yun YH, Choi SC (2006) Photoluminescence properties of $SrAl_2O_4$ and $CaAl_2O_4$ long-phosphorescent phosphors synthesized by an oxalate coprecipitation method. *J Ceram Process Res* 7:62.
104 Uche DOV (2013) Sol-gel technique: a veritable tool for crystal growth. *Adv Appl Sci Res* 4:506.
105 Ab Rahman I, Padavettan V (2012) Synthesis of silica nanoparticles by sol-gel: size-dependent properties, surface modification, and applications in silica-polymer nanocomposites—a review. *J Nanomater* 2012:132424.
106 Hench LL, West JK (1990) The sol-gel process. *Chem Rev* 90:33.
107 Schmidt H, Jonschker G, Goedicke S, Mennig M (2000) The sol-gel process as a basic technology for nanoparticle-dispersed inorganic-organic composites. *J Sol-Gel Sci Technol* 19:39.
108 Byrappa K, Adschiri T (2007) Hydrothermal technology for nanotechnology. *Prog Cryst Growth Charact Mater* 53:117.
109 Byrappa K, Yoshimura M (2001) *Handbook of Hydrothermal Technology: A Technology for Crystal Growth and Materials Processing* (Noyes).
110 Patil KC, Aruna ST, Ekambaram S (1997) Combustion synthesis. *Curr Opin Solid State Mater Sci* 2:158.
111 Sambandan E (2008) *Inorganic Materials Chemistry: General Concept and Research Topics* (iUniverse).
112 Hosokawa M, Nogi K, Naito M, Yokoyama T (2007) *Nanoparticle Technology Handbook* (Elsevier).
113 Salman AD, Ghadiri M, Hounslow M (2007) *Particle Breakage* (Elsevier).
114 Marignier JL, Belloni J, Delcourt MO, Chevalier JP (1985) Microaggregates of non-noble metals and bimetallic alloys prepared by radiation-induced reduction. *Nature* 317:344.
115 Alivisatos AP (1996) Semiconductor clusters, nanocrystals, and quantum dots. *Science* 271:933.
116 Neouze MA, Schubert U (2008) Surface modification and functionalization of metal and metal oxide nanoparticles by organic ligands. *Monatsh Chem* 139:183.
117 Mornet S, Vasseur S, Grasset F, Duguet E (2004) Magnetic nanoparticle design for medical diagnosis and therapy. *J Mater Chem* 14:2161.
118 Xiang SD, Selomulya C, Ho J, Apostolopoulos V, Plebanski M (2010) Delivery of DNA vaccines: an overview on the use of biodegradable polymeric and magnetic nanoparticles. *Wiley Interdiscip Rev: Nanomed and Nanobiotechnol* 2:205.
119 Goetze T*, et al.* (2002) Biocompatible magnetic core/shell nanoparticles. *J Magn Magn Mater* 252:399.
120 Sun C, Lee JSH, Zhang M (2008) Magnetic nanoparticles in MR imaging and drug delivery. *Adv Drug Deli Rev* 60:1252.

121 Martina MS*, et al.* (2005) Generation of superparamagnetic liposomes revealed as highly efficient MRI contrast agents for *in vivo* imaging. *J Am Chem Soc* 127:10676.
122 Maldiney T*, et al.* (2013) *In vivo* imaging with persistent luminescence silicate-based nanoparticles. *Opt Mater* 35:1852.
123 Mutin PH, Guerrero G, Vioux A (2003) Organic-inorganic hybrid materials based on organophosphorus coupling molecules: from metal phosphonates to surface modification of oxides. *C R Chim* 6:1153.
124 Neouze M-A, Schubert U (2008) Surface modification and functionalization of metal and metal oxide nanoparticles by organic ligands. *Chem Mon* 139:183.
125 Adden N*, et al.* (2006) Phosphonic acid monolayers for binding of bioactive molecules to titanium surfaces. *Langmuir* 22:8197.
126 Viornery C*, et al.* (2002) Surface modification of titanium with phosphonic acid to improve bone bonding: characterization by XPS and ToF-SIMS. *Langmuir* 18:2582.
127 Guerrero G, Mutin PH, Vioux A (2001) Anchoring of phosphonate and phosphinate coupling molecules on titania particles. *Chem Mater* 13:4367.
128 Hoque E*, et al.* (2006) Alkylphosphonate modified aluminum oxide surfaces. *J Phys Chem B* 110:10855.
129 Forget L, Wilwers F, Delhalle J, Mekhalif Z (2003) Surface modification of aluminum by n-pentanephosphonic acid: XPS and electrochemical evaluation. *Appl Surf Sci* 205:44.
130 Subbiah A*, et al.* (2005) A family of microporous materials formed by Sn(IV) phosphonate nanoparticles. *J Am Chem Soc* 127:10826.
131 Holland GP*, et al.* (2007) NMR characterization of phosphonic acid capped SnO_2 nanoparticles. *Chem Mater* 19:2519.
132 Zhang BB*, et al.* (2010) Surface functionalization of zinc oxide by carboxyalkylphosphonic acid self-assembled monolayers. *Langmuir* 26:4514.
133 White MA, Johnson JA, Koberstein JT, Turro NJ (2006) Toward the syntheses of universal ligands for metal oxide surfaces: controlling surface functionality through click chemistry. *J Am Chem Soc* 128:11356.
134 Ulman A (1996) Formation and structure of self-assembled monolayers. *Chem Rev* 96:1533.
135 Jun Y-W*, et al.* (2005) Nanoscale size effect of magnetic nanocrystals and their utilization for cancer diagnosis *via* magnetic resonance imaging. *J Am Chem Soc* 127:5732.
136 Carmen Bautista M, Bomati-Miguel O, del Puerto Morales M, Serna CJ, Veintemillas-Verdaguer S (2005) Surface characterisation of dextran-coated iron oxide nanoparticles prepared by laser pyrolysis and coprecipitation. *J Magn Magn Mater* 293:20.
137 Sung L-P, Scierka S, Baghai-Anaraki M, Ho DL (2002) Characterization of metal-oxide nanoparticles: synthesis and dispersion in polymeric coatings. *Mater Res Soc Symp Proc* 740:I5.4.1.
138 Yoshikawa J, Lewis JA, Chun BW (2009) Comb polymer architecture, ionic strength, and particle size effects on the $BaTiO_3$ suspension stability. *J Am Ceram Soc* 92:S42.
139 Palmqvist L, Holmberg K (2008) Dispersant adsorption and viscoelasticity of alumina suspensions measured by quartz crystal microbalance with dissipation monitoring and *in situ* dynamic rheology. *Langmuir* 24:9989.
140 Prabhakaran K, Kumbhar CS, Raghunath S, Gokhale NM, Sharma SC (2008) Effect of concentration of ammonium poly(acrylate) dispersant and MgO on coagulation characteristics of aqueous alumina direct coagulation casting slurries. *J Am Ceram Soc* 91:1933.
141 Penfold J, Thomas RK (1990) The application of the specular reflection of neutrons to the study of surfaces and interfaces. *J Phys: Condens Matter* 2:1369.
142 Sato K, Kondo S, Tsukada M, Ishigaki T, Kamiya H (2007) Influence of solid fraction on the optimum molecular weight of polymer dispersants in aqueous TiO_2 nanoparticle suspensions. *J Am Ceram Soc* 90:3401.
143 Nsib F, Ayed N, Chevalier Y (2006) Dispersion of hematite suspensions with sodium polymethacrylate dispersants in alkaline medium. *Colloid Surfaces A* 286:17.
144 Lyckfeldt O, Palmqvist L, Carlström E (2009) Stabilization of alumina with polyelectrolyte and comb copolymer in solvent mixtures of water and alcohols. *J Eur Ceram Soc* 29:1069.
145 Sahoo SK, Panyam J, Prabha S, Labhasetwar V (2002) Residual polyvinyl alcohol associated with poly (D,L-lactide-co-glycolide) nanoparticles affects their physical properties and cellular uptake. *J Controlled Release* 82:105.
146 Kakui T, Miyauchi T, Kamiya H (2005) Analysis of the action mechanism of polymer dispersant on dense ethanol alumina suspension using colloidal probe AFM. *J Eur Ceram Soc* 25:655.
147 Tang F, Uchikoshi T, Ozawa K, Sakka Y (2006) Effect of polyethylenimine on the dispersion and electrophoretic deposition of nano-sized titania aqueous suspensions. *J Eur Ceram Soc* 26:1555.

148 Nace VM (1996) Contrasts in the surface activity of polyoxypropylene and polyoxybutylene-based block copolymer surfactants. *J Am Oil Chem Soc* 73:1.
149 Lee HY*, et al.* (2008) Synthesis and characterization of PVP-coated large core iron oxide nanoparticles as an MRI contrast agent. *Nanotechnology* 19:165101.
150 Lai JR*, et al.* (2004) Mixed iron-manganese oxide nanoparticles. *J Phys Chem B* 108:14876.
151 Demchenko AP (2010) *Advanced Fluorescence Reporters in Chemistry and Biology II* (Springer).
152 Cheng ZL, Al Zaki A, Hui JZ, Muzykantov VR, Tsourkas A (2012) Multifunctional nanoparticles: cost versus benefit of adding targeting and imaging capabilities. *Science* 338:903.
153 Solé J, Bausa L, Jaque D (2005) *An Introduction to the Optical Spectroscopy of Inorganic Solids* (Wiley).
154 Szymczak H, Wardzynska M, Mylnikova IE (1975) Optical spectrum of Cr^{3+} in the spinel $LiGa_5O_8$. *J Phys C* 8:3937.
155 Alig RC (1971) Theory of photochromic centers in CaF_2. *Phys Rev B* 3: 536.
156 Staebler DL, Schnatterly SE (1971) Optical studies of a photochrominc color center in rare-earth-doped CaF_2. *Phys Rev B* 3:516.
157 Chandra VK, Chandra BP (2012) Dynamics of the mechanoluminescence induced by elastic deformation of persistent luminescent crystals. *J Lumin* 132:858.
158 Botterman J, Van den Eeckhout K, De Baere I, Poelman D, Smet PF (2012) Mechanoluminescence in $BaSi_2O_2N_2$:Eu. *Acta Mater* 60:5494.
159 Avouris P, Morgan TN (1981) A tunneling model for the decay of luminescence in inorganic phosphors: The case of Zn_2SiO_4:Mn. *J Chem Phys* 74:4347.
160 Delbecq CJ, Toyozawa Y, Yuster PH (1974) Tunneling recombination of trapped electrons and holes in KCl:AgCl and KCl:TlCl. *Phys Rev B* 9:4497.
161 Alemdar A, Oztekin N, Gungor N, Ece OI, Erim FB (2005) Effects of polyethyleneimine adsorption on the rheological properties of purified bentonite suspensions. *Colloid Surfaces A* 252:95.
162 Quan QM*, et al.* (2011) HSA coated iron oxide nanoparticles as drug delivery vehicles for cancer therapy. *Mol Pharm* 8:1669.
163 Ulbrich K*, et al.* (2011) Interaction of folate-conjugated human serum albumin (HSA) nanoparticles with tumour cells. *Int J Pharm* 406:128.
164 Boyd V, Cholewa OM, Papas KK (2008) Limitations in the use of fluorescein diacetate/propidium iodide (FDA/PI) and cell permeable nucleic acid stains for viability measurements of isolated islets of langerhans. *Curr Trends Biotechnol Pharm* 2:66.
165 Ben Amor K*, et al.* (2002) Multiparametric flow cytometry and cell sorting for the assessment of viable, injured, and dead bifidobacterium cells during bile salt stress. *Appl Environ Microbiol* 68:5209.
166 Gregori G*, et al.* (2001) Resolution of viable and membrane-compromised bacteria in freshwater and marine waters based on analytical flow cytometry and nucleic acid double staining. *Appl Environ Microbiol* 67:4662.
167 Canton I, Battaglia G (2012) Endocytosis at the nanoscale. *Chem Soc Rev* 41:2718.
168 Doherty GJ, McMahon HT (2009) Mechanisms of endocytosis. *Annu Rev Biochem* 78:857.
169 Conner SD, Schmid SL (2003) Regulated portals of entry into the cell. *Nature* 422:37.
170 Kim JG*, et al.* (2012) Ras-related GTPases Rap1 and RhoA collectively induce the phagocytosis of serum-opsonized zymosan particles in macrophages. *J Biol Chem* 287:5145.
171 Sanders CL, Adee RR (1968) Phagocytosis of inhaled plutonium oxide-^{239}Pu particles by pulmonary macrophages. *Science* 162:918.
172 Froystad MK, Rode M, Berg T, Gjoen T (1998) A role for scavenger receptors in phagocytosis of protein-coated particles in rainbow trout head kidney macrophages. *Dev Comp Immunol* 22:533.
173 Rudt S, Muller RH (1993) *In-vitro* phagocytosis assay of nanoparticles and microparticles by chemiluminescence .3. Uptake of differently sized surface-modified particles, and its correlation to particle properties and *in-vivo* distribution. *Eur J Pharm Sci* 1:31.
174 Iversen TG, Skotland T, Sandvig K (2011) Endocytosis and intracellular transport of nanoparticles: present knowledge and need for future studies. *Nano Today* 6:176.
175 Aderem A, Underhill DM (1999) Mechanisms of phagocytosis in macrophages. *Annu Rev Immunol* 17:593.
176 Le Roy C, Wrana JL (2005) Clathrin- and non-clathrin-mediated endocytic regulation of cell signalling. *Nat Rev Mol Cell Biol* 6:112.
177 Sieczkarski SB, Whittaker GR (2002) Influenza virus can enter and infect cells in the absence of clathrin-mediated endocytosis. *J Virol* 76:10455.
178 El-Sadik AO, El-Ansary A, Sabry SM (2010) Nanoparticle-labeled stem cells: a novel therapeutic vehicle. *Clin Pharmacol* 2:9.

179 Mercer J, Helenius A (2009) Virus entry by macropinocytosis. *Nat Cell Biol* 11:510.
180 Nimesh S*, et al.* (2006) Polyethylenimine nanoparticles as efficient transfecting agents for mammalian cells. *J Controlled Release* 110:457.
181 Evans CW*, et al.* (2011) Multimodal analysis of PEI-mediated endocytosis of nanoparticles in neural cells. *ACS Nano* 5:8640.
182 Li L*, et al.* (2013) Superparamagnetic iron oxide nanoparticles as MRI contrast agents for non-invasive stem cell labeling and tracking. *Theranostics* 3:595.
183 Yocum GT*, et al.* (2005) Effect of human stem cells labeled with ferumoxides-poly-L-lysine on hematologic and biochemical measurements in rats. *Radiology* 235:547.
184 Boussif O*, et al.* (1995) A versatile vector for gene and oligonucleotide transfer into cells in culture and *in vivo*: polyethylenimine. *Proc Natl Acad Sci USA* 92:7297.
185 Ferrari S*, et al.* (1997) ExGen 500 is an efficient vector for gene delivery to lung epithelial cells *in vitro* and *in vivo*. *Gene Ther* 4:1100.
186 Tang MX, Szoka FC (1997) The influence of polymer structure on the interactions of cationic polymers with DNA and morphology of the resulting complexes. *Gene Ther* 4:823.
187 Marquis BJ, Love SA, Braun KL, Haynes CL (2009) Analytical methods to assess nanoparticle toxicity. *Analyst* 134:425.
188 Ahlinder L, Ekstrand-Hammarstrom B, Geladi P, Osterlund L (2013) Large uptake of titania and iron oxide nanoparticles in the nucleus of lung epithelial cells as measured by Raman imaging and multivariate classification. *Biophys J* 105:310.
189 Chen N*, et al.* (2012) The cytotoxicity of cadmium-based quantum dots. *Biomaterials* 33:1238.
190 Hardman R (2006) A toxicologic review of quantum dots: toxicity depends on physicochemical and environmental factors. *Environ Health Perspect* 114:165.
191 Valizadeh A*, et al.* (2012) Quantum dots: synthesis, bioapplications, and toxicity. *Nanoscale Res Lett* 7:480.
192 Derfus A, Chan W (2004) Probing the cytotoxicity of semiconductor quantum dots. *Nano Lett* 4:11.
193 Zhang Y, Rufaihah AY, Sim EKW, Ye L, Chen NG (2008) Biocompatibility study of PEI-$NaYF_4$: Yb,Er upconversion nanoparticles. In: *4th Kuala Lumpur International Conference on Biomedical Engineering 2008: BIOMED*, Osman NAA *et al*. eds. Proceeding of IFMBE, 21:82.
194 Vallier L*, et al.* (2009) Early cell fate decisions of human embryonic stem cells and mouse epiblast stem cells are controlled by the same signalling pathways. *PLoS One* 4:e6082.
195 O'Dell BL, Sunde RA (1997) *Handbook of Nutritionally Essential Mineral Elements* (Marcel Dekker).
196 Di Bona KR*, et al.* (2011) Chromium is not an essential trace element for mammals: effects of a "low-chromium" diet. *J Biol Inorg Chem* 16:381.
197 Hoffer P (1980) Status of gallium-67 in tumor detection. *J Nucl Med* 21:394.
198 Schrand AM, Schlager JJ, Dai L, Hussain SM (2010) Preparation of cells for assessing ultrastructural localization of nanoparticles with transmission electron microscopy. *Nat. Protocols* 5:744.
199 Braydich-Stolle LK*, et al.* (2009) Crystal structure mediates mode of cell death in TiO_2 nanotoxicity. *J Nanopart Res* 11:1361.
200 Serda RE*, et al.* (2009) The association of silicon microparticles with endothelial cells in drug delivery to the vasculature. *Biomaterials* 30:2440.
201 Zhou J, Leuschner C, Kumar C, Hormes J, Soboyejo WO (2006) A TEM study of functionalized magnetic nanoparticles targeting breast cancer cells. *Mater Sci Eng C-Bio S* 26:1451.
202 Contag CH, Bachmann MH (2002) Advances *in vivo* bioluminescence imaging of gene expression. *Annu Rev Biomed Eng* 4:235.
203 Rabinovich BA*, et al.* (2008) Visualizing fewer than 10 mouse T cells with an enhanced firefly luciferase in immunocompetent mouse models of cancer. *Proc Natl Acad Sci USA* 105:14342.
204 Li SD, Huang L (2008) Pharmacokinetics and biodistribution of nanoparticles. *Mol Pharmaceutics* 5:496.
205 Neuberger T, Schopf B, Hofmann H, Hofmann M, von Rechenberg B (2005) Superparamagnetic nanoparticles for biomedical applications: possibilities and limitations of a new drug delivery system. *J Magn Magn Mater 293*:483.
206 Choi HS*, et al.* (2007) Renal clearance of quantum dots. *Nat Biotechnol* 25:1165.
207 Schipper ML*, et al.* (2009) Particle size, surface coating, and PEGylation influence the biodistribution of quantum dots in living mice. *Small* 5:126.
208 De Jong WH*, et al.* (2008) Particle size-dependent organ distribution of gold nanoparticles after intravenous administration. *Biomaterials* 29:1912.
209 Sharifi S*, et al.* (2012) Toxicity of nanomaterials. *Chem Soc Rev* 41:2323.

210 Li Y, Li Z, Wang X, Liu F, Cheng Y, Zhang B, Shi D (2012) *In vivo* cancer targeting and imaging-guided surgery with near infrared-emitting quantum dot bioconjugates. *Theranostics* 2:769.
211 Yan J*, et al.* (2000) Critical role of Kupffer cell CR3 (CD11b/CD18) in the clearance of IgM-opsonized erythrocytes or soluble beta-glucan. *Immunopharmacology* 46:39.
212 Sadauskas E*, et al.* (2007) Kupffer cells are central in the removal of nanoparticles from the organism. *Part Fibre Toxicol* 4:10.
213 Gao JH*, et al.* (2010) Ultrasmall near-infrared non-cadmium quantum dots for *in vivo* tumor imaging. *Small* 6:256.
214 Moghimi SM, Hunter AC, Murray JC (2001) Long-circulating and target-specific nanoparticles: theory to practice. *Pharmacol Rev* 53:283.
215 Lee S-Y, Cheng J-X, Gad SC. (2010) *Pharmaceutical Sciences Encyclopedia* (Wiley).
216 Duncan R (2003) The dawning era of polymer therapeutics. *Nat Rev Drug Discovery* 2:347.
217 Gao X, Cui Y, Levenson RM, Chung LWK, Nie S (2004) *In vivo* cancer targeting and imaging with semiconductor quantum dots. *Nat Biotechnol* 22:969.
218 Jain RK (2001) Delivery of molecular medicine to solid tumors: lessons from *in vivo* imaging of gene expression and function. *J Controlled Release* 74:7.
219 Jain RK (1999) Transport of molecules, particles, and cells in solid tumors. *Annu Rev Biomed Eng* 1:241.
220 Matsumura Y, Maeda H (1986) A new concept for macromolecular therapeutics in cancer chemotherapy: mechanism of tumoritropic accumulation of proteins and the antitumor agent smancs. *Cancer Res* 46:6387.
221 Fang J, Nakamura H, Maeda H (2011) The EPR effect: unique features of tumor blood vessels for drug delivery, factors involved, and limitations and augmentation of the effect. *Adv Drug Delivery Rev* 63:136.
222 Maeda H, Nakamura H, Fang J (2013) The EPR effect for macromolecular drug delivery to solid tumors: improvement of tumor uptake, lowering of systemic toxicity, and distinct tumor imaging *in vivo*. *Adv Drug Delivery Rev* 65:71.
223 Maeda H (2010) Tumor-selective delivery of macromolecular drugs *via* the EPR effect: background and future prospects. *Bioconjugate Chem* 21:797.
224 Bouchelouche K*, et al.* (2011) PET/CT imaging and radioimmunotherapy of prostate cancer. *Semin Nucl Med* 41:29.
225 Semmler W, Schwaiger M (2008) *Molecular Imaging II* (Springer).
226 Wu C*, et al.* (2013) *In vivo* cell tracking *via* ^{18}F-fluorodeoxyglucose labeling: a review of the preclinical and clinical applications in cell-based diagnosis and therapy. *Clin Imaging* 37:28.
227 Daley GQ, Scadden DT (2008) Prospects for stem cell-based therapy. *Cell* 132:544.
228 Thompson M, Wall DM, Hicks RJ, Prince HM (2005) *In vivo* tracking for cell therapies. *Q J Nucl Med Mol Imaging* 49:339.
229 Bengel FM, Schachinger V, Dimmeler S (2005) Cell-based therapies and imaging in cardiology. *Eur J Nucl Med Mol Imaging* 32:S404.
230 Hong H, Yang YA, Zhang Y, Cai WB (2010) Non-invasive cell tracking in cancer and cancer therapy. *Curr Top Med Chem* 10:1237.
231 Tunieh PC, Radu CG, Ribas A (2008) PET imaging of cancer immunotherapy. *J Nucl Med* 49:865.
232 Foster AE*, et al.* (2008) *In vivo* fluorescent optical imaging of cytotoxic T lymphocyte migration using IRDye800CW near-infrared dye. *Appl Opt* 47:5944.
233 Swirski FK*, et al.* (2007) A near-infrared cell tracker reagent for multiscopic *in vivo* imaging and quantification of leukocyte immune responses. *PLoS One* 2:e1075.
234 Lee MH, Lee WH, Van Y, Contag CH, Liu CP (2007) Image-guided analyses reveal that non-CD4 splenocytes contribute to CD4+ T cell-mediated inflammation leading to islet destruction by altering their local function and not systemic trafficking patterns. *Mol Imaging* 6:369.
235 Sen D, Deerinck TJ, Ellisman MH, Parker I, Cahalan MD (2008) Quantum dots for tracking dendritic cells and priming an immune response *in vitro* and *in vivo*. *PLoS One* 3:e3290.
236 Sutton EJ, Henning TD, Pichler BJ, Bremer C, Daldrup-Link HE (2008) Cell tracking with optical imaging. *Eur Radiol* 18:2021.
237 Zhao H*, et al.* (2005) Emission spectra of bioluminescent reporters and interaction with mammalian tissue determine the sensitivity of detection *in vivo*. *J Biomed Opt* 10:041210.
238 Dong NN*, et al.* (2011) NIR-to-NIR two-photon excited CaF_2:Tm^{3+},Yb^{3+} nanoparticles: multifunctional nanoprobes for highly penetrating fluorescence bio-Imaging. *ACS Nano* 11:8665.
239 Condeelis J, Pollard JW (2006) Macrophages: obligate partners for tumor cell migration, invasion, and metastasis. *Cell* 124:263.

240 Xie J*, et al.* (2010) Human serum albumin coated iron oxide nanoparticles for efficient cell labeling. *Chem Commun* 46:433.
241 Green CE*, et al.* (2009) Chemoattractant signaling between tumor cells and macrophages regulates cancer cell migration, metastasis and neovascularization. *PLoS One* 4:e6713.
242 Hood JD, Cheresh DA (2002) Role of integrins in cell invasion and migration. *Nat Rev Cancer* 2:91.
243 Cai WB, Chen XY (2008) Multimodality molecular imaging of tumor angiogenesis. *J Nucl Med* 49:113s.